INVESTIGATIONS INTO PHOTO-EXCITED STATE DYNAMICS IN COLLOIDAL QUANTUM DOTS

by

Gaurav Singh

A dissertation submitted to the faculty of
The University of North Carolina at Charlotte
in partial fulfillment of the requirements
for the degree of Doctor of Philosophy in
Nanoscale Science

Charlotte

2015

Approved by:

____
Dr. Marcus Jones

____
Dr. Jordan Poler

____
Dr. Yong Zhang

____
Dr. Michael Walter

____
Dr. Ed Stokes

ABSTRACT

GAURAV SINGH. Investigations into photo-excited state dynamics in colloidal quantum dots. (Under the direction of DR. MARCUS JONES)

Colloidal Quantum dots (QDs) have garnered considerable scientific and technological interest as a promising material for next generation solar cells, photo-detectors, lasers, bright light-emitting diodes (LEDs), and reliable biomarkers. However, for practical realization of these applications, it is crucial to understand the complex photo-physics of QDs that are very sensitive to surface chemistry and chemical surroundings. Depending on the excitation density, QDs can support single or multiple excitations. The first part of this talk addresses evolution of QD excited state dynamics in the regime of low excitation intensity. We use temperature-resolved time-resolved fluorescence spectroscopy to study exciton dynamics from picoseconds to microseconds and use kinetic modeling based on classical electron transfer to show the effect of surface trap states on dynamics of ground-state exciton manifold in core-shell CdSe/CdS QDs. We show that the thickness of CdS shell plays an important role in interaction of CdSe core exciton states with nanocrystal environment, and find that a thicker shell can minimize the mixing of QD exciton states with surface trap states.

I will then present an investigation into the dynamics of multiply-excited states in QDs. One of the key challenges in QD spectroscopy is to reliably distinguish multi- from single-excited states that have similar lifetime components and spectroscopic signatures. I will describe the development of a novel multi-pulse fluorescence technique to selectively probe multi-excited states in ensemble QD samples and determine the nature of the multi-excited state contributing to the total fluorescence even in the limit of low fluorescent yields. We find that in our sample of CdSe/CdS core/shell QDs the multi-excited emission is dominated by emissive trion states rather than biexcitons. Next, I will discuss the application of this technique to probe exciton-plasmon coupling in layered hybrid films of QD/gold nanoparticles separated by poly-electrolyte spacers of varying thickness, and conclusively show that plasmon coupling can strongly enhance fluorescence yields and dynamics of multi-excited states in QDs. I will also discuss some recent experiments using our multi-pulse technique to successfully probe delayed fluorescence (due to triplet-triplet annihilation) in porphyrin dyes.

The results presented here are helping us to advance the field of QD photo-physics by enabling us to learn more about multi-excited states in QDs and many of the factors that control their radiative and non-radiative recombination. They are also guiding us in the design of better ways to utilize multi-excited states in new hybrid metal-QD devices.

DEDICATION

This dissertation is dedicated to my mother, Asha Devi, and my father, Ompal Singh Chauhan, and to all my teachers.

ACKNOWLEDGMENTS

This thesis would not have been possible without the support of several people who have guided and supported me at the various stages of my PhD work. First and foremost, I would like to thank my advisor, Dr. Marcus Jones, affectionately referred to as “boss”, for supervising my research, and instilling a methodical way of approaching any research problem. I would also like to sincerely appreciate the support of faculty and staff at the chemistry department, specially, Dr. Jordan Polar, Dr. Juan Vivero, Dr. Bernadette Donovan-Merkert, Dr. Jon Merket, Dr. Thomas Schmedake and Caroline Kennedy for helping me to navigate the Nanoscale PhD program. I would also like to thank Dr. Michael Walter and Dr. Yong Zhang for always taking the time out to answers my questions and helping me out with my research problems. I am also grateful to all my colleagues and friends for those fruitful discussions on physics, nanotechnology, and other areas of life.

TABLE OF CONTENTS

LIST OF FIGURES

LIST OF ABBREVIATIONS

1-D	One-dimensional
2-D	Two-dimensional
3-D	Three-dimensional
AMP	Amplifier
ADC	Analogue-to-digital converter
Au	Gold
BX	Biexciton
BX^+	Trion
BX^{2+}	Doubly charged biexciton
CdSe	Cadmium Selenide
CdS	Cadmium Sulfide
CQDs	Colloidal quantum dots
CFD	Constant function discriminator
DOS	Density of states
DOF	Depth of focus
EMA	Effective mass approximation
E_g	Band gap
ET	Electron transfer
fs	Femtosecond
FWHM	Full width at half maximum
G	Ground state
HP	High power

IRF	Instrument response function
LEDs	Light-emitting diodes
LP	Low power
MBE	Molecular beam epitaxy
MOVPE	Metal-organic vapor phase epitaxy
MEG	Multiple exciton generation
MX	Multi-excited
ML	Monolayer
MP	Medium power
NCs	Nanocrystals
NPs	Nanoparticles
ns	Nanoseconds
OPO	Optical parametric oscillator
PbSe	Lead Selenide
PbS	Lead Sulfide
PL	Photoluminescence
PMT	Photomultiplier
ps	Picoseconds
QDs	Quantum dots
QW	Quantum well
QWr	Quantum wire
SILAR	Successive ion layer adsorption and reaction
SP	Surface plasmon

TOPO	Trioctylphosphine oxide
TEM	Transmission electron microscopy
TA	Transient absorption
TRPL	Time resolved photoluminescence
TCSPC	Time correlated single photon counting
TAC	Time-to-amplitude convertor
Ti	Titanium
T1 and T2	Trap states
X	High energy exciton
X_B	Bright exciton states
X_D	Dark exciton states
X^+	Charged exciton

CHAPTER 1 : QUANTUM DOTS

1.1 Introduction

If we look at recent history, our society has been tremendously influenced by the scale at which things work. The advent of the microprocessor in the seventies transformed the way we work, think, and interact with technology. It ushered us into our present 'information age' .The scale has now shifted from “one-millionth of a meter” to “one billionth of a meter”. However, nanoscale is not just another shrinking of scale. The physical and chemical properties of materials begin to change at sizes less than 100 nm.[1] The size, surface and geometry of nano-materials start playing a significant role; giving rise to new emergent properties. Due to highly multidisciplinary nature of nanoscale science, it is important to put into perspective the actual *size dimensions* that make a bulk material *nano* especially for semiconductor nanomaterials. If we are interested in optical and electronic properties, as in my case, a useful distinction could be the de-Broglie wavelength or Bohr radius of carriers in the material.[2] Even better, for semiconducting materials, we can define material size in terms of bulk Bohr exciton radius.

Excitons are essentially electron-hole pairs bound by coulombic attraction in semiconductor materials and can have binding energies ranging from a few meVs to hundreds of meVs.[3–53] For bulk semiconductors, exciton binding energies are typically much less or comparable to the thermal energy at room temperature, and therefore we don't usually see excitonic features in the light absorption spectrum of bulk semiconductors.

However, as we shall see subsequently, binding between electron and holes is much stronger in nanostructures since charge carriers are forced to come closer owing to smaller physical size of the nanostructures.

If any of the physical dimensions of the material is smaller or comparable to the exciton bohr radius, the charge carriers i.e. electrons and holes start feeling the effect of finite boundary of the material and become quantum mechanically confined along that spatial dimension. The confinement energy of the charge carriers would then depend on the length of material dimension relative to the Bohr radius of charge carriers and the magnitude of confining potential.

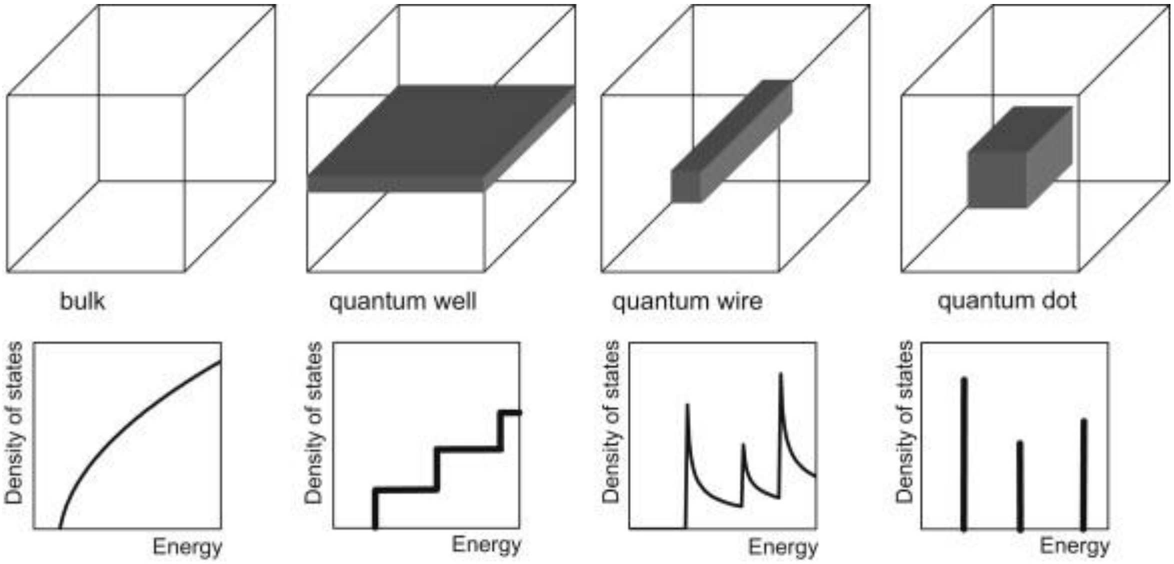

Figure 1.1: Sketch of the geometry and the density of states of a bulk material and of nanostructures in which the carrier confinement is in one (QW), two (QWr) or three dimensions (QD). Reprinted with permission from reference.[6]

Figure1.1 shows a way of classifying nanostructures based on the number of dimensions in which charge carriers are confined or are free to move. A nanostructure in which charge carriers are confined in only one dimension is called a quantum well (QW). It could be realized by having a very thin layer of a low bandgap semiconductor sandwiched between two insulator layers, and historically QWs based on III-V semiconductors were one of the first nanostructures fabricated and studied extensively since the early 1970s.[6] In contrast to a bulk material for which the density of states (DOS) varies parabolically with energy; the DOS in QWs vary in a step like fashion.

Similarly, a structure in which the motion of charge carriers is confined in two directions is known as a quantum wire (QWr). And, if we make a semiconductor crystal so small that all the three spatial dimensions are smaller or comparable to bulk Bohr exciton radius, the resulting nanostructure or nanocrystal (NC) is known as a Quantum dot (QD). The DOS for QDs vary in atom-like discrete steps and for this reason, they are sometimes also referred to as "artificial" atoms or molecules. In this sense, semiconductor nanocrystals (NCs) span the gap between bulk materials and molecules.

Quantum Dots have been one of the mostly widely researched class of nanomaterials for past two decades, and have been one of the “central materials” in nanoscience community[7]; considering the amount of scientific interest and research funding that QDs have attracted for such a long time. Apart from very interesting fundamental science, QDs are also extremely attractive candidate material for a variety of commercial applications and technologies. High extinction coefficient, excellent photo-stability, and a size tunable bandgap across the entire visible/infrared spectrum makes them an exceptional material for lighting, display and bio-imaging applications.[8] There is already a QD based television display manufactured by Sony that is available in the commercial market[9], and it is predicted that QD and QD LED based displays will have a significant market presence by 2020.[10–12] QDs are also strong candidates for next generation solar cells based on multi-exciton generation[13–15] and hot-carrier effects[16], single photon sources for quantum[17] computing, low cost compact lasers[18], and high quantum efficiency photodetectors.[19]

1.2 Electronic Structure of QDs

3-D confinement of charge carriers in QDs fundamentally changes its electronic structure, and leads to size dependent optoelectronic properties, particularly light absorption and fluorescence.

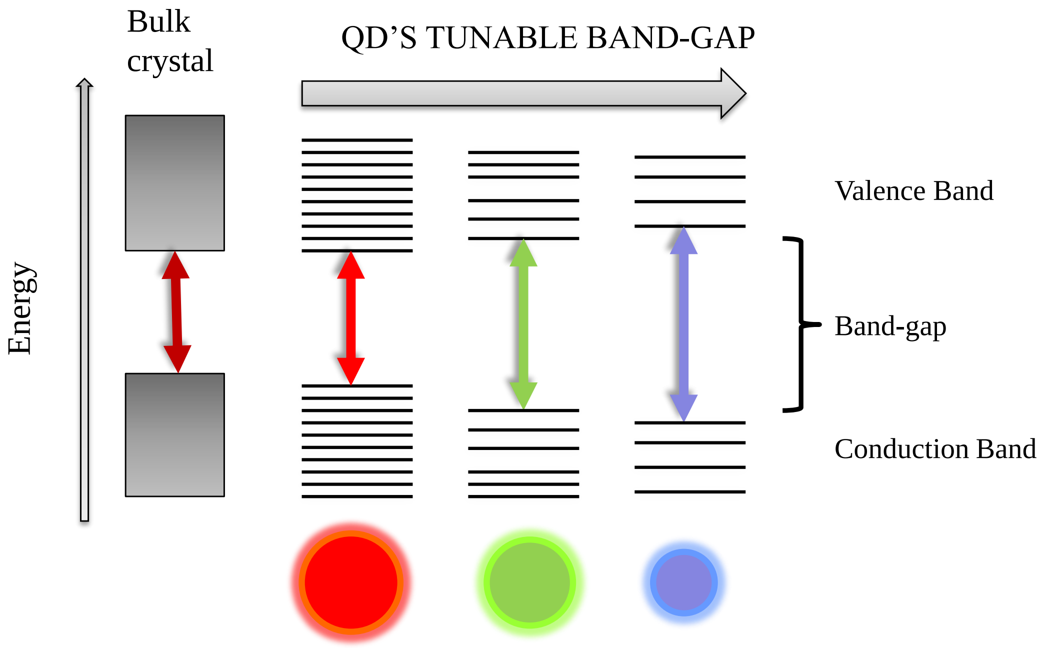

Figure 1.2: An illustration showing size-dependent tunability of QD electronic bandgap.

Thus, by merely changing the size of the nanocrystal, we can tune its band gap across the entire visible spectrum (Figure 1.2).

The size dependent electronic structure of QDs can be explained by a simple "particle-in-a-sphere" model. The model is basically similar to the textbook "particle-in-a-box" problem with the exception that instead of a square well potential, the particle is confined in a spherical potential well of radius a,

$$V(r) = \begin{cases} 0, & r < a \\ \infty, & r > a \end{cases} \tag{1.1}$$

The Schrodinger equation can then be solved for the above boundary conditions to determine the wavefunctions and energies of the particle. The solutions for this problem are given by Flugge[20] and following are the wavefuctions for the particle:

$$\psi\ (r, \theta, \phi) = C\ \frac{j_l\big(k_{n,l}, r\big) Y_l^m(\theta, \phi)}{r} \tag{1.2}$$

where C is the normalization constant, $Y_l^m(\theta, \phi)$ is a spherical harmonic, $j_l\big(k_{n,l}, r\big)Y_l^m$ is the l^{th} order spherical Bessel function, and

$$k_{n,l} = \frac{\alpha_{n,l}}{a} \tag{1.3}$$

with $\alpha_{n,l}$ the nth zero of j_l .

The energy of the particle is given by,

$$E_{n,l} = \frac{\hbar^2\ k_{n,l}^2}{2m_0} \tag{1.4}$$

The particle energies given by equation 1.4 are exactly similar to the kinetic energy of a free particle except that the wave vector, $k_{n,l}$, is quantized by the spherical boundary condition. It should be noted that the energy is inversely proportional to the square of the radius of the sphere, a, and therefore is strongly dependent on the size of the particle. This is the reason why the opto-electronic properties of the QDs change with size. .

The "particle-in-a-sphere" formalism so far hasn't taken into account the effect of lattice atoms and lattice symmetry of the NC. However, the *effective mass approximation*[21] (EMA) can be used to incorporate the effect of periodic lattice potential felt by the charged particles in the NC by using the "effective" masses, m_{eff}, for the particles instead of m_0, and therefore equation 1.4 can be rewritten as,

$$E_{n,l} = \frac{\hbar^2 \, k_{n,l}^2}{2m_{eff}} \tag{1.5}$$

The effective mass takes into account the effect of curvature of the conduction and valence bands at k=0 on electron and holes, and allows us to retain the particle-in-a-sphere formalism for the carriers. If we treat electron and holes as two separate particles confined in the spherical NC, the total energy would just be the sum of the electron and hole contributions, and then using the effective mass approximation, the bandgap of NC can be calculated as,

$$E_g = E_{bulk} + \frac{\hbar^2 \, k_{n,l}^2}{2m_{e,eff}} + \frac{\hbar^2 \, k_{n,l}^2}{2m_{h,eff}} \tag{1.6}$$

where E_{bulk} is the bulk bandgap of the semiconductor, $m_{e,eff}$ and $m_{h,eff}$ are effective masses for the electron and the hole respectively.

We can further rewrite equation 1.6 by expressing confinement energy in terms of QD size using equation 1.3, and also account for the coulombic attraction between electron and holes,

$$E_g = E_{bulk} + \frac{\hbar^2\pi^2}{2\ a^2}\left(\frac{1}{m_{e,eff}} + \frac{1}{m_{h,eff}}\right) - \frac{1.8\ e^2}{\epsilon\ a} \tag{1.7}$$

Equation 1.7 clearly demonstrates the well-known size dependence of electronic band-gap for spherical QDs.

Further, since the confinement energy scales as $1/a^2$, while the coulomb attraction varies as $1/a$, in sufficiently small dots the confinement term dominates. This is the case when the QD size is much smaller than the bulk exciton Bohr radius, and in this size regime, also known as st*rong confinement regime*[22], the electron and holes are treated independently of each other and we can neglect the coulombic interaction. However, an interesting scenario arises when QD size is smaller than one carrier's Bohr radius but larger than other's. This is also known sometimes as *intermediate confinement regime*, and is often observed in CdSe NCs, which are also used in this study.[2,23] The Bohr exciton radius for CdSe is ~5nm, and many CdSe QDs are often coated with a few nm thick semiconducting shell such as CdS, that can lead to a delocalized electron but a strongly confined hole in the core. However, the absorption spectra of CdSe core-shell nanoparticles still show several different absorption peaks indicating that the quantization effects are preserved in the nanoparticle.

Another important property that significantly changes in nanocrystals is density of states (DOS). For a 3-D confined nanomaterial such as QDs, the DOS can be described by the following equation[24],

$$\frac{dN}{dE} \propto \frac{d}{dE}\left(\sum_{\varepsilon_i<E} \theta\,(E-\varepsilon_i)\right) \propto \sum_{\varepsilon_i<E} \delta\,(E-\varepsilon_i) \qquad (1.8)$$

where θ is standard Heaviside function.

Equation 1.8 indicates that DOS in QDs vary in sharp discrete steps, which is in complete contrast to a quasi-continuous parabolic distribution of DOS in bulk semiconductors, shown graphically in Figure 1.1. This discretization of DOS in QDs can lead to interesting intraband dynamics and equilibrium properties. In strongly confined QDs, the spacing of energy levels can be much greater than the thermal energy available at room temperature thus preventing the thermal depopulation of the ground state. This phenomenon forms the basis for next generation QD lasers where lasing threshold could be made temperature insensitive at an excitation level of one exciton per QD.[25] Further, in strongly confined QDs, the discretization of electronic states can strongly affect carrier relaxation through electron-phonon coupling. The intraband spacing in electronic levels can be as large as several hundred meV that is much bigger than typical phonon energies of tens of meV, thus making it difficult for charge carriers to couple with phonons leading to phenomenon also known as “*photon bottleneck*” in QDs.[26]

1.3 Synthesis of Colloidal Nanocrystals

Colloidal nanocrystals or quantum dots (CQDs) are essentially semiconductor nanocrystals (NCs) that are synthesized and suspended in the solution phase. QDs can also be grown by epitaxial techniques such as molecular beam epitaxy (MBE) or metal-organic vapor phase epitaxy (MOVPE) that involves strain induced growth of small QD islands on a lattice mismatched substrate.[27] This is known as the *Stranski-Krastanow* growth mechanism. However, solution processability, convenience of bench-top synthesis, and the capability to grow high quality monodisperse QDs of various shapes and sizes makes colloidal synthesis very attractive and has led to its widespread adoption in making QDs.

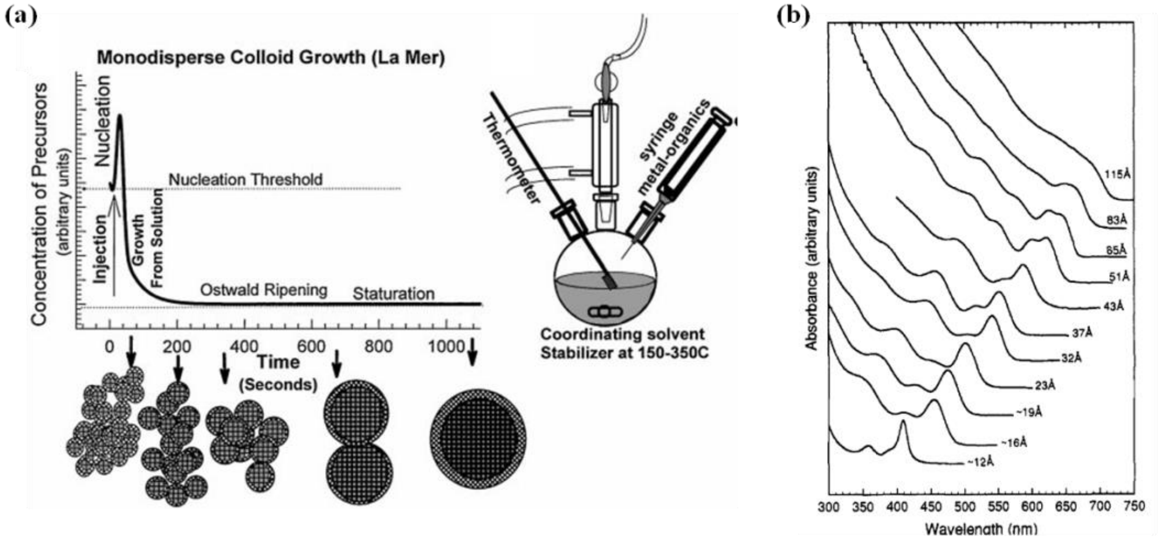

Figure 1.3. (a) A cartoon showing various growth stages during NC synthesis and the synthetic apparatus employed. Reproduced with permission.[28] Copyright 2000, Annual Reviews. (b) Optical absorption spectra at room temperature of CdSe QDs varying in size from 1.2 nm to 11.5 nm. Reproduced with permission.[29] Copyright 1993, American Chemical Society.

In 1993, a key advance in making high quality mono-disperse CQDs was reported in a landmark paper by Murray, Norris, and Bawendi.[29] The paper described a synthesis protocol, based on the classic colloidal synthesis work by LaMer and Dinegar,[30] of making cadium chalcogenide QDs (CdE where E=S, Se, Te). The procedure, known as the hot-injection method (Figure 1.3a), essentially involved injecting "cold" organometallic precursors at room temperature into a hot organic solvent, namely, trioctylphosphine oxide (TOPO). The injection of precursor solution leads to rapid homogenous nucleation of cadmium chalcogenide particles. However, a decrease in precursor concentration owing to nucleation, and a drop in solution temperature due to introduction of room temperature precursors prevents further nuclei formation (shown in Figure 1.3a). The reaction temperature is then raised back, though kept below nucleation temperature, to allow for slow growth and annealing of nanocrystals. Small aliquots are taken at regular intervals for optical measurements to monitor the nanocrystal size. The increase in nanocrystal size is indicated by a corresponding red-shift in the optical absorption spectra as shown in Figure 1.3b.

The above synthesis produces NCs with high crystallinity, and a good size dispersion but poor fluorescence quantum yields typically less than ~10%. It is evident that organic ligands are not sufficient to passivate the QD surface, and the unpassivated atoms and dangling bonds on the surface create trapping centers that act as a major source of non-radiative recombination leading to low fluorescence quantum yields. An effective strategy to improve surface passivation, first demonstrated by Hines and Guyot-Sionnest,[31] is to grow a thin shell of a wide-bandgap semiconductor such as ZnS or CdS on nanocrystals.

The inorganic shell not only effectively passivates the surface traps but also acts as a barrier between the optically active QD core and its surroundings leading to photostable and highly fluorescent QDs that can have emission yields around 50%. Such coated nanocrystals are called *core-shell* nanocrystals.[32] Further, introduction of a semiconducting shell leads to delocalization of exciton wave function into the shell that leads to a bathochromic shift in excitonic absorbance and fluorescence spectra.

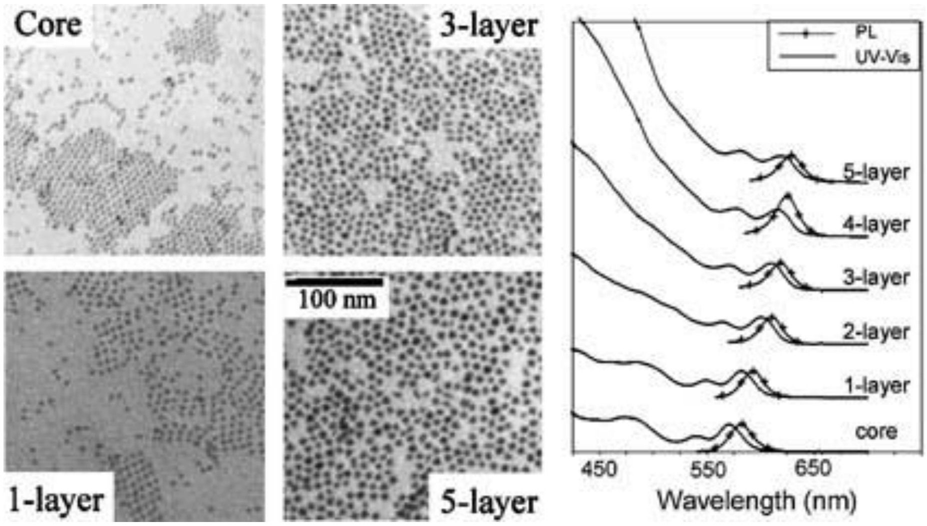

Figure 1.4: (Left) TEM images of CdSe NCs depicting the increase in diameter upon growth of several monolayers of a CdS shell by means of the SILAR technique. **(**Right**)** UV-vis and PL spectra of core-shell QDs with different shell thicknesses. Reproduced from reference.[33] Copyright 2001, American Chemical Society.

There are several different synthetic approaches for making core-shell QDs, but most methodologies either involve adding shell precursor slowly or by a technique originally introduced by Peng and coworkers[33] called successive ion layer adsorption and reaction (SILAR). The primary goal of SILAR technique is to prevent homogeneous nucleation of shell precursors by preventing their coexistence in the reaction bath, and allows precise control of shell thickness by alternating injection of cationic and anionic precursors, and thus depositing only half of a monolayer at a time. Figure 1.4 shows the TEM images, and evolution of absorbance and fluorescence spectra at different stages of shell growth on CdSe QDs. The SILAR technique allows synthesis of highly mono-disperse and defect free core-shell nanocrystals, and has become the standard method for shelling QDs. The CdSe-CdS core-shell QDs used in this study are also synthesized by a modified SILAR method.

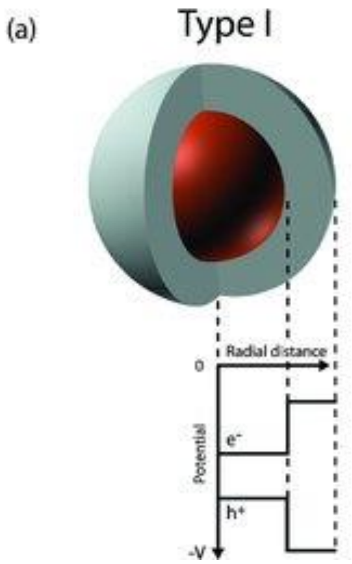

Figure 1.5: Alignment of conduction and valence band edges in heterostructured QDs. a) Type-I heterostructure constituting a higher band-gap outer shell. b) Type-II heterostructure having a staggered band alignment. Reproduced from reference.[34]

The choice of shell material is a key factor that determines the band-alignment of the resulting core-shell structure. Depending on the relative position of the valence and conduction band levels, we can either confine both electrons or holes in the core, known as **Type I** system or could have one of charge carriers delocalized into the shell, known as **Type II** band alignment (Figure 1.5). Type II systems are particularly attractive for energy conversion and catalytic applications. Further, type and thickness of shell material not only influences the fluorescent quantum-yield and photo stability but also strongly modifies the QD excited state dynamics as we shall see in later chapters.

1.4 Photo-Excited State dynamics

1.4.1 Overview

Photo-absorption above or near bandgap energies results in creation of coupled electron-hole pairs or excitons in quantum dots. Depending on the photon energy and excitation density, a single excitation event can create one or multiple excitons per QD particle. Further, as we shall see in later chapters, if the photoexcitation rate is comparable to excited state lifetimes, the QD can be re-excited thus introducing new excited states with completely different dynamics. Figure 1.6 gives a glimpse of different photo excited states that are normally observed in quantum confined semiconductor nanocrystals.

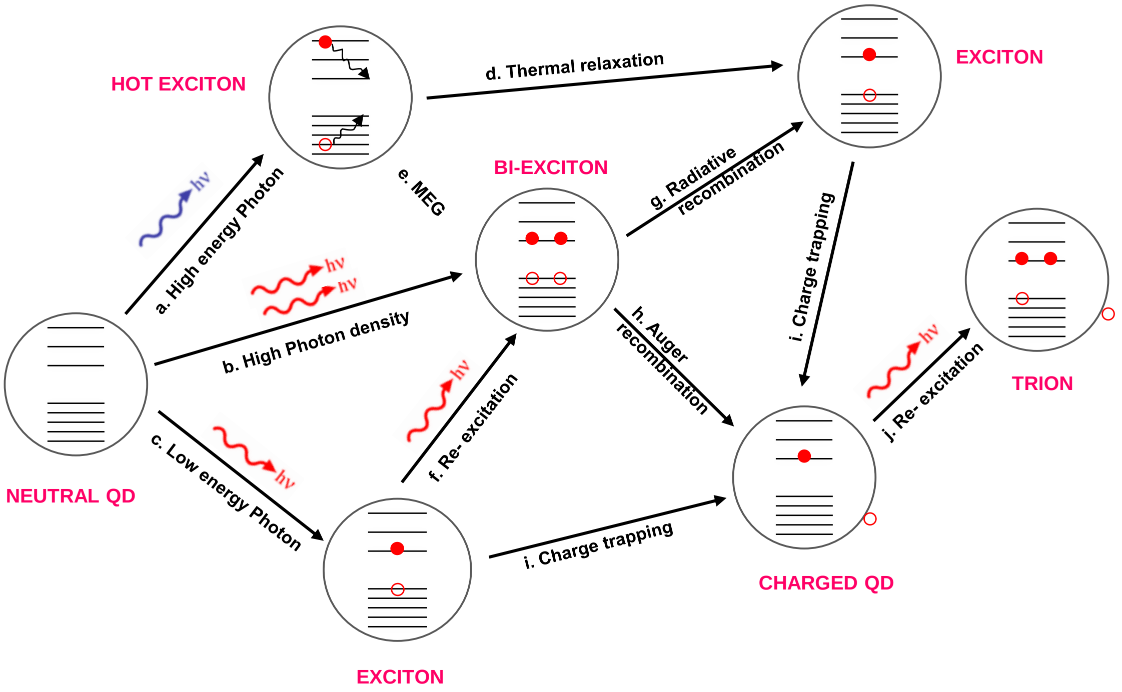

Figure 1.6: A manifold of photo- excited states in QDs.

The study of photo excited states dynamics in semiconductor nanocrystals is much more complex than their bulk counterparts due to strong coupling of QD excited state with the nanocrystal surface and its environment. Further, due to size heterogeneity in colloidal NCs, the ensemble QD dynamics can be markedly different from single particle dynamics, which makes it difficult to identify physical processes responsible for charge dynamics.

In the regime of low excitation intensity, the QD dynamics can be successfully described by interaction of ground state exciton with surface states employing classical electron transfer theory. We will discuss this in more detail in chapter 3 where we will use temperature-dependent time resolved photoluminescence experiments to study charge carrier dynamics of single exciton states in QDs.

In the case, where the excitation photon energy is much greater than the QD bandgap, the excess energy can be used to create additional electron-hole pairs by an inverse auger process called impact ionization or multiple exciton generation (MEG) (Figure 1.6e). MEG is significantly much more efficient in semiconductor nanocrystals than bulk semiconductors. Energy conservation dictates that minimum photon energy to generate two electron–hole pairs per photon has to be at least twice the bandgap (E_g). For bulk semiconductors, in addition to conserving energy, crystal momentum also needs to be conserved requiring excess energy.[35] For e.g. energy and momentum constraints make the MEG threshold to be 4.22 E_g for bulk PbSe.[36] However, from Heisenberg's uncertainty principle, well-defined location of carriers in the nanocrystal makes the momentum uncertain, and therefore the momentum conservation limit is relaxed, and for PbSe QDs, MEG threshold has been observed at just 2.7 E_g.

For low bandgap semiconductor nanocrystals like PbS, the MEG threshold can easily lie in the visible spectral region, and therefore, MEG in nanocrystals offers a possibility to create highly efficient photo-voltaic devices. Alternatively, when the excitation intensity is high, QDs can absorb two or more photons from a single laser pulse to generate multiple excitons (Figure 1.6b).

Further, QDs can be re-excited again before they relax down to the ground state, and therefore, sequential excitation provides yet another way of generating multiple excitons (Figure 1.6c). However, it is entirely possible that instead of creating another electron-hole pair, the subsequent excitation pulse may raise the energy of an already existing exciton resulting in a *hot exciton*. It has been shown in several different NC structures that hot excitons may get trapped on the nanocrystal surface.[37] If the electron is trapped, it results in a positively charged QD and vice-versa. Alternatively, multiple excitons generated by the initial excitation pulse may recombine by a fast non-radiative process called *auger recombination* that would also result in formation of charged QDs. These charged QDs can further be photo-excited to form positively or negatively charged excitons, also known as *trions*. Trions were initially thought to be non-emissive or very weakly emissive and were suggested to be responsible for the *off* state in QD blinking.[38]

It is clear from the Figure 1.6 that photo- excitation in QDs leads to a whole gamut of singly and multiply excited states that includes single or multiple excitons, hot excitons, charged excitons etc. Chapter 4 and 5 will discuss in more detail, the study spectral and dynamical properties of multi-excited (MX) states in colloidal QDs.

1.4.2 Spectroscopy and challenges

Semiconductor NCs exhibit complicated single exciton decay dynamics which are very sensitive to surface chemistry and chemical surroundings.[41] Multi-excited (MX) decay dynamics are even more sensitive to NC size, shape and composition and can therefore be easily perturbed by high photo-excitation intensity. The majority of optical and electronic spectroscopy work in colloidal NCs so far has focused mostly on lowest energy single exciton photo-physics.[37] It is therefore important to study the structure and dynamics of MXs in colloidal QDs in order to harness the true potential of semiconductor nanocrystals. Therefore, necessitating the development and use of new spectroscopic techniques, which can inject multiple electron hole pairs in a NC without exposing it to high photo-excitation intensity or energy.

Femtosecond transient absorption (TA) and time resolved photoluminescence (TRPL) spectroscopy has been the mainstay to probe exciton dynamics in QDs.[40–43] TA has very high temporal resolution and can probe intra-band exciton dynamics but suffers from high background noise therefore usually requires high excitation intensity to obtain a good signal-to-noise ratio. Also, practical considerations on probe pulse delay in TA makes it difficult to probe long lived multi-excitonic states, especially seen in “giant” CdSe/CdS core-shell NCs.[44] On the other hand, time resolved PL spectroscopy has a very low background noise, requires just a single excitation laser and instrumentation is comparatively simple. However both TA and TRPL are susceptible to extraneous signals which could be mistaken for MX decay.[45] Although origin of this artifact is still unclear[45], it’s thought to arise from photo-charged dots especially in domain of high excitation intensity and has been a source of confusion and controversy for calculating correct MX quantum yields and associated spectroscopic signatures.[34, 37–39]

On the other hand, fluorescence confocal microscopy on single nanocrystals has enabled us to separate the effect of inhomogeneous broadening in ensemble samples due to variation in size, shape, or environment of nanocrystals. Single particle spectroscopy has also revealed several new features in QD photo-physics such as fluorescence blinking, ultra-narrow emission line widths, and spectral diffusion of emission linewidth. Further, multiple exciton emission can also be directly inferred by photon correlation measurements using single molecule techniques.[40] However, single particle fluorescence microscopy suffers from user-selection bias towards bright QDs, poor sample statistics, and photo bleaching of the sample, and is also vulnerable to charging related artifacts as in ultrafast techniques described previously.

1.4.3 Motivation and thesis outline

In 2004, Schaller and Klimov[50] for the first time demonstrated efficient multiple exciton generation (MEG) in semiconductor NCs and later, in 2011, a QD solar cell exploiting the concept of MEG efficiency was demonstrated having more than 100% peak external quantum efficiency.[51] Therefore the potential of MEG based solar cells to make a big leap in photo-conversion efficiency has intensified scientific interest in study of multi-excitons in colloidal NCs. The MEG is equally important for practical realization of optical gain in NC based lasers[25,40] or using NCs as entangled photon sources.[52,53] On the other hand, multiple exciton recombination,[43,54] reverse of MEG, is thought to play a key role in NC blinking and NC photo charging, and its understanding has important implications for using NCs as reliable biomarkers,[55,56] bright LEDs[57] or single photon sources.[56,57]

The fluorescent yield of multi-excited states is often small and their lifetimes can be comparable to fast decay components in multi-exponential exciton decays. It is therefore often challenging to differentiate multi- from singly-excited states using conventional spectroscopy techniques discussed in the previous section. The primary focus of my research has been to develop ensemble techniques based on time resolved fluorescence that are able to reliably distinguish multi- from singly-excited states, even in the limit of low fluorescence yield. Thus, a significant portion of this thesis details some of the new spectroscopic and analytical techniques that I have developed to study spectral and dynamical properties of multi-excited states in colloidal QDs.

Next, we need to understand how the shape, structure and surroundings of QDs affects its photo physics, particularly, properties and dynamics of multi-excited states. Therefore, the next important goal is to apply both conventional and newly developed spectroscopic techniques to different QD materials and systems.

Several interesting experiments that don't involve complex synthetic protocols like modification of surface ligands on QDs or varying the shell thickness or shell material in case of core-shell QDs could be performed to obtain essential exciton structure and dynamics. However, a very interesting system would be the QD-metal nanoparticle assembly. Metal-semiconductor nanostructures would be an ideal platform to control light and charge transfer at nanoscale for various applications such as sensing, photovoltaic devices, light emitters and catalysis.

In the weak coupling regime, the exciton dipole of the QD can couple with light-induced electronic excitations, known as *surface plasmons*, in the metal nanoparticles (NPs). Plasmon-exciton interaction has been shown to affect the optical absorption and fluorescence emission rates in QDs.[42] Several reports including one[59] recently published by our group have shown the potential of multi-exciton emission enhancement via coupling to plasmon modes of Au films. The latter part of thesis particularly chapters 5 and 6 will discuss interaction of metal nanoparticles with QDs, construction of hybrid films of QD/Au NPs separated by poly-electrolyte spacers of varying thickness, spectroscopy of such hybrid devices, and, particularly the effect of plasmon coupling on multi-excited state dynamics in quantum dots.

CHAPTER 2 : TIME-RESOLVED SPECTROSCOPY SYSTEM

Time resolved Photoluminescence (TRPL) has been one of the key experiments to probe exciton dynamics in quantum dots. TRPL is an extremely sensitive technique since it's a zero background measurement, and can probe samples with very low photo-excitation intensities. TRPL can be easily coupled with a microscopy setup to study photo-excitation of single nanocrystals. Further, TRPL has a very high dynamic range and can measure dynamics ranging from few picoseconds to tens of seconds.

2.1 Time correlated single photon counting (TCSPC)

TCSPC has been the standard practice to time-resolve PL decays since the late 70's. Single photon counting is based on the basic principle of reconstructing the probability distribution function of photon emission by sampling one photon at a time following a large number of excitation cycles.

Figure 2.1 describes the basic layout of a typical TCSPC system. A pulsed excitation source such as a laser or a LED excites the sample, and also generates a reference timing pulse *correlated in time* with the optical pulse. The reference pulse is sent through a constant function discriminator (CFD). The CFD is used to remove any amplitude jitter in the timing signal that may result from amplification gain or some other source of electronic noise. The reference pulse after passing through the CFD starts a TAC (Time-to-amplitude convertor) which initiates charging of a capacitor. The charging ramp of the capacitor in the TAC is stopped by a timing signal sent by the photo-detector after detecting fluorescence. The TAC generates an output pulse that is proportional to the time difference between START and STOP pulses. The TAC pulse can be routed through a biased amplifier (AMP) if needed, and is then sent to an analogue-to-digital converter (ADC) that converts the TAC voltage into a digital numerical value. The ADC output is used to increment a counter corresponding to the delay time in a data memory, and by repeating this process, a histogram of number of photon counts can be built up.

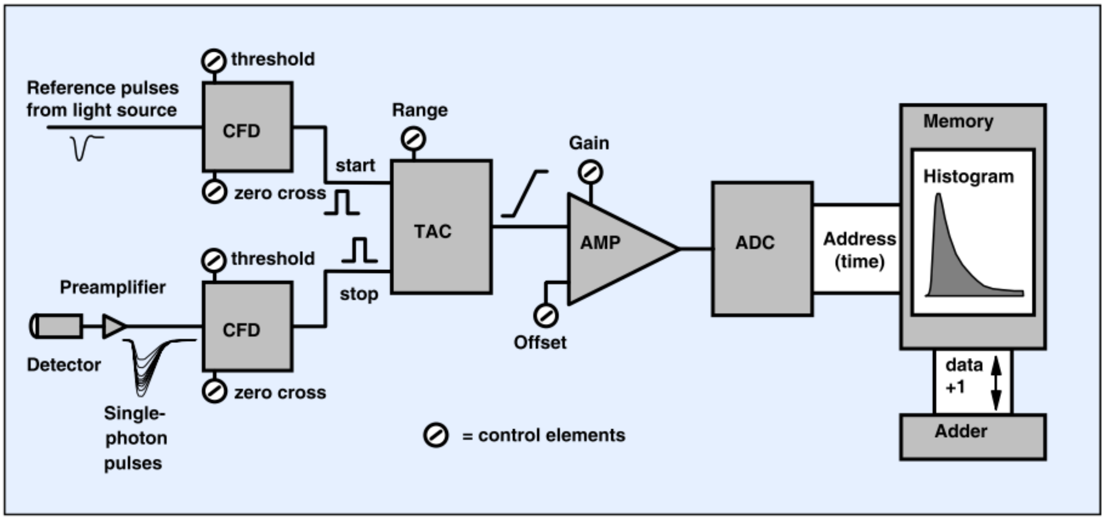

Figure 2.1: Elements of a classical TCSPC system. Reproduced from reference.[60]

2.1.1 Detection count and pulse pile-up

The detection count rate is normally adjusted to one percent of the excitation rate, i.e., only one photon per 100 excitation events is recorded. This is because, the photon-counting electronics typically have a dead time on the order of few hundred nanoseconds whereas fluorescence decays on a much faster timescale. Therefore, we keep the emission intensity, using neutral density filters before the detector, low enough that at-most only one photon is detected per excitation cycle. If the detected count rate is high, then there will be several photons in a given time window, but the TAC will be stopped by the first arriving photon, thus the recorded intensity decay would be biased towards early arriving photons, and would be distorted to shorter lifetimes. This phenomenon is called *pulse pile-up*. However, it has been shown that measured lifetimes change by as little as 1% even for counts rate as high as 10% of the excitation rate.[61] Nonetheless, we have been overcautious and all the data presented in this thesis has been collected for count rates less than 1% of the excitation rate.

2.1.2 Reverse Start-stop

As discussed in the previous section, in a TCSPC experiment, the collection rate is kept much lower than excitation rate thus there are many time-periods in which no photon is collected. In these periods, the TAC is started but not stopped, and the TAC resets for the next signal period. This may cause a problem if we are working with high repetition rate light sources, as frequent TAC resets might lead us to miss a rare detection event. Therefore, most TCSPC experiments are performed in a reverse start-stop mode. In reverse mode, the TAC is started by the detected photon and stopped with the next reference pulse. We can also delay the reference pulse by an appropriate amount to measure time of photon against the laser pulse from which it originated.

2.1.3 Deconvolution

The lifetime decay obtained in a TCSPC experiment is actually a convolution of sample's true decay with excitation profile of the light source, and response of the detection system. Therefore, we need to separately record the response of the TSCPSC system to excitation light in the absence of fluorophore, and is known as the instrument response function (IRF). The IRF is mostly recorded by collecting the scattered light from the sample near the excitation wavelength.

2.2 Development of ultrafast time-resolved PL system

Quantum dots depending on the material and nanocrystal size can have a wide optical bandgap range[7] that can be tuned from ultraviolet to near infrared absorption. In addition, semiconductor nanocrystals exhibit very complex decay dynamics, which occur over a wide timescale ranging from a few picoseconds to several microseconds.[62] Therefore, we need a very flexible and adaptable laser spectroscopy system.

Figure 2.2 shows the ultrafast laser spectroscopy system that we have built to study light-induced charge and energy transfer dynamics in semiconductor nanocrystals. The entire table is home assembled and it has taken us several iterations to find the right optical layout of our components. Most important, several key electronic and optical components like the OPO laser, electro-optical modulators, hybrid PMT detectors, and photon counting cards were newly introduced products when we purchased them. It took a long time and a sustained effort that included calibrating and testing the optical and electronic components first individually, then on a system level and countless back and forth discussions with different manufacturers to get everything working as a single unit. The entire effort has been really painstaking and time consuming. However, the kind and scope of experiments we had planned required us to build a flexible laser spectroscopy system with a very high signal to noise ratio.

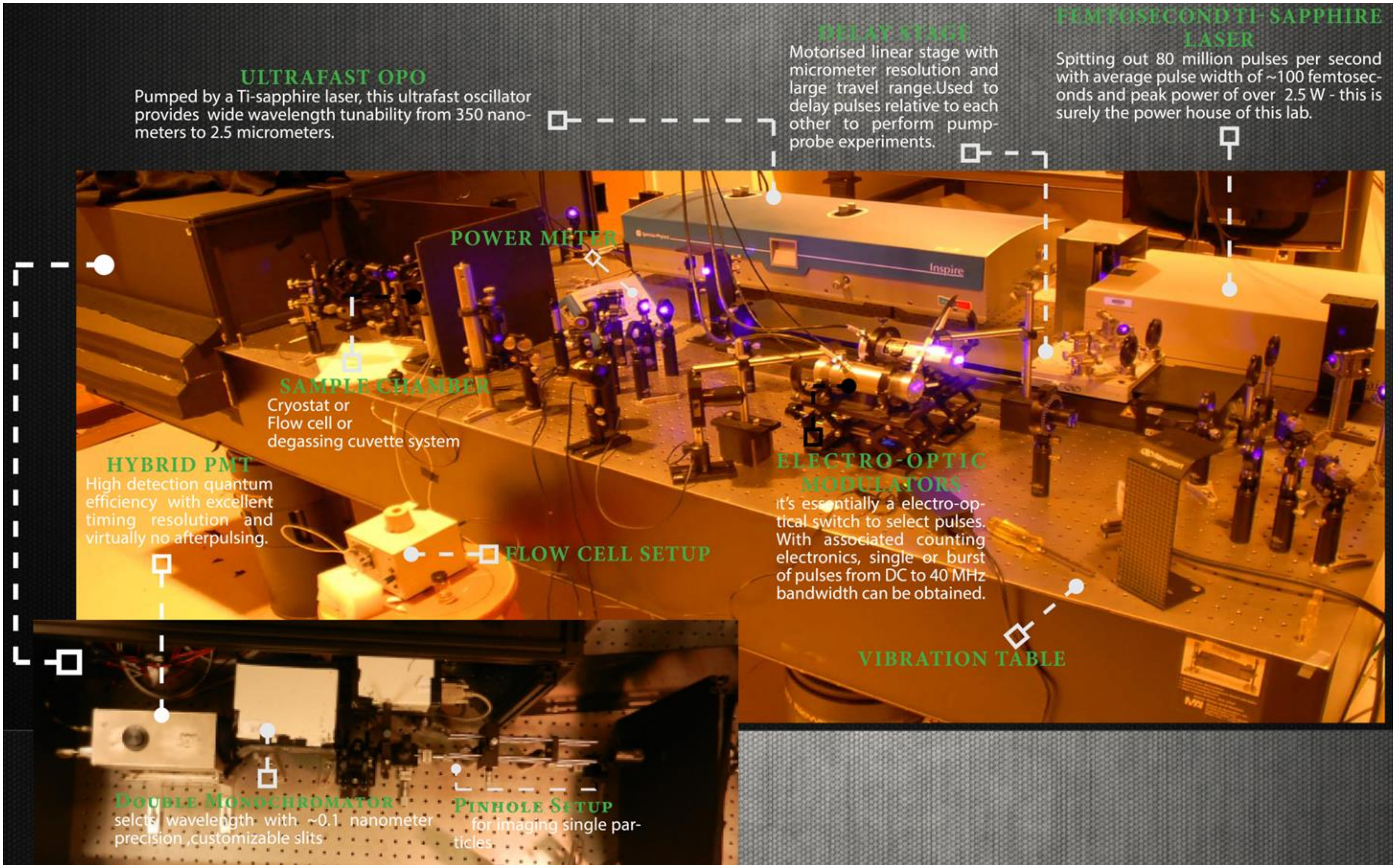

ULTRAFAST OPO

Pumped by a Ti-sapphire laser, this ultrafast oscillator provides wide wavelength tunability from 350 nanometers to 2.5 micrometers.

DELAY STAGE

Motorised linear stage with micrometer resolution and large travel range.Used to delay pulses relative to each other to perform pump-probe experiments.

FEMTOSECOND TI-SAPPHIRE LASER

Spitting out 80 million pulses per second with average pulse width of ~100 femtoseconds and peak power of over 2.5 W - this is surely the power house of this lab.

POWER METER

SAMPLE CHAMBER

Cryostat or
Flow cell or
degassing cuvette system

HYBRID PMT

High detection quantum efficiency with excellent timing resolution and virtually no afterpulsing.

FLOW CELL SETUP

ELECTRO-OPTIC MODULATORS

it's essentially a electro-optical switch to select pulses. With associated counting electronics, single or burst of pulses from DC to 40 MHz bandwidth can be obtained.

VIBRATION TABLE

DOUBLE MONOCHROMATOR

selcts wavelength with ~0.1 nanometer precision ,customizable slits

PINHOLE SETUP

for imaging single particles.

Figure 2.2 : A side view of the home built laser spectroscopy table.

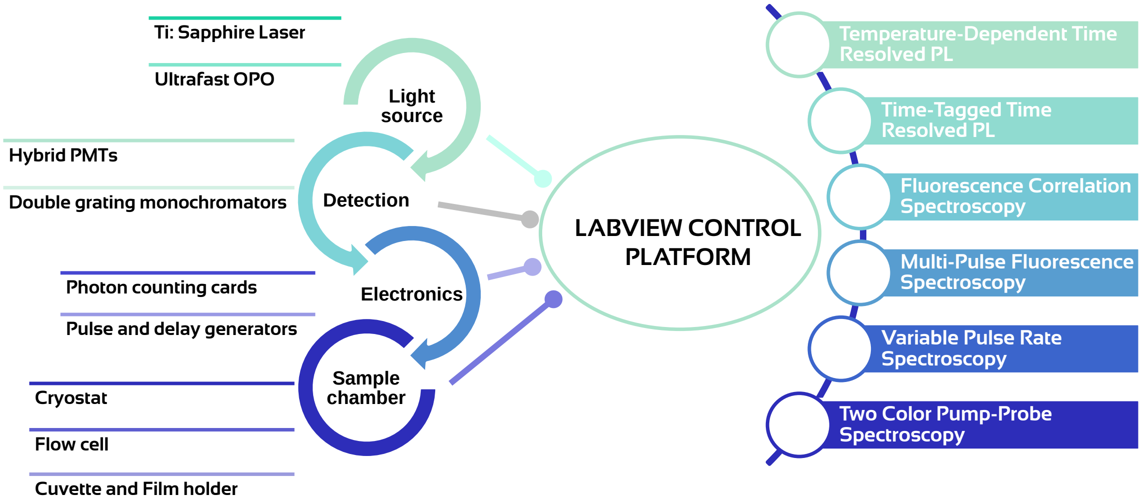

Figure 2.3 : Functional layout of the laser spectroscopy system.

The laser spectroscopy system can be further decomposed into following functional sub-systems (shown in Figure 2.3):

2.2.1 Light source

The fundamental light source in our spectroscopy system is a mode-locked femtosecond Titanium: Sapphire (Spectra Physics MaiTai HP) laser pumping at 80 MHz. The pulse width is on the order of ~100 fs with peak average power around 2.5 W at 820 nm. The tuning range for this laser is between 700 nm-1000 nm. In order to access the visible and far infrared spectrum, the MaiTai is used to drive an optical parametric oscillator (OPO) (Spectra Physics Inspire). This combination gives us a gap-free tuning range from 345 nm to 2.5 μm.

2.2.2 Pulse modulation system

The pulse repetition rate of the native laser system is much higher than what is typically required for single photon counting (< 1 MHz). This is achieved by using two electro-optic modulators (Conoptics 350-105 KD*P Series) arranged in series. The electro-optic modulators used in our system are essentially voltage controlled waveplates that work by using the Pockels effect i.e. birefringence is linearly proportional to applied voltage. Further, by arranging the modulators in series, we are able to achieve light modulation with net extinction ratios greater than 100,000:1. Such kind of serially connected E-O modulators are custom- designed, and are somewhat difficult to use as they present considerable challenges in electronically and optically syncing both the modulators to work in tandem. However, we are interested in resolving low yield but long living decay components in quantum-dot fluorescence. This long time window requirement restricts us to use slow pulse repetition rates on the order ~100 KHz. Therefore, we have to record fluorescence over long periods to get good statistics, and thus required us to have high signal-to-noise ratios.

2.2.3 Photon counting

We have two photon counting cards that can be simultaneously triggered by the Laser SYNC (reference), and record short and long dynamics at the same time. The first one is called SPC-130 (Becker-Hickl) and is a standard TCSPC module. The second one is called DPC-230; is a dual-channel photon correlator, and is usually used by us to record the long microsecond dynamics as the SPC-130 uses a TAC (based on charging capacitor) based timing mechanism which can go up to only 2 microseconds.

Further, although both the counting module are LabVIEW compatible but the drivers to run them in parallel weren’t provided by the manufacturer therefore we had to spend some amount of time to write specialized code in order to communicate with both the modules at the same time.

2.2.4 Software

As described above, the entire laser spectroscopy system is custom built by using several different opto-electronic components, and therefore we had to build our own software platform to control and coordinate various individual systems. The software platform is developed using LabVIEW, which is a visual programming language, created by national instruments, and is a very popular programming environment for laboratory automation and measurement.[46] There are currently two different LabVIEW routines used in our lab, one developed for temperature-dependent time-resolved PL experiments and another one built for multi-pulse experiments.

Apart from automating data collection, a customized software platform allows us to perform complex yet powerful experiments involving collecting/analyzing data as a function of several tunable parameters, which is not possible from an out of the box system with a fixed software platform.

CHAPTER 3 : TEMPERATURE-TIME-RESOLVED PHOTOLUMINESCENCE

3.1 Motivation

In core-shell quantum dots[32], the inorganic shell protects the optically active core from its surrounding environment and the surface traps that result in enhanced fluorescence quantum yields and photo-stability. Recently, it was found that QDs with thick shell up to 16 monolayers (termed as "Giant" QDs[47]) also have enhanced multi-exciton emission efficiencies[44] and suppressed blinking.[48] Therefore, we wanted to study and understand the exciton dynamics in core-shell QDs as a function of shell thickness. We used temperature dependent time–resolved photoluminescence[49] (PL) to study decay dynamics over five orders of time scales ranging from picoseconds to microseconds. We also present a quantitative model of charge carrier trapping based on Marcus electron –transfer theory that closely fits PL decays over the entire range of time scales and temperatures (ranging from 77 K up to 300 K).[45]

3.2 Experimental methods

3.2.1 QD sample preparation

We utilized a procedure developed by Clapp et al.[50] to synthesize CdSe quantum dots. A SILAR method first introduced by Li et al.[51] was then employed to grow CdS shells on as-prepared CdSe cores.

Table 3.1: QD sample parameters used in this study.

Sample Name	Core size (nm)	Shell monolayers	Shell thickness (nm)	Peak Emission (nm)	Quantum yield (%)
Thin shell	2	6.25	2.5	619	10.1%
Thick shell	2	9.25	4.1	638	20.3%

The average thickness of one monolayer (ML) of CdS was taken as 0.35 nm, which is equal to half the c-lattice parameter of the bulk CdS. After the growth of each monolayer a small aliquot was taken out for optical measurements.

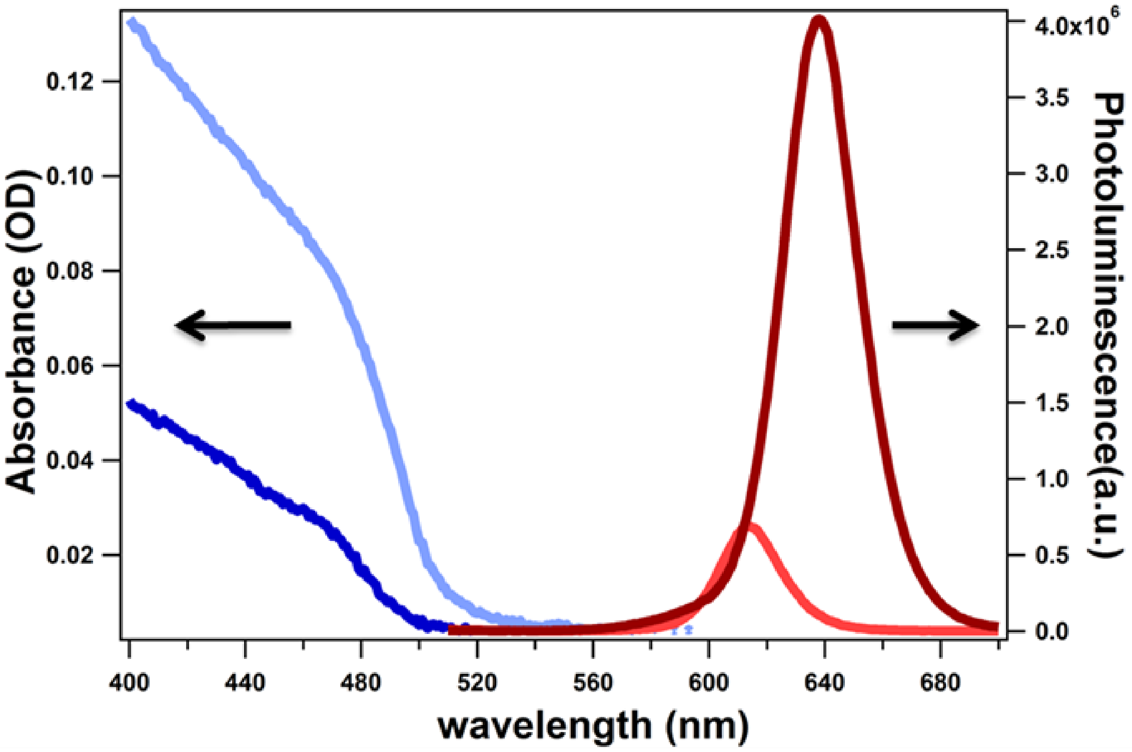

Figure 3.1: Absorbance and emission intensity for CdSe/CdS (6.25 ML) (purple and red, respectively) and CdSe/CdS (9.25 ML) (blue and dark brown, respectively) QDs.

In this study, two samples corresponding to 6.25 ML (thin shell) and 9.25 ML (thick shell) of CdS shell thickness were used for subsequent measurements. Table 3.1 lists the general details of the samples used in this study. The resulting core-shell dots were then purified by precipitating them with acetone or methanol and then re-dispersed in hexane. Figure 3.1 shows the typical UV-Vis absorption and steady-state emission spectra for the CdSe/CdS core-shell QDs used in this study. Photoluminescence peak red shifts for the thicker shell QD on the account of exciton delocalization as the size of QD shell increases.

3.2.2 Single Photon Counting

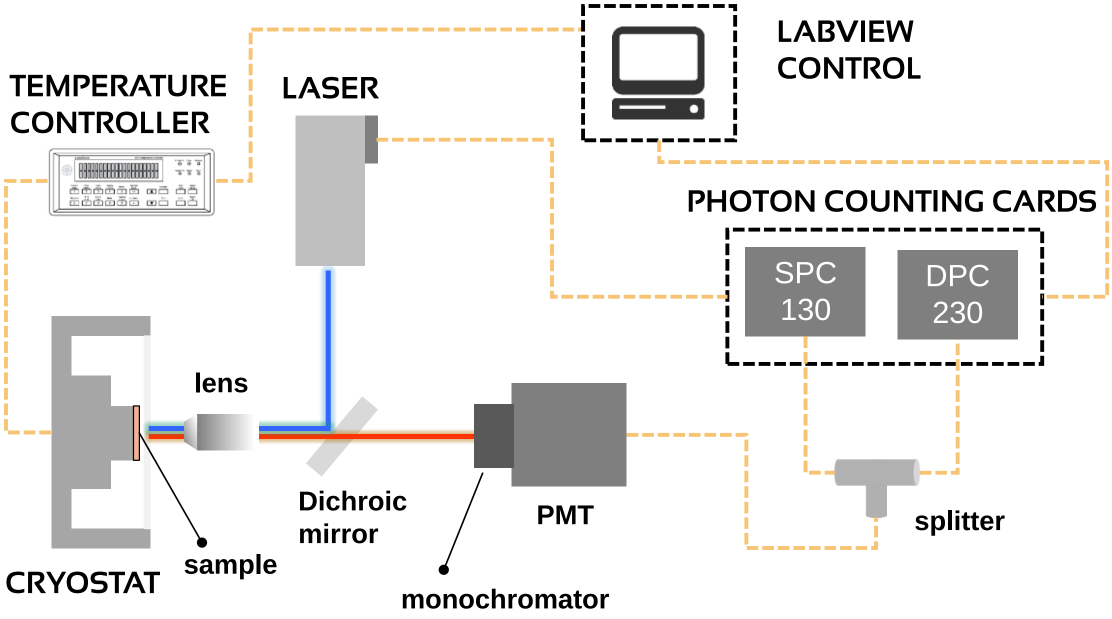

Figure 3.2: Simplified schematic for the temperature-time resolved PL setup.

Time correlated single photon counting[52] (TCSPC) was used to record PL dynamics. To ensure accurate determination of both short and long decay components, two counting modules, SPC 130 and DPC 230 respectively, were used to record both short time window (50 ns) and long-time window (10μs) PL dynamics. The liquid nitrogen cooled cryostat (ST 500) coupled with a temperature controller was used to collect the PL decays as a function of temperature from 77 K to 298 K in 12 K increments.

Mode-locked femtosecond Ti:sapphire laser (Spectra Physics MaiTai), operating at 80 MHz repetition rate and 820 nm, was used as a synchronous pump source for the optical parametric oscillator (INSPIRE OPO). The frequency-doubled output (410 nm) from the OPO was then directed through the pulse-picker system, as described in chapter 2, to reduce the laser repetition rate to 100 kHz.

The pulse-picked frequency doubled light was then focused on the cryostat window, containing the QD sample, using a 500 mm uncoated plano-convex lens from Newport mounted on a XYZ stage. We then collected the sample fluorescence using the same lens, separated from the scattered laser light by a dichroic beam splitter (Semrock FF01-480) and a subtractive double monochromator (Spectral Products CM112). It was then detected by the hybrid PMT (Becker&Hickl HPM-100-40).

The home built LabVIEW software platform was used to collect the data automatically over the entire temperature range. The software changed the temperature, waited for the new temperature point to stabilize, adjusted the monochromator wavelength to remain coincident with the peak of the steady-state PL emission, initialized the photon-counting cards and collected the required number of photons, stopped the measurement, and saved data before moving on to the next temperature point.

Steady state emission was collected using a Jobin-Yvon Fluorolog 3 fluorimeter with a Hamamatsu R928 PMT detector. Absorbance measurements were made using a Cary 50 UV–vis spectrometer.

3.2.3 Data Analysis

For each temperature setting, a pair of short and long decays was fitted simultaneously with a single decay function using iterative least-squares method. The decay function is modeled by an N-component multi-exponential function that is reconvoluted with two instrument response functions (IRFs), one each for short and long time windows, to fit the pair of decays.[62] The IRFs are measured by collecting scattered light from the sample near the laser wavelength without changing the optical setup.

The quality of fit is determined by two statistical tests, reduced chi square (χ_r^2), and the Durbin-Watson factor (d^w). For a good fit, it has been shown previously[62] that reduced chi-square values should be close to 1, and Durbin- Watson parameter, should have a value around 2. All the data presented here is fitted to ensure that $\chi_r^2 < 1.1$ and $|d^w - 0.05| < 2$.

Further, we can calculate average fluorescence lifetimes, $\langle\tau\rangle$, for each multi-exponential decay by the following equation,[66]

$$\langle\tau\rangle = \sum_n \frac{\alpha_n \tau_n^2}{\sum \alpha_m \tau_m} \tag{3.1}$$

3.2.4 Kinetic model

Exciton states in QDs couple with surface trap states that result in one of the charge carriers getting localized at the surface or at another interface (such as between the core and the shell in a core-shell QD), and that leads to spreading of PL dynamics over several microseconds.[56] Charge trapping (whether it is electron or hole trapping) can be modeled as a classical Marcus electron transfer reaction.[39] In Marcus theory framework, electron transfer (ET) from an exciton state to a trap state would depend on the free-energy difference, ΔG, for the charge transfer, the reorganization energy, λ, required to distort the QD and its local environment until it can accept the transferred charge distribution, and

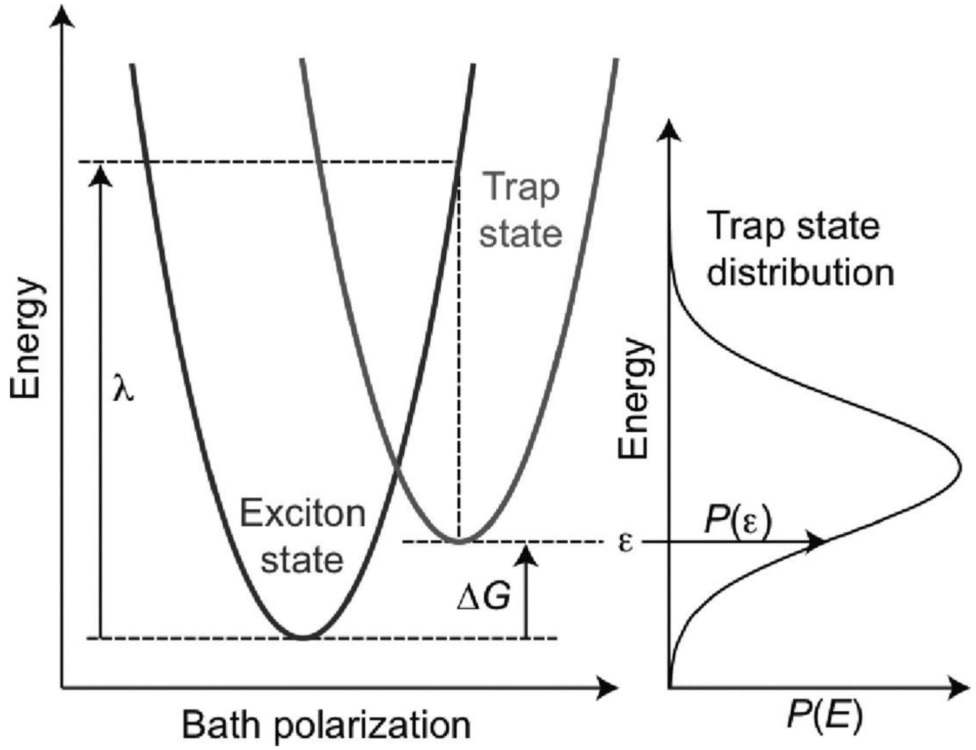

Figure 3.3 : A simple schematic depicting charge transfer by Marcus theory.

electron coupling, V, between the donor exciton states and the acceptor trap states (see Figure 3.3).

Each QD can have several discrete trap states, however, in an ensemble of QDs, we can define a trap distribution, $P_K(\varepsilon)$ with a single value of reorganization energy (λ_k) and electronic coupling parameter(V_k) for all the transitions from K^{th} trap distribution to QD exciton states. This allows us to use the spherical symmetry of QDs to treat trap states as narrow radial bands lying at the nanocrystal interfaces. Nevertheless, it's still a challenge to determine the mathematical form for such a trap distribution in semiconductor NCs which have discrete exciton states. In organic photoconductors, trap state energies are described by a Gaussian distribution[71] whereas in bulk semiconductors, an exponential distribution of trap energies is usually preferred. In this study, following the work by Jones et al,[39] the trap sate distribution is defined as a convolution of Gaussian and exponential functions, and is defined as follows:

$$P_K(\varepsilon) = A_K \int_0^\infty exp\left(-\frac{(E-\varepsilon_K)^2}{2\sigma_K^2}\right) exp\left(-\frac{\varepsilon_K - (\varepsilon - K)}{\alpha_K}\right) dE \tag{3.2}$$

where $\varepsilon_K$is the peak energy of the Gaussian distribution, σ_K is its width, α_K is the exponential decay constant, and A_K is a normalization factor. Following the Marcus theory outlined above, we can define trapping rates from exciton state, i, to trap states in the K^{th} trap distribution:

$$k_{iK} = g_K P_K(\varepsilon) \frac{2\pi |V_K|^2}{\hbar} \sqrt{\frac{1}{4\pi\lambda_B k_B T}} \exp\left(\frac{-(\Delta G_{iK}(\varepsilon) + \lambda_K)^2}{4\lambda_B k_B T}\right) \tag{3.3}$$

The reverse rates are given by:

$$k_{Ki} = \frac{g_i}{g_K P_K(\varepsilon)} k_{iK} \exp\left(\frac{-\Delta G_{iK}(\varepsilon)}{k_B T}\right) \tag{3.4}$$

where g_i and g_K are, respectively, the degeneracy of the i^{th} exciton state and the average number of trap sites in the K^{th} trap distribution.

Following the framework described above, we can then define a kinetic scheme with N states. The number of states, N, is given by:

$$N = Ground\ state + exciton\ states + \sum_k N_K$$

where N_K is the number of trap states used to approximate the K^{th} "continuous" ensemble trap distribution. Following the treatment by Jones et al, it was found sufficient to set N_K such that the spacing between consecutive trap states was less than 5 meV.

We then modeled exciton dynamics by calculating probability, $\rho_n(t)$, of populating *n*th exciton state at time t after excitation. The values of $\rho_n(t)$ are calculated by numerically solving a series of N rate equations:

$$\frac{d\rho_n(t)}{dt} = -\gamma_n^R \rho_n(t) + \sum_{m \neq n} \left(\gamma_{mn}^{NR} \rho_m(t) - \gamma_{nm}^{NR} \rho_n(t)\right) \tag{3.5}$$

where γ_{mn}^{NR} (γ_{nm}^{NR}) are the non-radiative transition rates from state *m (n)* to state *n (m)*, and γ_n^R is the radiative transition rate from state *n*.

We have used the software developed by Jones et al[39] for the analysis of time-resolved PL decays at different temperatures. Using this software, we can build any arbitrary first-order kinetic scheme, assign initial populations, and propagate the dynamics over a set of time interval.

3.3 Results and discussion

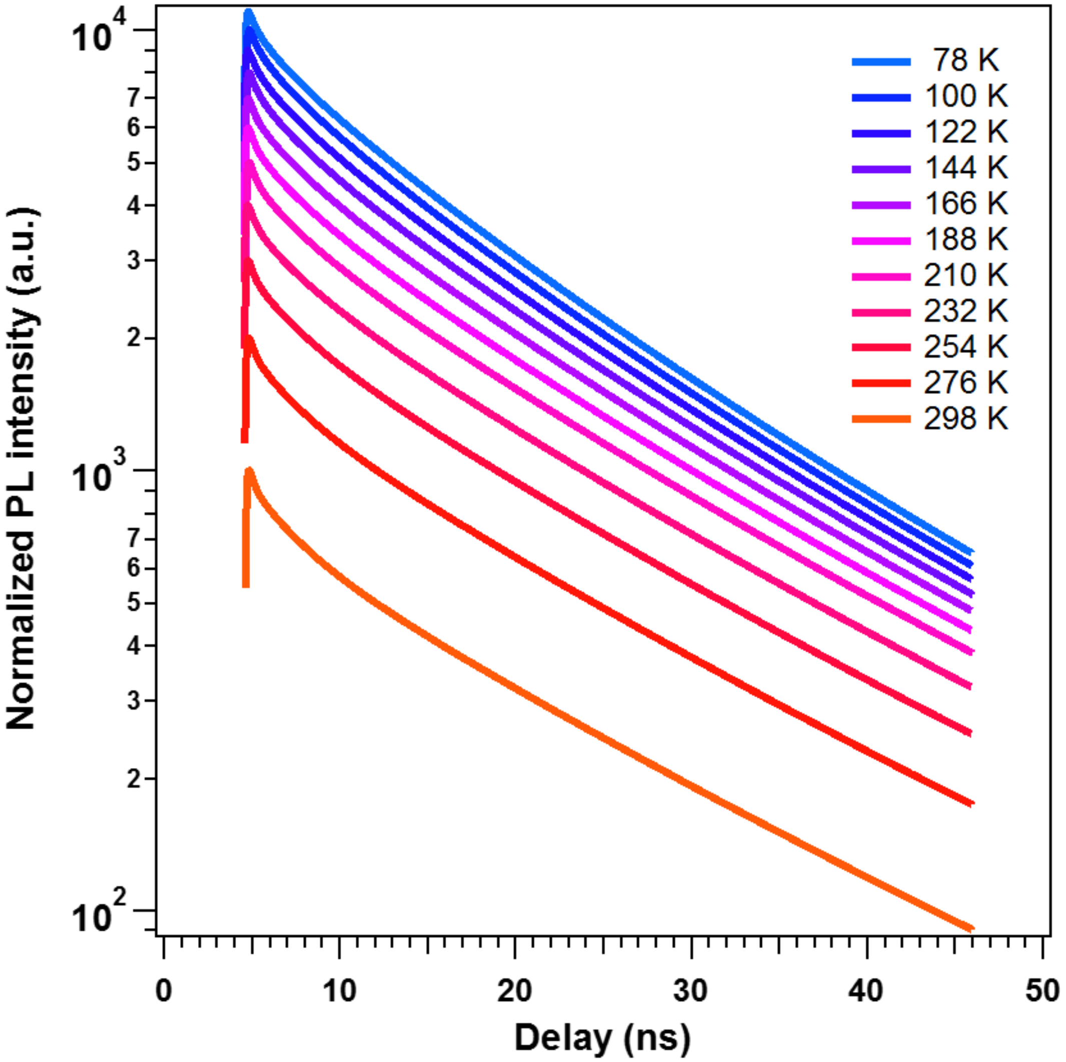

Figure 3.4: PL transients recorded as a function of temperature (77 K-298 K) for thin shell QDs over 50 ns.

Figure 3.4 shows the fitted decays for thin-shell QD sample collected over a time window of 50 ns at 11 different temperatures ranging from 77 K to 298 K.

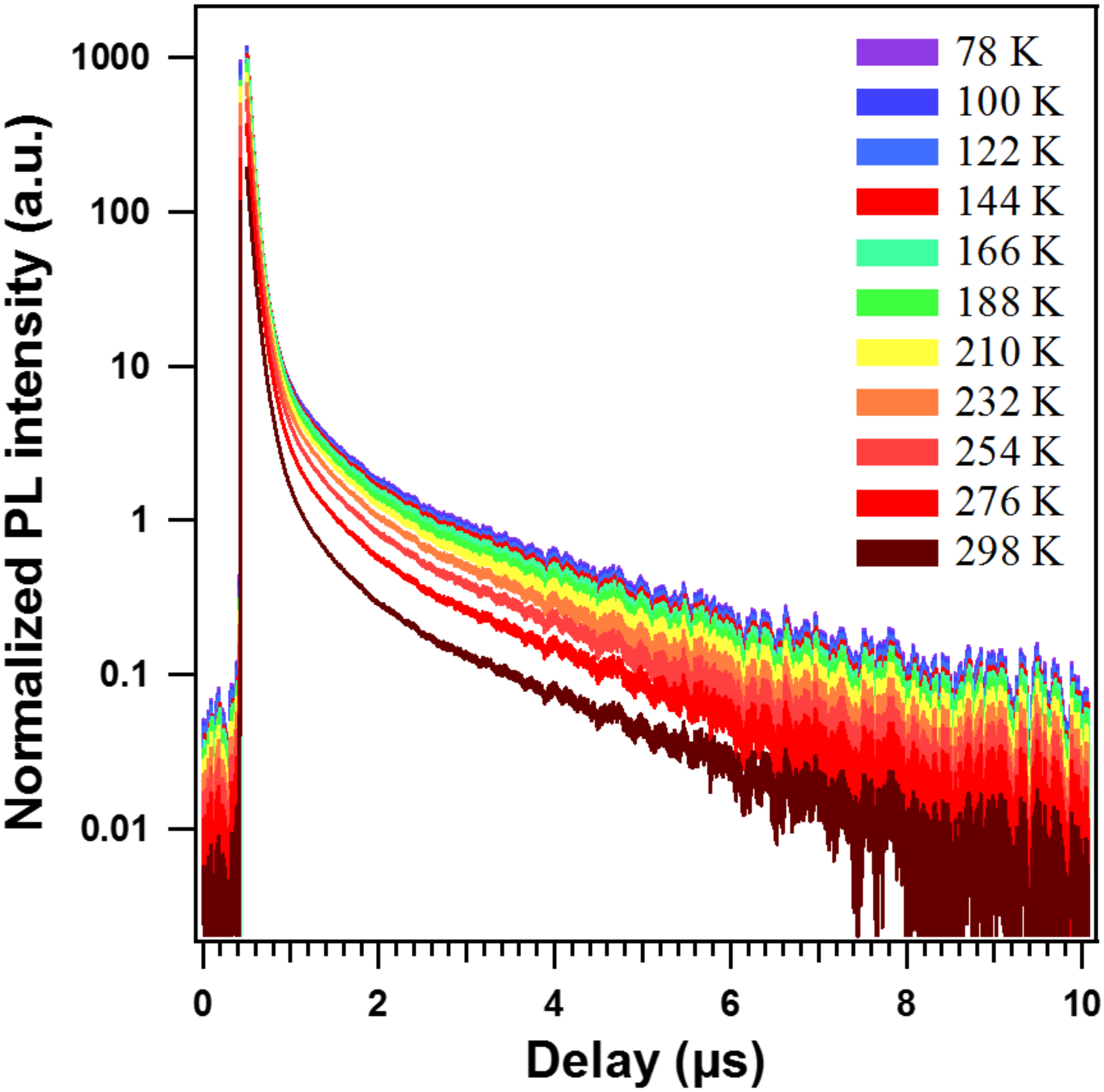

Figure 3.5: PL transients recorded as a function of temperature (77 K-298 K) for thin shell QDs over 10 µs.

The normalized decays are displayed in a staggered fashion for ease of viewing. For the same sample, Figure 3.5 shows the dataset collected over a longer time period of 10 µs. Each PL decay pair at a given temperature was analyzed by a single multi-exponential function as described in section 3.2.3.

Similar fitting procedure was also adopted for the thick shell sample, and corresponding short and long PL decay components are shown in Figure 3.6 and 3.7. Clearly, the shape of PL decays changes both with the temperature and the collection time window.

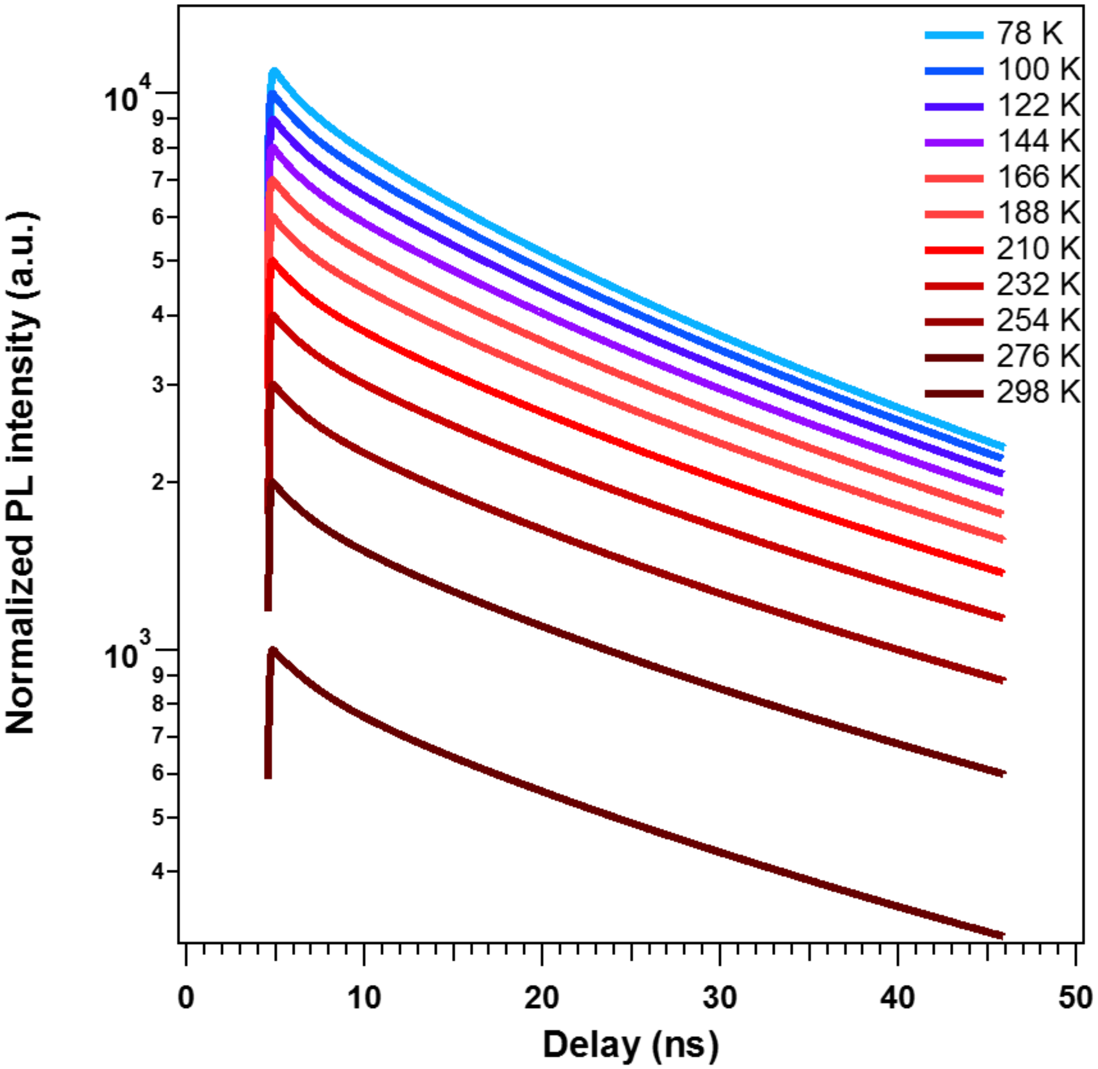

Figure 3.6: PL transients recorded as a function of temperature (77 K-298 K) for thick shell QDs over 50 ns.

First, the PL decays are multi-exponential and last for several µs (Figure 3.5 and 3.7) which is several orders of magnitude longer than the ≈20 ns lifetime of the optically active exciton states responsible for PL in CdSe QDs.[53] Although, in CdSe QDs, there is a "dark" state with a PL lifetime of ≈1 µs[54] situated below the bright exciton state, however the bright-dark exciton splitting is just a few meVs[55] which is easily overcome by the thermal energy at 77- 298 K temperature range in our experiment, and therefore the dark state cannot account for long PL decay tails. However, we do know that semiconductor nanocrystals have surface traps on account of dangling bonds and defect sites[75,76] that can couple with exciton states leading to long lived trap mediated photoluminescence. Several studies[39,62,66,77] have firmly established that exciton-trap interactions are the primary mechanism that controls the dynamics of band-edge excitons in QDs and gives rise to complex multi-exponential decays.

Further, irrespective of the shell thickness, over the short (50 ns) time window, PL decays became progressively longer as the sample temperature was increased. This trend would be consistent with a reversible charge trapping and de-trapping mechanism that is thermally activated. However, over a longer time window (10 µs), the evolution of PL decay profile with temperature was found to be sensitive to QD shell thickness. For the thin shell QDs, PL decays became progressively faster with increase in temperature (Figure 3.5) whereas the trend was completely opposite for the thick-shell QDs (Figure 3.7).

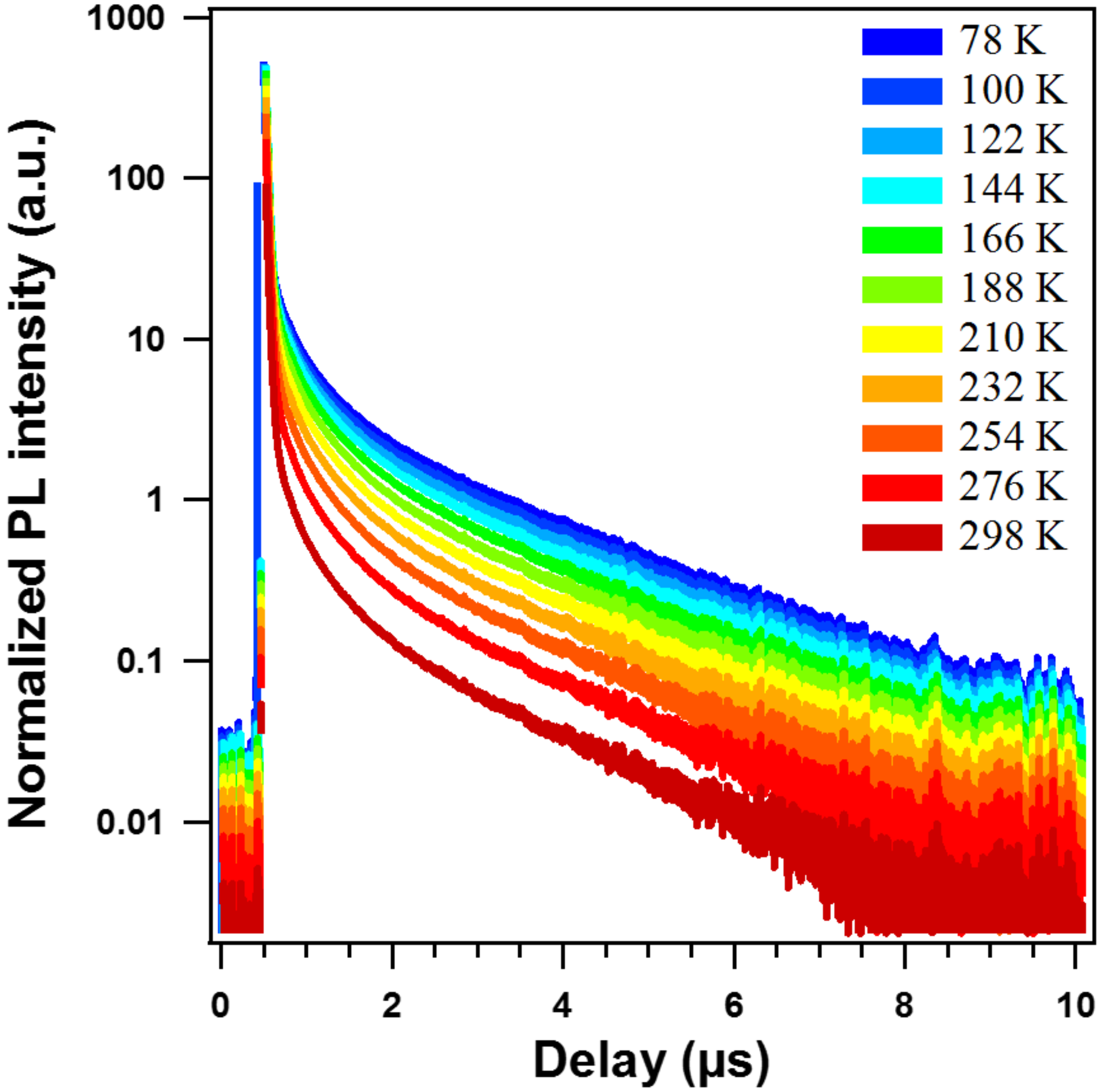

Figure 3.7: PL transients recorded as a function of temperature (77 K-298 K) for thick shell QDs over 10 µs.

First, this shows that the timescale over which PL dynamics are recorded plays a crucial role in understanding the photo-physics of charge carriers in nanocrystals. And, this validates our approach of measuring both short and long time dynamics. Second, temperature dependence of PL dynamics excludes quantum tunneling as a possible mechanism for charge transfer because electron/hole tunneling should be independent of temperature.[78] Further, the fact that long tails in PL decays strongly depend both on the temperature, and the shell thickness point towards a distribution of activation barriers for the trapping/de-trapping processes, and suggests one or more trap distributions with different re-organization energies and coupling parameters[79] could be responsible for changes in PL dynamics.

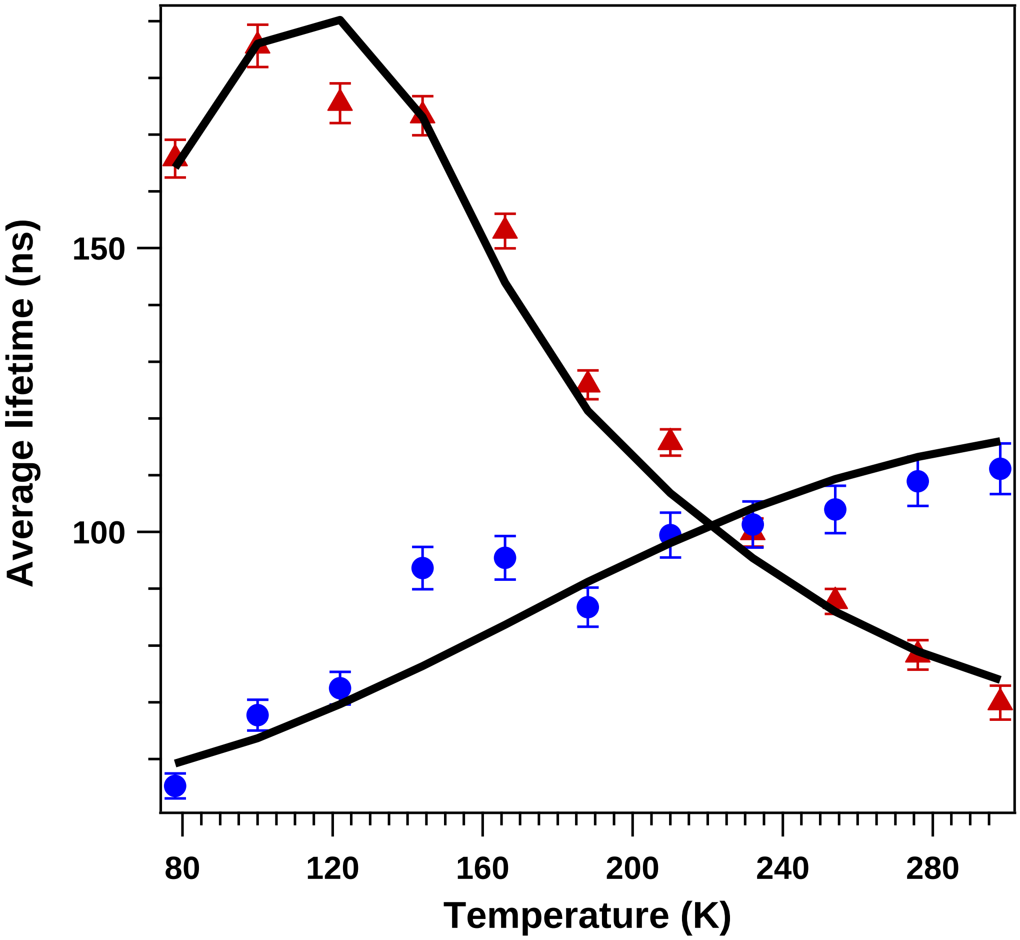

Figure 3.8: Average lifetimes plotted as a function of temperature for thin shell (red, triangles) and thick shell (blue, circles) QDs. In each case, the error bars are ±2 × the standard deviation. The procedure for estimating errors is discussed in Appendix A. The solid black lines are fits constructed from lifetime values calculated using the kinetic model shown in Figure 3.9 and 3.11.

Further, using the eq. 3.1 described in section 3.2.3, average lifetimes for both the samples are calculated, and plotted as a function of temperature (as shown in Figure 3.8). The average lifetime data resolved with temperature, along with PL transients can be highly informative, and predict the basic nature of physical processes happening in the QDs.

First, the average lifetime at 77K for the thin shelled QDs (165 ns) was almost three times as big as that for the thick-shell sample (54 ns). This clearly indicates presence of trap states or a trap distribution very close in energy with the exciton state in thin shelled QDs, which can be populated even at low temperatures. Further, for thin shelled sample, an increase in temperature leads to a rapid drop in average lifetimes which would indicate thermally activated de-trapping from the trap states. Interestingly, the average lifetimes for the thick-shelled sample just keeps growing in a monotonic fashion with temperature, contrary to the drop for thin shelled samples. This would strongly suggest an energetically deeper trap distribution relative to the exciton energy. For such a trap distribution, ΔG would be negative and it would be easier for charges to get trapped but relatively difficult for them to get de-trapped. Also, with increase in temperature, the trap state population would grow due to increased trapping rates therefore reducing the number of exciton states available for radiative recombination.

We then proceed to develop a kinetic scheme based on Marcus theory, as discussed in section 3.2.5, to model exciton dynamics, and explain the origin of processes that might be responsible for long PL lifetimes, and the intriguing trend we observe for average lifetimes as a function of shell-thickness. The solid black lines in Figure 3.8 are computed from our kinetic models and match the experimental lifetimes very well.

The lowest energy exciton manifold in CdSe QDs (wurtize structure) is eight fold degenerate,[22] however, the exciton quickly relaxes back to the lowest state with sub-picosecond rates,[80] and therefore only the band-edge exciton states are sufficient for modeling exciton dynamics. Figure 3.9 shows the kinetic scheme used to model the exciton dynamics for the thin shelled QDs.

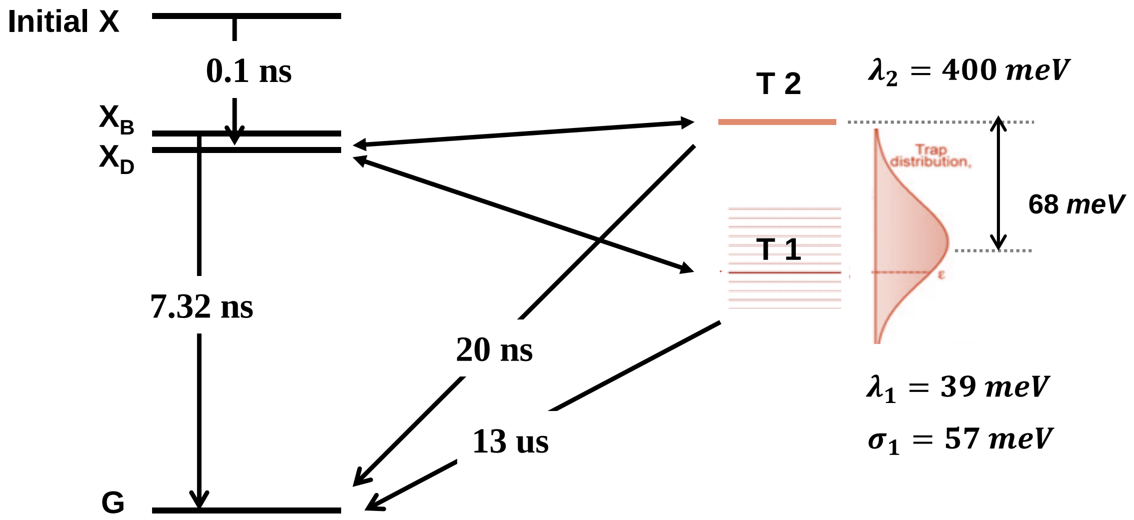

Figure 3.9 : Kinetic scheme based on Marcus electron transfer for thin shelled QDs. The corresponding transition times are indicated by solid black lines. $\boldsymbol{\lambda}$ denotes the reorganization energy as defined by equation 3.3 and $\boldsymbol{\sigma}$ defines the width of the Gaussian trap distribution as described by equation 3.2.

The kinetic scheme shown in Figure 3.9 consists of following states: ground state (G), high energy exciton (X) denoting initial photo-absorption high up in the band, bright (X_B) and dark (X_D) exciton states, and a series of discrete trap states (T1 and T2). It is to be noted that the kinetic scheme is framed in terms of electronic state representation, and not particle representation. Therefore, we don't assign trap distribution to any particular particle, and the model is equally valid for both electron or hole trapping. The interaction between exciton states and traps is modeled by Marcus electron–transfer theory. The transition from high energy, X to lower exciton states is denoted by a fast 1 ps rate that was held constant as changing this rate had a minimal effect on dynamics. Further, the non-radiative transition from trap states directly to ground state is very unlikely, and therefore this transition has a very slow rate of 13 µs, and changing this rate didn't have any significant influence on modeled dynamics.

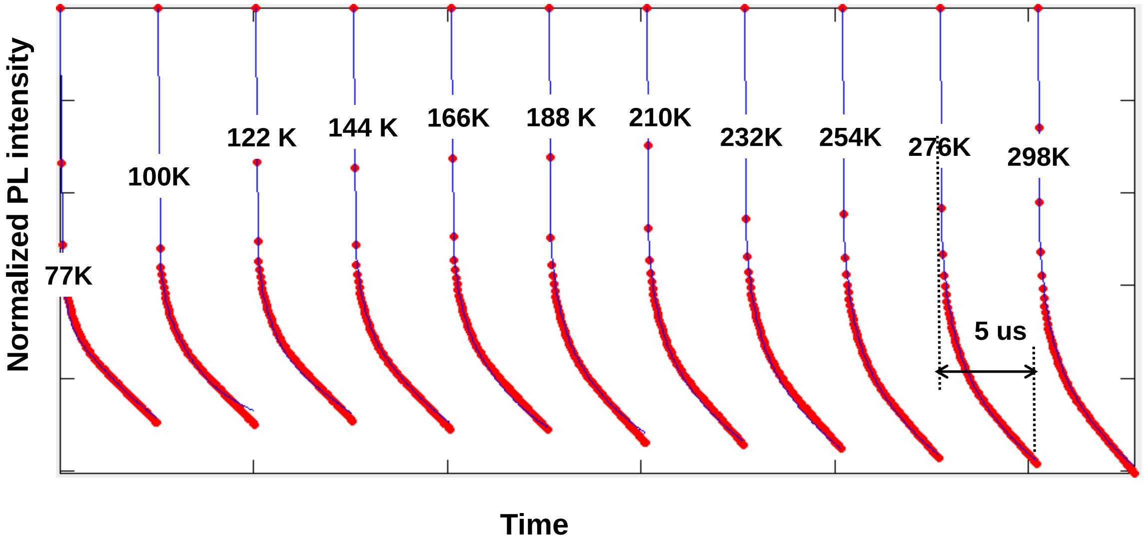

Figure 3.10: Global data analysis of 11 PL decay functions (red lines) using the kinetic scheme (blue thin lines) for thin shell QDs.

The kinetic model was then used to perform a global analysis of each pair of short and long decays for all the 11 different temperature datasets simultaneously.[41] In total, we have used a single kinetic model to globally fit data analyzed from 22 different decays, as shown in Figure. 3.10, over a long dynamic range of 5μs thus signifying the strength of our model. The full set of scheme parameters and associated errors are included in Appendix A.

We found that for thin shell QDs, the kinetic scheme required minimum two trap distributions, T1 and T2 to model the temperature resolved PL decays (see Figure 3.9). The two trap distributions are quite distinct: T1 is relatively broad (57 meV) and has a small reorganization energy (39 meV) whereas T2 is a narrow trap distribution with very large reorganization energy of around 400 meV. Large re-organization energies are often associated with electron or hole traps on the QD surface.[62,79] Since, for a thin shell QD, it is easier for the exciton to interact with surface traps therefore we believe that T2 most likely is a surface trap distribution. Further, T2 lies very close to the exciton energy level (just 7 meV above), and most likely responsible for the fast depopulation of exciton state leading to large average lifetimes observed at low temperatures.

It should be highlighted here that the number of trap states or trap distributions used in these kinetic models only represents the minimum required for an acceptable fit (criteria for a reasonable fit defined earlier). We did a thorough search of the parameter space but we couldn’t find other alternate solutions that could model the data well. Further, global modelling of large number of datasets using a relatively simple kinetic scheme, based on known photo-physical processes adds to the confidence in the kinetic modellings presented here.

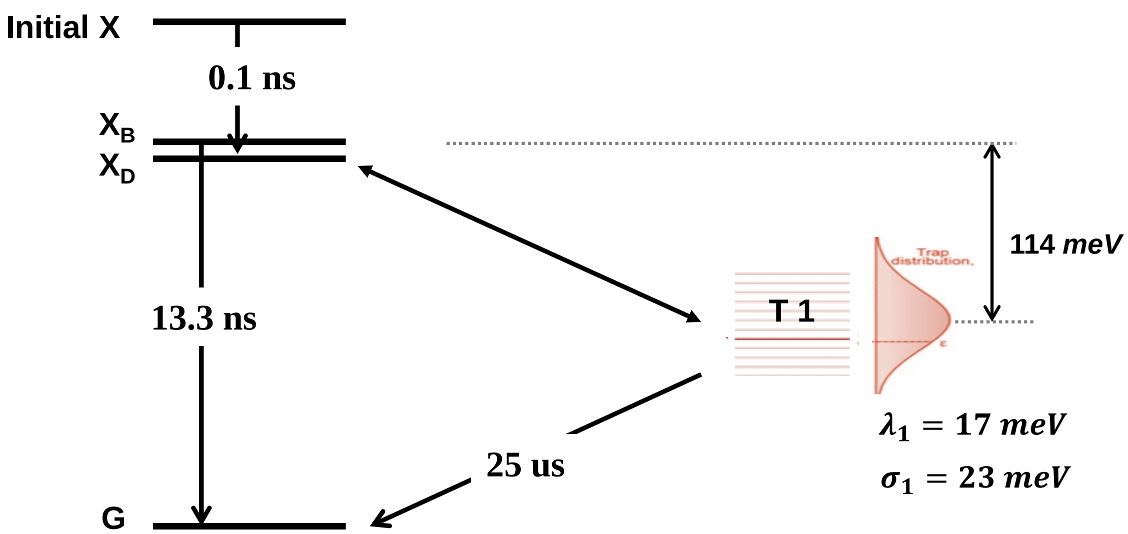

Figure 3.11: Kinetic scheme based on Marcus electron transfer for thick shelled QDs.

We built a similar kinetic scheme (Figure 3.11) to model the exciton trapping for the thick shelled QDs that consisted of a ground state (G), high energy exciton (X) denoting initial photo-absorption high up in the band, bright (X_B) and dark (X_D) exciton states, and a single trap distribution (T1). The fast relaxation from high energy X to low energy exciton state was fixed at 1 ps as in the previous case, and non-radiative rate from T2 directly ground state was negligible (25 µs). The radiative recombination was found to be slightly longer (~13 ns) than thin shelled dots (7 ns). The complete parameter set with standard deviations is included in Appendix A.

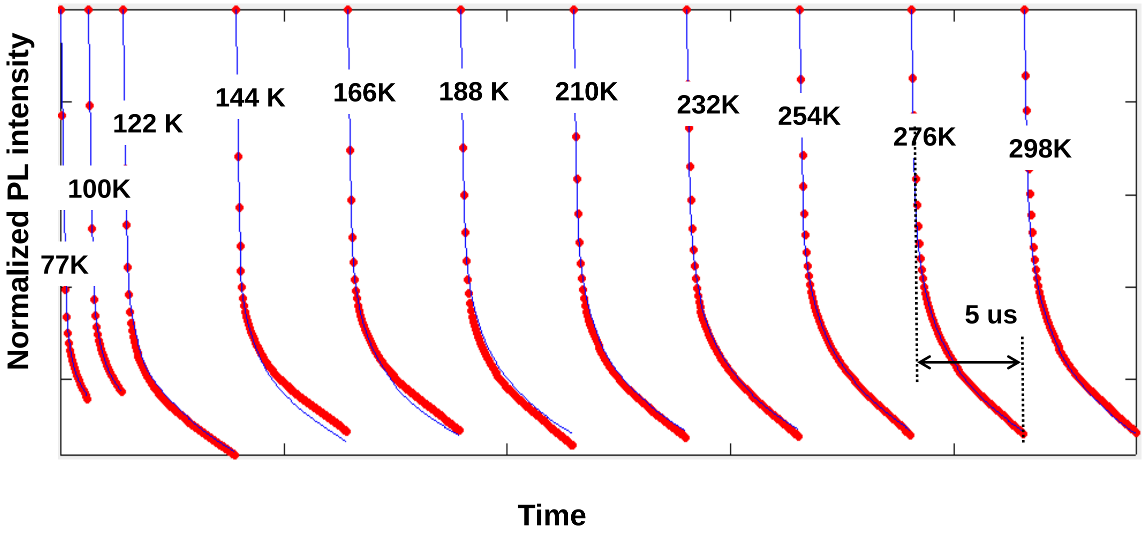

Figure 3.12: Global data analysis of 11 PL decay functions (red lines) using the kinetic scheme (blue thin lines) for thick shelled QDs.

However, interestingly, for thick shelled QDs, only one trap distribution (T1) was sufficient to model all the 11 PL decays (see Figure 3.12). T1 was found to be a relatively narrow distribution (FWHM around ~23 meV) and a small reorganization energy (17 meV), but lying very deep, roughly 114 meV below the exciton energy. Previous studies[62] have shown that trap states lying at the core-shell interface may have small re-organization energies similar to what we observe for T1 used for thin shelled QDs. Such kind of a trap distribution in thick shelled QDs would make sense since the exciton is further separated from the surface and is therefore less likely to interact with surface trap sites. Further, it might seem confusing how excitons trapped ~ 100 meV below would contribute to PL dynamics since it’s thermally unlikely for these excitons to get de-trapped, and recombine radiatively. Therefore, it should be stressed that only thermally accessible trap states contribute primarily to exciton dynamics, and not all traps in QDs would necessarily modify dynamics. A better way would have been to plot evolution of trap populations as a function of temperature but this beyond the scope this thesis.

Further, the depth of T1 relative to exciton energy is also consistent with increase in average lifetimes with temperature (Figure 3.9). Trap states below the exciton energy level will have $\Delta G < 0$, that would make it favorable for excited charge carriers to get trapped. Increase in temperature will further increase the trapping rates leading to higher trap population. Consequently, it would result in less number of available exciton states for radiative recombination leading to longer lifetimes.

3.4 Conclusions

We showed that shell thickness has a significant effect on exciton recombination dynamics in core-shell NCs. On the basis of kinetic modeling of PL dynamics, we found that thin-shelled QDs probably have two different type of trap distributions. One of the trap distributions had a high re-organization energy, and is most likely due to surface states. For thick-shelled QDs, a single trap distribution with a small reorganization energy was sufficient to model decay dynamics. These observations support the hypothesis that using a suitably thick conformal shell of a lattice matched semiconductor, we can minimize the quenching of CdSe core exciton by surface trap states.

CHAPTER 4 : VARIABLE PULSE RATE FLUORESCENCE SPECTROSCOPY

4.1 Motivation

Colloidal quantum dots show a very large range of fluorescence decay dynamics lasting from several picoseconds to few microseconds. In the previous chapter, we showed that CdSe/CdS QD samples had very long PL decay tails extending beyond 5 µs after the initial excitation. For a pulsed excitation source, in order to measure complete sample dynamics, the repetition rate or the signal period has to be kept long enough to cover full range of decay dynamics. However, as shown in Figure 4.1, for higher pulse repetition rates, QDs don't decay completely in the signal period. And, the next laser pulse may see an excited QD instead of a QD in the ground state and can re-excite it. And, as we increase the pulse repletion rate, we also increase the overall probability of re-exciting the sample, and therefore change the nature of accessible excited states. As discussed in chapter 1, increased understanding of multi-excited states in QDs is key to harness the full potential of semiconductor nanocrystal as the next generation opto-electronic material. Therefore, it is necessary to develop experiments and techniques that can help us to better understand the photophysics of multi-excited states.

The flexibility of our laser table allows us to easily change the repetition rate of excitation laser pulses, over a wide range, from 80 MHz to few Hz. In this experiment, we have used the CdSe/CdS (thick-shelled) QD samples as described in the previous chapter. Further, in the previous experiment, we have showed that the excited QDs relax back to the ground state within the 10 µs time window therefore setting the lower limit (1/10 µs) on the pulse rate that is required to re-excite the samples. The upper limit on pulse rate is determined by the repetition rate of laser source that in our case was 80 MHz, thus, the pulse rate was varied from 80 kHz to 80 MHz to induce and study the dynamics of multi-excited states in QDs.

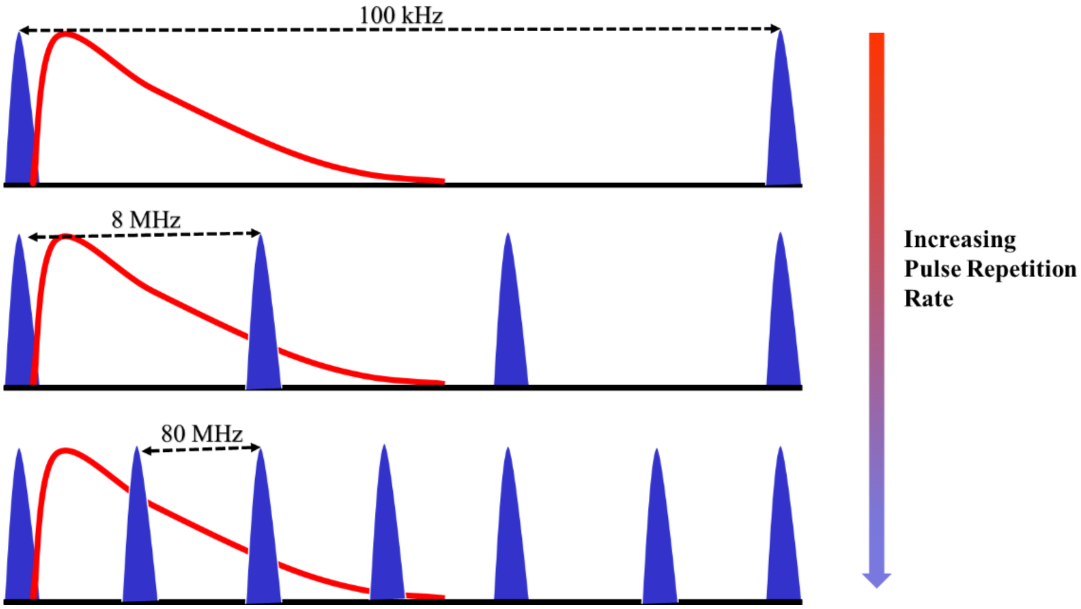

Figure 4.1: A cartoon illustrating the variable pulse-rate fluoresence technique.

4.2 Experimental methods

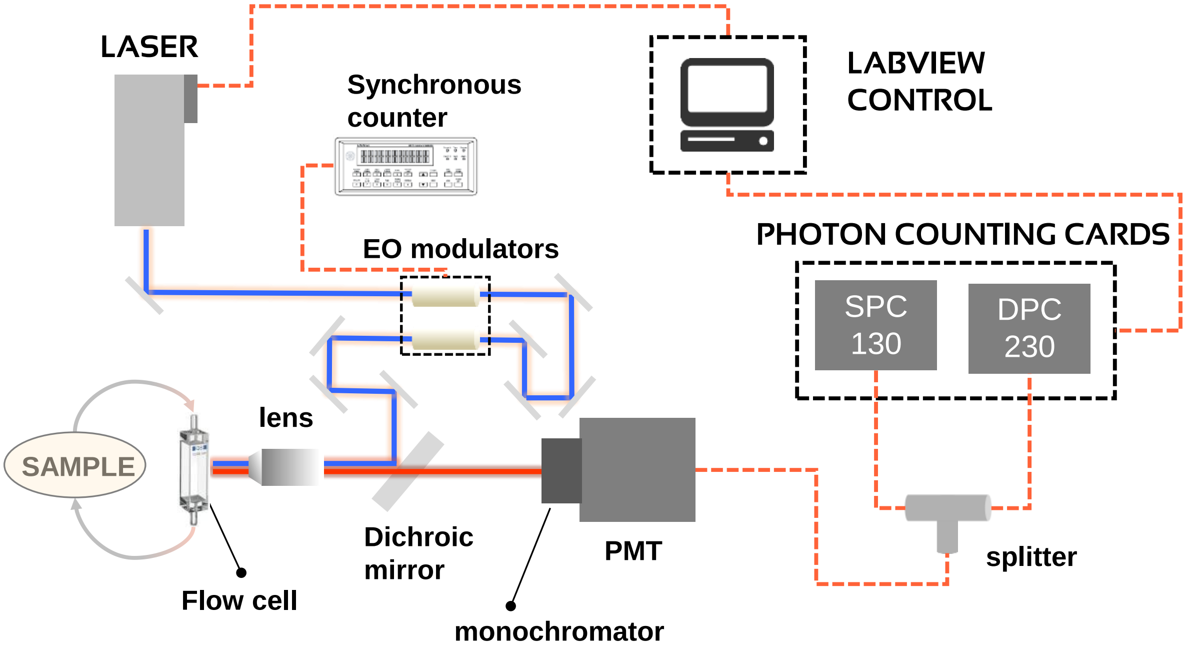

Figure 4.2: A simplified schematic of the variable pulse rate fluorescence experiment.

Femtosecond laser system (Ti:Sapphire /OPO), operating at 410 nm, as described in the previous chapter, was also used for this study. The frequency-doubled output (410 nm) from the OPO was then directed through two electro-optic modulators driven by a high voltage push-pull power amplifier (Conoptics 25D). The power amplifier in turn is triggered by a synchronous counting system (Conoptics 305). The synchronous counter allows us to change the pulse repetition rate anywhere from 40 MHz up to 10 Hz. For data collected at 80 MHz, the laser pulse train wasn't routed through the modulators, and directly hit the sample. It is to be noted that the synchronous counter has to be operated manually, and therefore cannot be controlled through a LabVIEW control scheme, as done for the previous project. However, we will describe a way to overcome this problem by outlining a more versatile scheme in the next chapter, which will also form the basis for a novel fluorescence technique.

For this project, we re-used the thick CdSe-CdS (9.25 monolayers) core-shell QD samples dispersed in hexane as described in chapter 3. The sample solution was placed in a flow cell cuvette connected to a peristaltic pump (Thermo scientific FH 10). The sample fluorescence was separated from the scattered laser light using a dichroic beam splitter and collected using a double monochromator, and a hybrid PMT. The PL was time resolved by time-correlated single-photon counting technique, as described previously, over a time window of 100 ns using the SPC-130 photon counting card.

4.3 Results and Discussion

4.3.1 Effect of excitation power

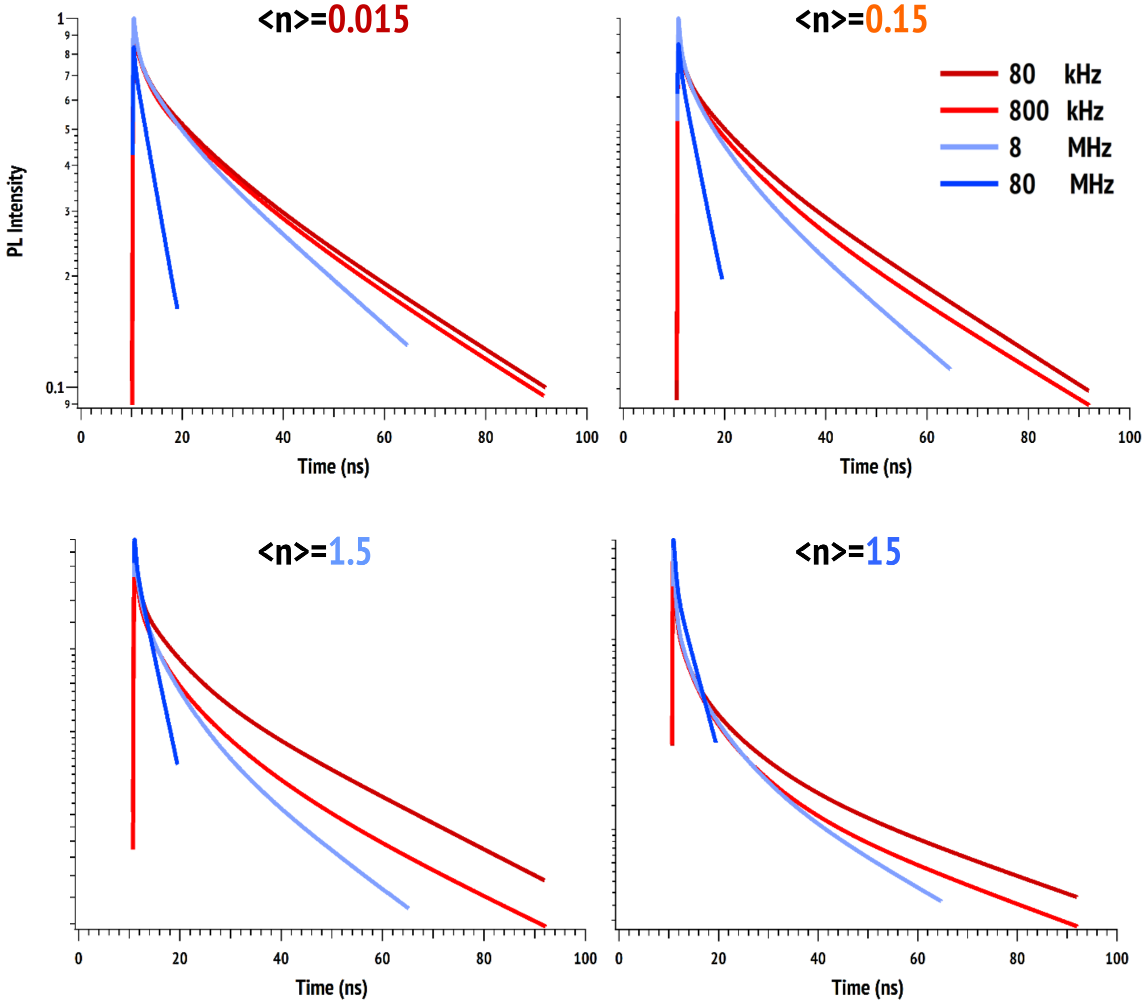

Figure 4.3: Fitted PL decays plotted as a function of pulse repetition rate for different excitation powers.

Figure 4.3 shows a set of QD fluorescence decays collected at four different excitation repetition rates: 80 kHz, 800 kHz, 8 MHz and 80 MHz. At each repetition rate, the PL decay is also collected as a function of excitation intensity.

The excitation intensity is quantified in terms of average number of photo-excitations per laser pulse, denoted $\langle n \rangle$. The magnitude of $\langle n \rangle$ can also be interpreted as the upper limit on average number of electron-hole pairs that can be generated per QD in each laser pulse, and is calculated by the following equation:

$$\langle n \rangle = \frac{C_{\text{abs}} \times \text{power}}{\text{photon energy} \times \text{spotsize} \times \text{laser repitition rate}} \tag{4.1}$$

where C_{abs} is the estimated absorption cross-section for the quantum dots. The details for this calculation are presented in Appendix A.

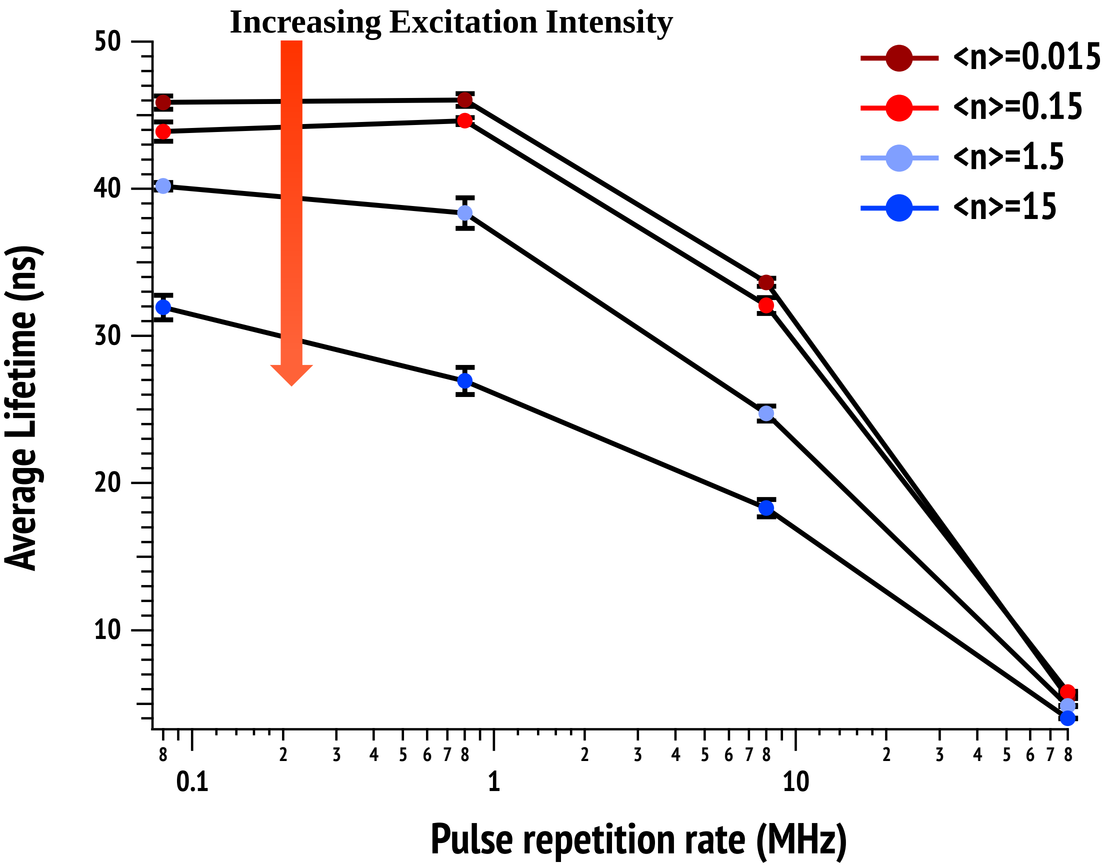

Figure 4.4: Average lifetimes plotted as a function of pulse repetition rate for different excitation powers. In each case, the error bars are ±2 × the standard deviation. The procedure for estimating errors is discussed in Appendix A.

We show in Figure 4.3 that even at low excitation intensities, $\langle n \rangle = 0.015$, increase in pulse repetition rates from 80 kHz to 80 MHz leads to a substantial change in decay dynamics. For low excitation intensity, the probability of creating more than one electron-hole pairs is negligible therefore the photoluminescence decay should just reflect exciton recombination dynamics. As we discussed in chapter 3, the exciton recombination times for QDs can be several microseconds due to exciton trapping and de-trapping by surface trap states lying close to the band edge. Therefore, if either one of the photo-excited hole or electron is trapped, the QD core becomes charged, and if the charge separated state lives long enough it can be photo-excited several times by the faster repetition rate pulses. And we know from QD photo-physics, particularly blinking[65,81,82] and spectral diffusion[83] experiments that QD discharging time can be microseconds or longer. Further, the charged QDs can absorb another photon (from the next pulse in the pulse train) to form a trion[84] that have fast emission rates.

Moreover, we can analyze the decay dynamics by calculating average lifetimes using eq. 3.1 as described in the previous chapter.

As shown in Figure 4.4, for low excitation intensities, $\langle n \rangle = 0.015$ and 0.15, the average lifetimes do not change appreciably for pulse repetition rates up to 800 kHz but changes considerably at 8 MHz repetition rate. This means that the charge separated state in QD lives on the scale of several hundreds of nanoseconds somewhere between 125 ns and 1.25 µs. At maximum pulse repetition rate of 80 MHz, the average lifetime becomes really short around 4 ns. This is partially because the average lifetime can be calculated only for a small time window of ~10 ns (at 80 MHz, the time separation between pulses is 12.5 ns), thus would be preferentially biased towards faster PL decay components.

However, as shown in Figure 4.3, even over a 10 ns time window, the PL decays much faster at 80 MHz. This would strongly indicate that at higher repetition rates, we start creating new photo-species, such as biexciton or trions as discussed earlier that have shorter emission times.

At moderate and high excitation intensities, namely $\langle n \rangle = 1.5$ and 15, we start creating multiple electron-hole pairs such as bi-excitons and tri-excitons that have short emission lifetimes; leading to faster decaying PL even at low repetition rates.

4.3.2 Effect of sample flow rate

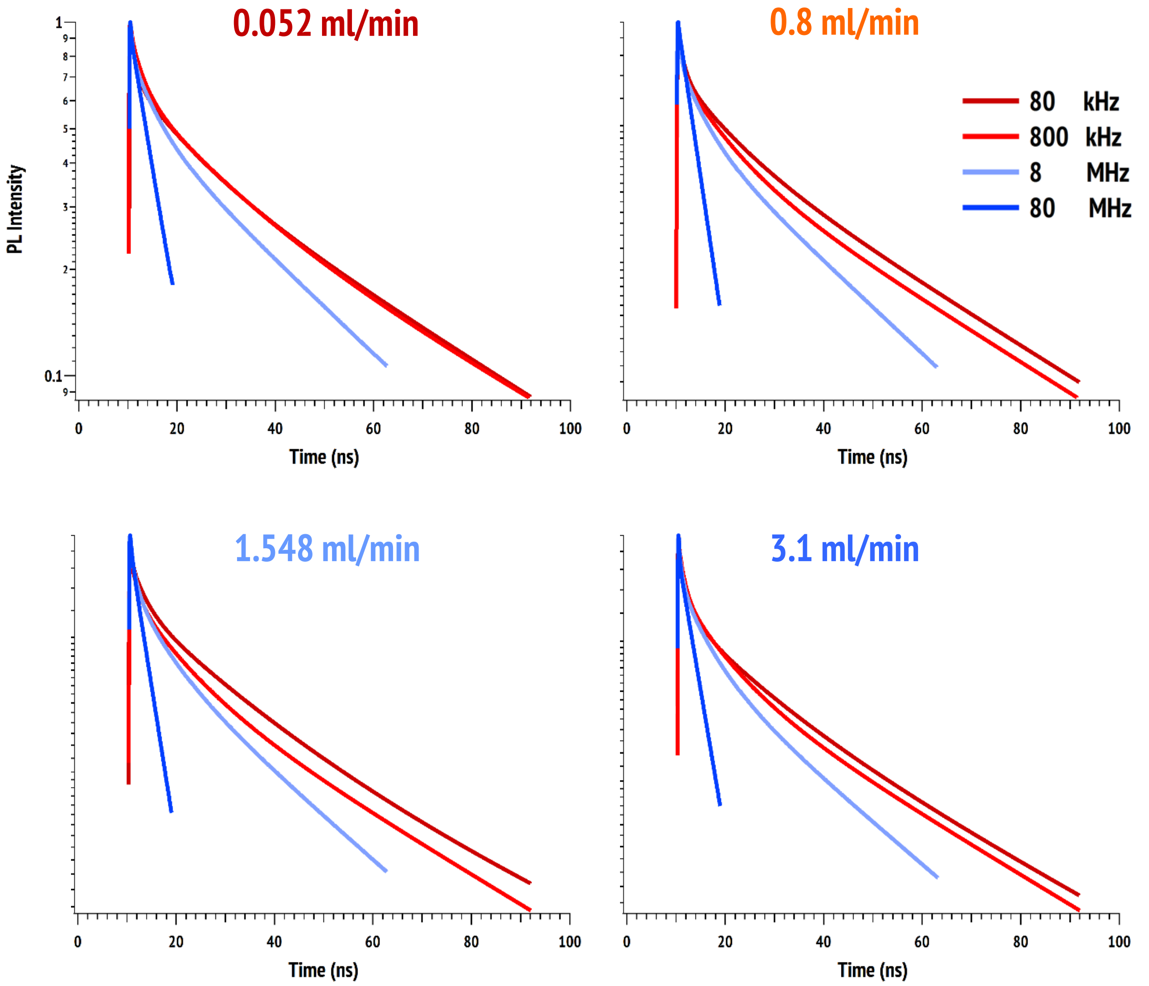

Figure 4.5: Fitted PL decays plotted as a function of pulse repetition rates for different sample flow rates.

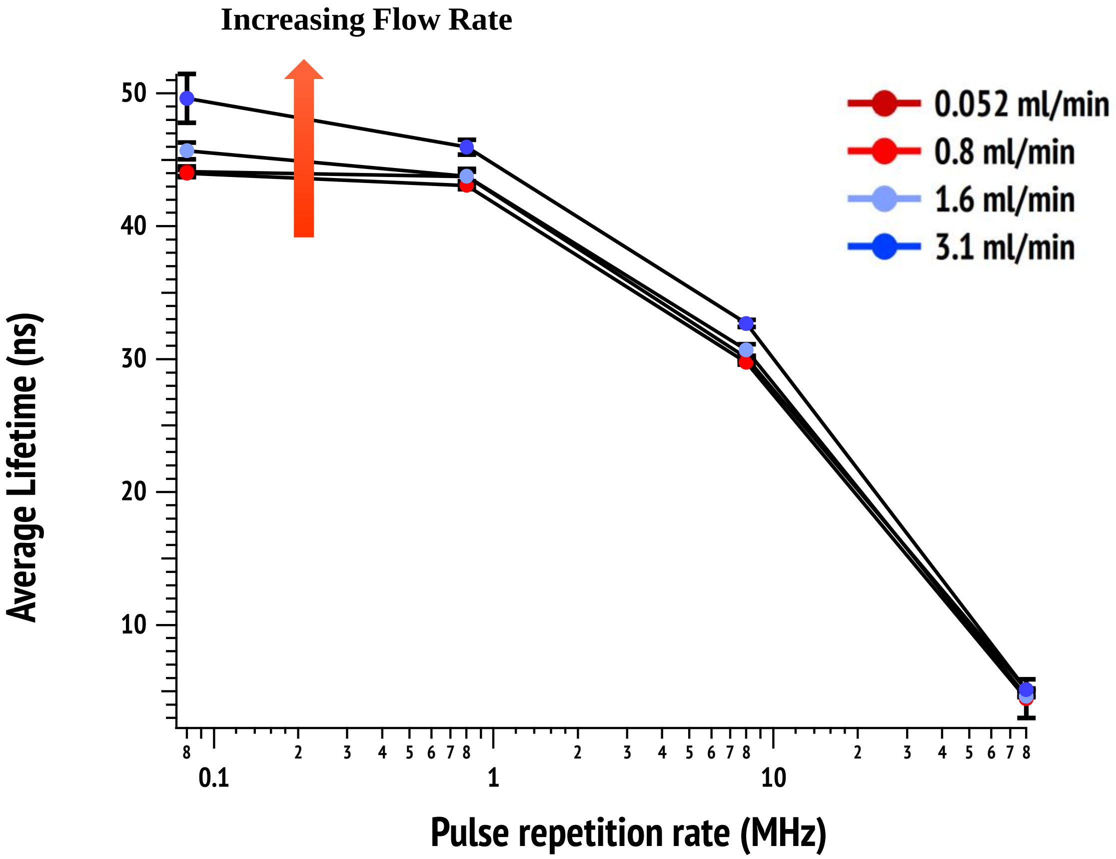

Figure 4.6: Average lifetimes plotted as a function of pulse repetition rate for different sample flow rates. In each case, the error bars are ±2 × the standard deviation.

The fast decaying components in PL emission in QDs, especially at higher photo-intensities or excitation rates, have been a source of confusion,[45] and make its very difficult to distinguish the nature of emitting state whether it is an exciton, bi-exciton or an emissive trion.

If the excited state created in our variable pulse rate experiment is an emissive trion based on a population of long lived charged QDs, then flushing the sample periodically using a flow cell should reduce the population of charged QDs in the excitation volume, resulting in modified emission dynamics. Therefore, we did another experiment at low excitation intensity ($\langle n \rangle = 0.15$) but with QDs (dispersed in hexane) placed in a flow cell. QD sample flow rates were varied over three orders of magnitude, and for each flow rate, fluorescence decays were collected at four different excitation repetition rates: 80 kHz, 800 kHz, 8 MHz and 80 MHz. Flow cell allows us to replace QDs in the excitation volume with fresh supply of unexcited QDs. If the rate of replenishment of QDs is comparable to the rate of generation of photo-charged QD population in the excitation volume, this should manifest in terms of modified fluorescence dynamics as a function of pulse repetition rate, and sample flow rate. Figure 4.5 shows the QD fluorescence decays collected for different sample flow rates, and at varied pulse repetition rates.

For low repetition rates, 80 kHz and 800 kHz, raising the flow rate lead to increased average lifetimes (Figure 4.6). This is anticipated since an increase in the sample flow rate would result in quicker flushing out of faster decaying charged QD population in the excitation volume. At the maximum sample flow rate of 3.1 ml/min, its takes around ~10 µs (or 1/100 kHz) for replenishing the excitation volume of $0.469 \times 10^{-6}\,\mathrm{cm}^3$ (see Appendix A) in our experiment. Thus, the average lifetime would be weighed more by the uncharged QDs having relatively longer lifetimes. At higher repetition rates, namely 8 MHz and 80 MHz, increasing flow rates doesn't appreciably change the average PL lifetimes. This is expected because the rate of charged QD population buildup by high repetition rate pulses is much higher than that can be replenished by an increase in flow rate.

4.4 Conclusions

In this project, we have introduced variable pulse rate fluorescence spectroscopy as a niche technique to study multi-excited state fluorescence in QDs. We found that pulse rates faster than 800 kHz resulted in a change in PL dynamics even at low excitation powers implying that QDs were re-excited and these multi-excited QDs had modified dynamics. Now, we know that excitons recombine fairly quickly (few ten of ns) therefore these re-excited QDs cannot be bi-excitons, and therefore strongly suggestive of charged separated states that can last very long from several hundred nanoseconds to at least a microsecond. We then flowed the sample at different flow rates to show that by changing the QD flow rates, we can control the build of these charge separated states. This is particularly very useful when we want to analyze multi-exciton fluorescence and thus would like to avoid the buildup of faster decaying charged QD states that have lifetimes similar to multi-exciton recombination times.

However, recording fluorescence decays at variable pulse rates has several severe limitations. First, we are unable to record a baseline during measurement, required for data-fitting, particularly at high repetition rates. This is anticipated because, excitation source being a continuous series of pulses, would lead to pile up of emission decays from previous pulses. Second, time window available to record decays becomes limited especially at high repetition rates (for e.g. just 12.5 ns window for an 80 MHz pulse laser). Since time window at high repetition rates is much shorter than the emission time of the QDs it is therefore difficult to distinguish slower decay processes that are the key to understanding the exciton dynamics that we discussed in the previous chapter. This prompted us to look for a more controllable technique, and resulted in the development of multi-pulse time-resolved fluorescence spectroscopy that we discuss in the next chapter.

CHAPTER 5 : MULTI-PULSE TIME RESOLVED FLUORESCENCE SPECTROSCOPY[⊥]

5.1 Motivation

In a typical time resolved fluorescence experiment, increasing excitation intensity is the most common way of generating multi-excited states. However, the fluorescent yield of multi-excited states in colloidal QDs, such as biexcitons or trions, is often small and their lifetimes can be comparable to fast decay components in multi-exponential exciton decays.[45] It is therefore very difficult to distinguish multi- from singly-excited states using conventional time-resolved fluorescence techniques. The alternative approach is to increase the pulse rate of the excitation laser which has several limitations as discussed in the previous chapter.

To overcome this issue we have taken a slightly different approach. Instead of illuminating our QDs with variable repetition rate pulses, we have developed a gated time-correlated single photon counting experiment that excites the sample with a controllable number of 80 MHz laser pulses. Figure 5.1 outlines the multi-pulse technique we introduce in this chapter. By controlling the individual pulse energy and varying the number of pulses in the pulse train, our technique allows us to controllably create and study the photo-physics of multi-excited states in colloidal QDs. Also, our technique enables us to measure both long and short lived multi-excited states, and we will show later that the long time window provided by our gated technique allows us to distinguish between neutral and charged

---

[⊥] Some sections in this chapter are adapted from my published work: Multipulse Time-Resolved Fluorescence Method for Probing Second-Order Recombination Dynamics in Colloidal Quantum Dots. *J. Phys. Chem. C* 118**,** 14692–14702 (2014

QDs, and can potentially help us design better ways of utilizing multiexcitons in new devices.

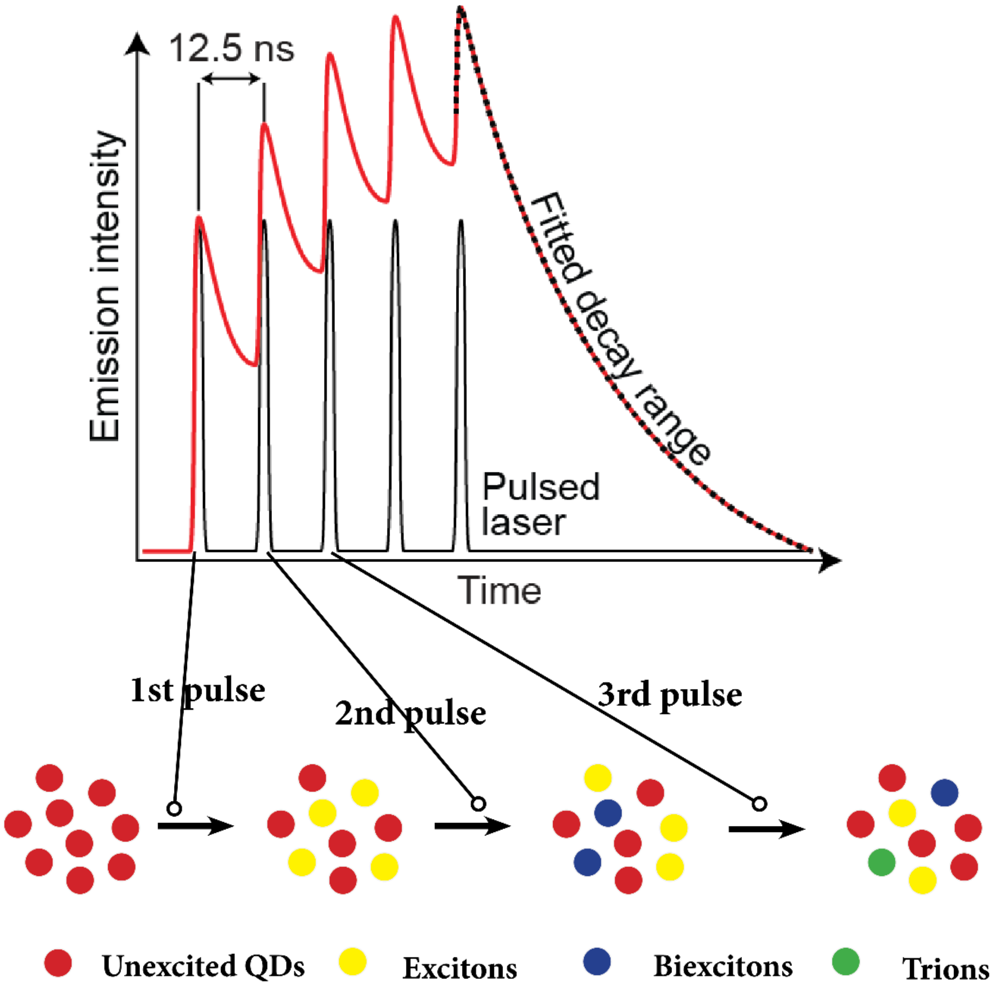

Figure 5.1: A schematic showing multi-pulse single photon counting technique. The QDs are excited multiple times during the pulse sequence that leads to creation of multi-excited states such as biexcitons, trions etc. These higher order species have different recombination dynamics that are reflected in the N^{th} pulse decay.

5.2 Experimental methods

5.2.1 Sample preparation

The thick shelled (9.25 monolayers) CdSe-CdS QDs, as described in chapter 3, were also utilized in this experiment. The nanocrystals were purified by precipitation with methanol, and then re-dispersed in hexane. In addition, before collecting time resolved data, the QD sample was degassed by several freeze−pump−thaw cycles to remove dissolved oxygen. A degassed test sample was initially prepared, and fluorescence intensity and decay profiles were monitored for 24 hours under continuous photo-excitation to ensure that the sample is photo-stable and prolonged excitation exposure for several hours (as in this experiment) does not photo-bleach the QDs.

5.2.2 Multi-pulse fluorescence setup

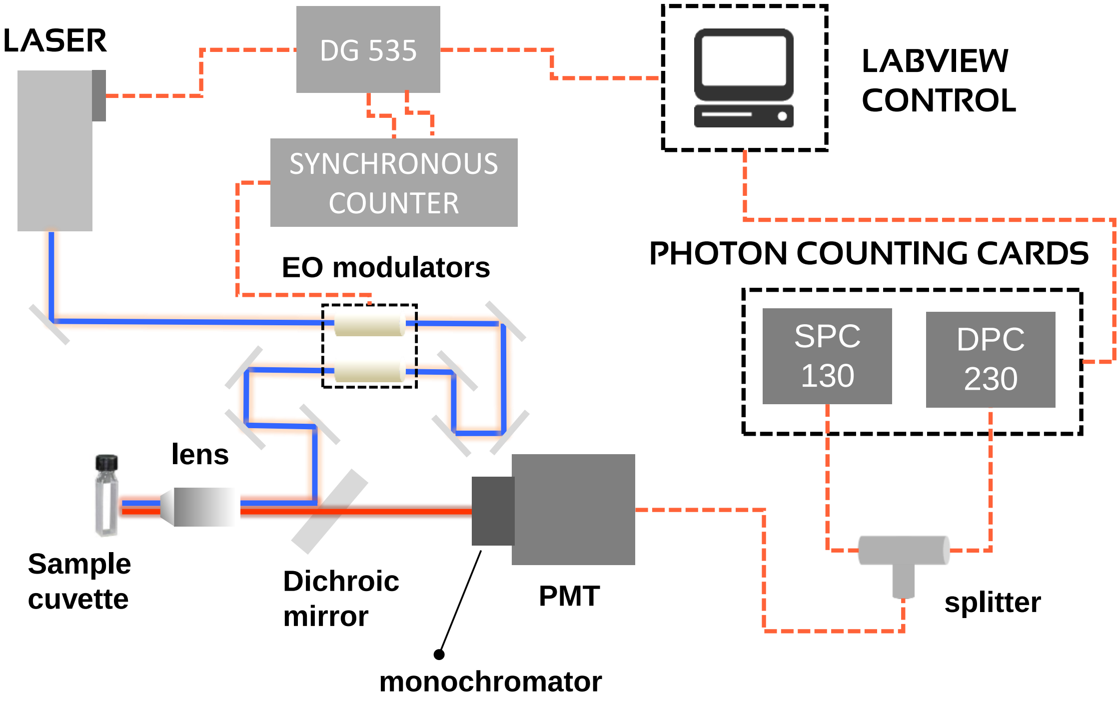

Figure 5.2: A simplified schematic of the multi-pulse experimental setup.

The optical laser table used for this experiment was very similar to one described in the previous chapter in terms of excitation light used, layout of optical components, and photon counting scheme. Figure 5.2 shows the basic experimental apparatus that was used for this project. The doubled light at 410 nm (3.02 eV) from the femtosecond laser system (Ti:Sapphire/OPO) was used to photo-excite the samples. The QD fluorescence was separated from the scattered laser light using a dichroic beam splitter and collected using a double monochromator, and a hybrid PMT. The PL was time resolved TCSPC technique, as described previously, using SPC-130 (short time window) and DPC-230 (long time window) counting modules.

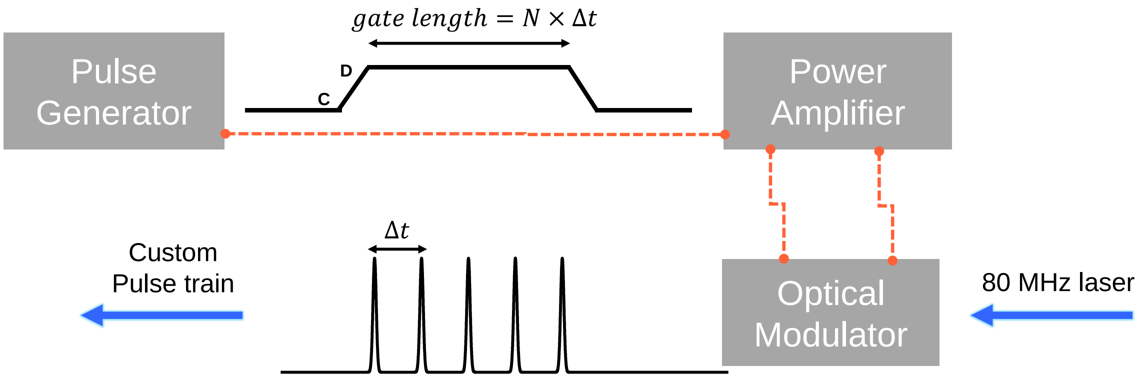

Figure 5.3: Schematic showing the generation of multi-pulse waveform with a desired number of pulses, *N*, from an 80 MHz pulse train.

In order to generate a customized pulse train for doing multi-pulse time resolved fluorescence, we had to change the way we modulated the laser pulses. Figure 5.3 outlines the basic approach we have employed to generate multi-pulse waveforms.

We configured a pulse generator (SRS DG535) to produce an electronic gate of variable length. The length of the gate signal, that was a standard TTL logic, was determined by the number of pulses we required in the pulse-sequence. Further, the pulse generator was triggered by the synchronous counter at 100 kHz (only for this study but could be adjusted accordingly from DC to 1 MHz). This means that two consecutive pulse sequences consisting of N pulses were separated by 10 μs.

The gate signal was then sent to the high voltage push-pull power amplifier that drives the electro-optical modulators. The high voltage driver was fully DC coupled and can accept any pulse width. Thus, the width of the electronic gate determined the length of the optical gate opened by the electro-optical modulators. Varying the length of the electronic gate controlled the number of pulses in the sequence. Further, the optical "gate" created by the driver/modulator system had to be synched with the incoming laser pulse train. This was achieved by adding an adjustable delay to the gate signal using one of the delay channels on the pulse generator.

5.2.3 Multi-pulse fluorescence technique

In a fluorescence experiment, the measured fluorescence intensity, $I(t)$, is a convolution of actual fluorescence decay function, $F(t)$, and excitation function, $E(t)$. This could be mathematically expressed as:

$$I(t) = \int_0^\infty F(t - t')\, E(t)\, dt' \tag{5.1}$$

In order to simplify matters, let's assume that each ultrafast laser pulse is a Dirac-delta function. Then, for a multi-pulse experiment, the excitation function can be simply treated as a sum of Dirac-delta functions:

$$E(t) = \sum_{j=0}^{N-1} \delta(t + j\Delta t) \tag{5.2}$$

where N is the number of pulses in a pulse sequence, and Δt is the time-separation between pulses. Therefore equation 5.1 can be rewritten as:

$$I(t) = \int_0^\infty F(t - t') \sum_{j=0}^{N-1} \delta(t + j\Delta t)\ dt' \tag{5.3}$$

Case I: Average PL lifetime $\ll\ \Delta t$

If the sample decays completely within the inter-pulse period, Δt, then the experiment would reduce to a standard photon counting experiment in which we build a photon histogram at a certain repetition rate.

Case II: PL decay $> \Delta t$ and $F(t)$ is invariant

Almost all QD samples generally have decays that extend much beyond 12.5 ns, that is the inter-pulse time period of our system. We have shown in chapter 2 that QD decays can have long tails that can extend upto several microseconds on account of (de-)trapping processes, and this is one of the reasons why we record PL transients over long time windows as well.

However, if the sample decay function doesn't change with each pulse then equation 5.3 could be simplified as:

$$I(t) = \int_0^\infty F(t - t') \sum_{j=0}^{N-1} \delta(t + j\Delta t)\ dt'$$

$$I(t) = \sum_{j=0}^{N-1} \int_0^\infty F(t - t')\delta(t + j\Delta t)\ dt'$$

$$I(t) = \sum_{j=0}^{N-1} F((t + j\Delta t)) \tag{5.4}$$

Equation 5.4 essentially means that multi-pulse decay after N^{th} pulse can be expressed as sum of N independent single pulse decays, $F(t)$, each displaced in time by Δt.

We can verify this experimental condition in several different ways. One way is to photo-excite the sample at very low excitation powers such that the probability of re-exciting the same QD in a given pulse-sequence is negligible. We will discuss this regime later in this chapter.

Another approach is to synthesize QDs whose recombination dynamics don't change even if they are photo-excited multiple times in a pulse sequence. This approach is slightly challenging because it's difficult to synthesize well-passivated QDs, and when multiply excited may lead to formation of charged species that have modified recombination dynamics. However, we were able to obtain some very well passivated core-shell CdSe/CdS QDs from our collaborators at University of South Carolina, that have close to unity quantum-yields and nearly mono-exponential dynamics.[85] These nanocrystals showed exemplary photo-stability, and showed no change in recombination dynamics even when they were multiply excited. We did a multi-pulse experiment on a sample of these QDs, dispersed in a degassed solvent, using 10 different pulse sequences (containing 1, 3 5, 7, 9, 11, 15, 21, 25 and 29 pulses) over two different time windows of - 500 ns and 5 μs. And, we were able to fit all the multi-pulse decays using just the equation 5.4. Details of this data and associated fits are included in Appendix C. We will discuss the photo-physics of these particular QDs in much more detail in the next chapter.

Case III: PL decay $> \Delta t$ and $F(t)$ changes with multi-pulse excitation

This is the regime in which QDs in the excitation volume are excited more than once over the pulse-sequence. And, if these multiply excited QD states are emissive and have different recombination rates than the singly-excited QDs, then the N^{th} pulse decay shape can no longer be dictated by Equation 5.4, and has to be accounted for additional decay components introduced by formation of multi-excited states.

5.3 Results and discussion

5.3.1 Multi-pulse decays

A controllably gated 80 MHz pulse sequence consisting of 1 to 25 pulses was generated using electro-optic modulators. The length of time between the start of two consecutive pulse sequences was held at 10 μs to give sufficient time for excited QDs to return to the ground state. Each pulse photoexcites a proportion of the QDs and generates a fluorescence decay that is added to any fluorescence generated by the previous pulses in the sequence. Composite plots containing seven representative PL data sets are presented in Figure 5.4. These data were recorded using seven different pulse sequences (containing 1, 5, 9, 13, 17, 21, and 25 pulses) over a 500 ns and a 5 μs time window to ensure accurate determination of both short and long decay components. The final decay for each N-pulse pair (short and long time window) was simultaneously modeled with one multiexponential decay function convoluted with the measured 1-pulse instrument response function.

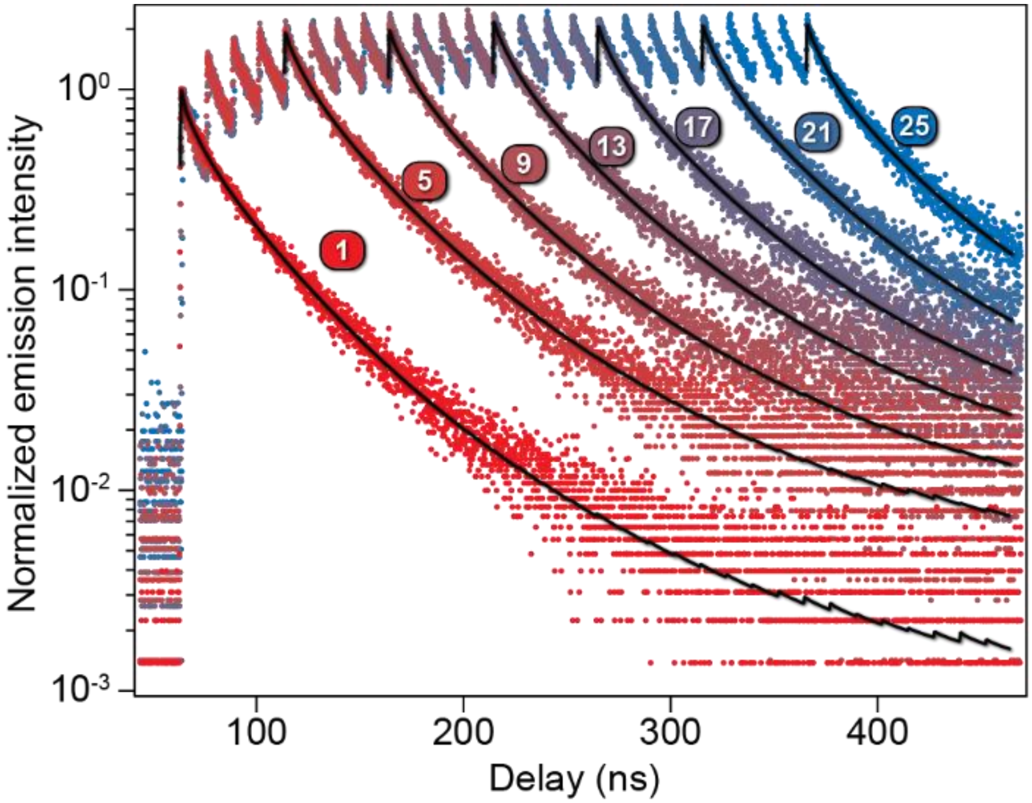
Normalized emission intensity
10^0
10^-1
10^-2
10^-3
100
200
300
400
Delay (ns)
1
5
9
13
17
21
25

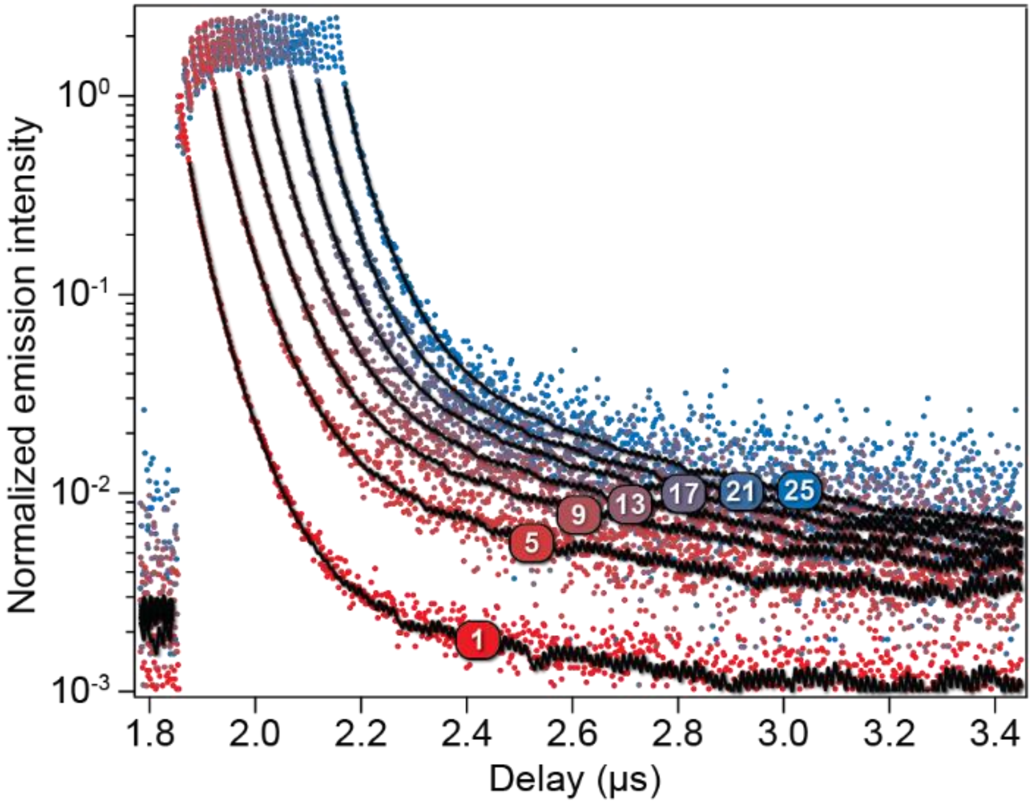
Normalized emission intensity
10^0
10^-1
10^-2
10^-3
1.8
2.0
2.2
2.4
2.6
2.8
3.0
3.2
3.4
Delay (µs)
1
5
9
13
17
21
25

Figure 5.4 Composite plots of multi-pulse time-resolved fluorescence data recorded using low excitation pulse energy (λ=0.002) over two different time windows: (a) 500 ns and (b) 5 µs. The number of laser pulses used to generate each of the decays is indicated.

Figure 5.4 shows that the peak intensities initially rise with *N*, reaching a quasi-equilibrium after approximately eight pulses (~100 ns). In other words, it takes about eight pulses for the exciton population lost to recombination to be balanced by the population generated in each pulse. In addition, the decay shape change slightly as a function of the number of laser pulses in the sequence, *N*. This is expected because each laser pulse in a sequence generates a decay that adds to and is offset from the previous decay.

A typical single pulse decay can be modeled by a multi-exponential function, $I_1(t)$

$$I_1(t) = \sum_i \alpha_i e^{-k_i t} \tag{5.5}$$

In the limit of low fluence, as discussed in section 5.2.3, the N^{th} pulse decay can be written using Equation 5.4 as:

$$I_N(t) = \sum_{j=1}^{N-1} I(t + j\Delta t)$$

$$I_N(t) = \sum_i \alpha_i e^{-k_i t} \sum_{j=0}^{N-1} e^{-jk_i\Delta t} = \sum_i \alpha_i \left(\frac{1 - e^{-Nk_i\Delta t}}{1 - e^{-k_i\Delta t}} \right) e^{-k_i t} \tag{5.6}$$

In general, if an *N*-pulse QD fluorescence decay can be modeled with eq. 5.6, using the α_i and k_i coefficients obtained after fitting a 1-pulse decay, it is a strong indication that the same distribution of excited states was formed after each pulse in the *N*-pulse experiment. Conversely, if eq. 5.6 does not model the N^{th} pulse decay when the α_i and k_i coefficients from a 1-pulse fit are used, it means that the second and subsequent laser pulses gave rise to a modified distribution of excited states with different fluorescence decay dynamics.

5.3.2 Experimental conditions

Using estimated absorption cross-sections we calculated the average number of photo-absorption events per illuminated QD per laser pulse, denoted by λ. Decay series were then recorded at three different laser powers corresponding to $\lambda=0.002$ (low power, LP), 0.15 (medium power, MP) and 1.5 (high power, HP). Each series was recorded with $N = 1, 5, 9, 13, 17, 21$, and 25 pulses. The final decay in each series was then independently modeled with multiexponential decay functions.

For estimating multiphoton absorption for N pulse experiments, we did a Poissonian analysis of excitation fluence, which is presented in the Appendix B. Assuming that photon absorption is a stochastic process, and that the QD absorption cross-section is unchanged for the absorption of a second, or subsequent photon, we calculated

(i) the probability that a QD will absorb one or more photons during the pulse train, but never more than one per pulse and

(ii) the probability that a QD will absorb two or more photons, and more than once per pulse on at least one occasion.

(a) *Low Power*

At low excitation power, the probability that QD is re-excited again over the entire pulse train is very low (0.0012), and therefore, there should be no contribution of multi-pulse dynamics and the N^{th} pulse decay should be simulated by eq. 5.6. We can clearly see in Figure 5.5a, that for low excitation power, the actual 25-pulse decay (green curve) indeed matches exactly with the simulated 25-pulse decay using eq. 5.6.

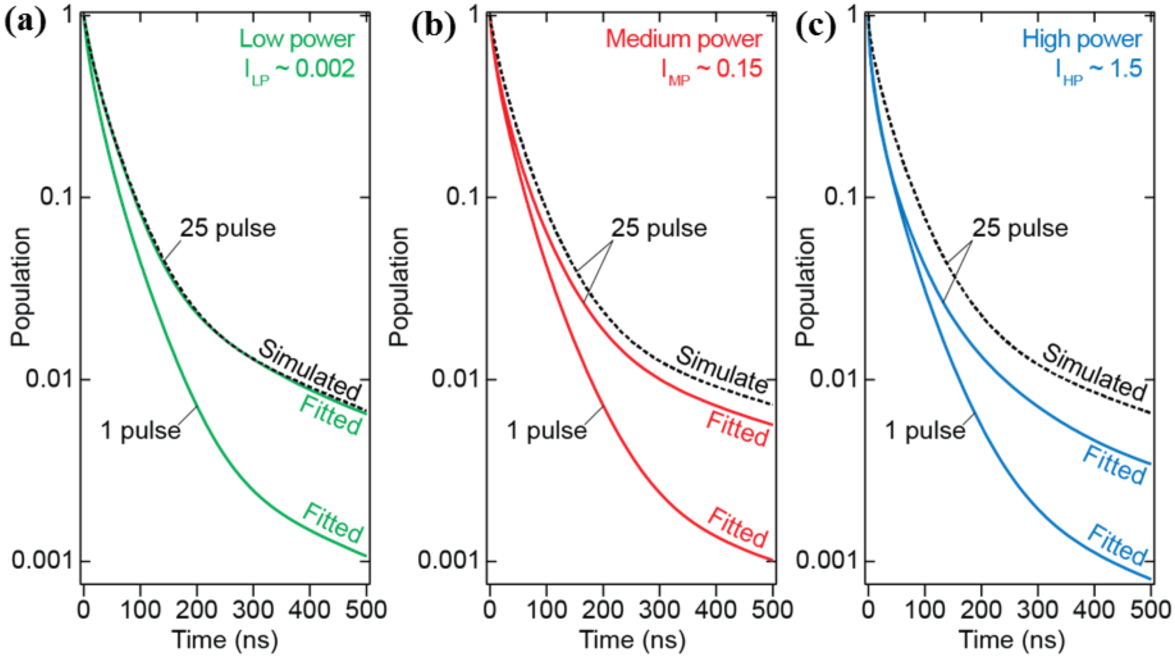

Figure 5.5: (a)-(c) Multiexponential decays extracted from fits to $N = 1$ ($I_1(t)$) and $N = 25$ ($I_{25}(t)$) TRPL decays recorded at (a) low (green curves), (b) medium (red curves), and (c) high (blue curves) power. In each case the black dashed line is generated from $I_1(t)$ using eq 5.6.

(b) *Medium* Power

The medium excitation power was chosen so that there is still a very small probability (0.01) of QD absorbing two or more photons in a single laser pulse but over the 25-pulse train, the likelihood that two or more photons are absorbed becomes high (0.89). This is the regime where we can make the distinction between multi-excited states formed by multiphoton absorption over multiple pulses vis-à-vis multiphoton absorption in a single high intensity pulse.

And, as expected, for medium power, the experimental 25-pulse decay (red curve, Figure 5.5b) diverges from the simulated decay curve. This means that we can no longer describe the N^{th} pulse decay simply as a sum of single pulse dynamics and that probably, the 2nd and subsequent laser pulses are giving rise to a modified distribution of excited states with different fluorescence decay dynamics.

(c) *High Power*

The high power level was chosen so that multiphoton absorption was very likely both for single pulse (0.44) and the entire 25-pulse train (1.00). And as would be expected, the divergence between the experimental 25-pulse decay (blue curve, Figure 5.5c) and the simulated decay was even higher.

This implies that if the pulse repetition rate in an *N*-pulse train is such that two or more pulses occur within the chromophore's excited state lifetime then, assuming sufficient laser fluence and measurable fluorescence intensity from multi-excited states, decays recorded with a different number of laser pulses cannot be fit using just one multi-exponential function. In this case, higher order decay terms contribute to the total *N*-pulse decay, $I_N(t) = \sum_{m=1}^{N} I_N^{(m)}(t)$. For example, second-order fluorescence can arise from QDs that have absorbed a photon from pulse i, generating an exciton, and then absorb a second photon from pulse j ($i \neq j$) within the exciton lifetime, generating a biexciton. In an *N*-pulse train, the contribution to the fluorescence dynamics from states generated in this way would be denoted as $I_N^{(2)}(t)$.

Given sufficient laser fluence, a QD could absorb two photons from a single laser pulse. Fluorescence emitted by the resulting doubly excited state would be second order with respect to the number of photons per pulse. However, emission contributions from states formed in this way would contribute to $I_N^{(1)}(t)$ since both absorptions occurred within the same pulse. Instead we are considering contributions that are second order with respect to the number of laser pulses. In this approach, fluorescence from doubly excited QDs formed after interaction with two *separate* laser pulses is second order and would therefore contribute to $I_N^{(2)}(t)$.

Since it takes at least m pulses to observe the contribution of the m^{th}-order term we can, in general, generate the $I_N^{(m)}(t)$ decay contribution from $I_m^{(m)}(t)$ using a slightly modified version of eq. 5.6,

$$I_N^{(m)}(t) = \sum_{j=0}^{N-m} I_m^{(m)}(t + j\Delta t) = \sum_i \alpha_i \left(\frac{1 - e^{-(N-m+1)k_i \Delta t}}{1 - e^{-k_i \Delta t}} \right) e^{-k_i t} \qquad (5.7)$$

where α_i and k_i are, respectively, the i^{th} pre-exponential coefficient and decay constant for the $I_m^{(m)}(t)$ decay.

We found that first- and second-order contributions were required to fit the measured decays. This was done by simultaneously modeling an entire pulse series ($N = 1, 5, 9, 13, 17, 21$ and25) using the fit function in eq. 5.7:

$$I_N(t) = \chi_N^{(1)} I_N^{(1)}(t) + \chi_N^{(2)} I_N^{(2)}(t) \qquad (5.8)$$

The relative weighting of first- and second-order contributions in each of the N-pulse decays was determined by the fitting parameters, $\chi_N^{(m)}$, which change with N. Since second-order contributions are absent from the 1-pulse experiments, $\chi_1^{(2)} = 0$.

In total, 14 decays (short and long time windows for each N) were globally fit for low, medium, and high power experiments. Note that seven exponentials were the minimum required to achieve an acceptable fit: reduced chi-squared, $\chi^2 < 1.1$, and Durbin–Watson parameter, $|d - 2| < 0.05$. All the decay functions are fully tabulated in the Appendix B.

High quality fits to the medium and high power decays required a second-order contribution, $I_N^{(2)}(t)$, to account for modified recombination dynamics with increasing N. $I_2^{(2)}(t)$ was found to be a single exponential decay function for the medium power fluorescence and a biexponential function for the high power data. Note that although we could not rule out the contribution of third-order dynamics, our decay analysis suggests that their contribution is likely $\ll$1% of the total yield.

The average intensity-weighted emission lifetimes for the first-order contributions, $I_1^{(1)}(t)$, were almost identical: 83.5, 80.8 and 85.3 ns for the low, medium and high power data. However, the second-order decay functions, $I_2^{(2)}(t)$, were considerably shorter with average lifetimes of 7.9 and 6.7 ns for the medium and high power decays respectively. Both $I_1^{(1)}(t)$ and $I_2^{(2)}(t)$ functions are tabulated in the Appendix B.

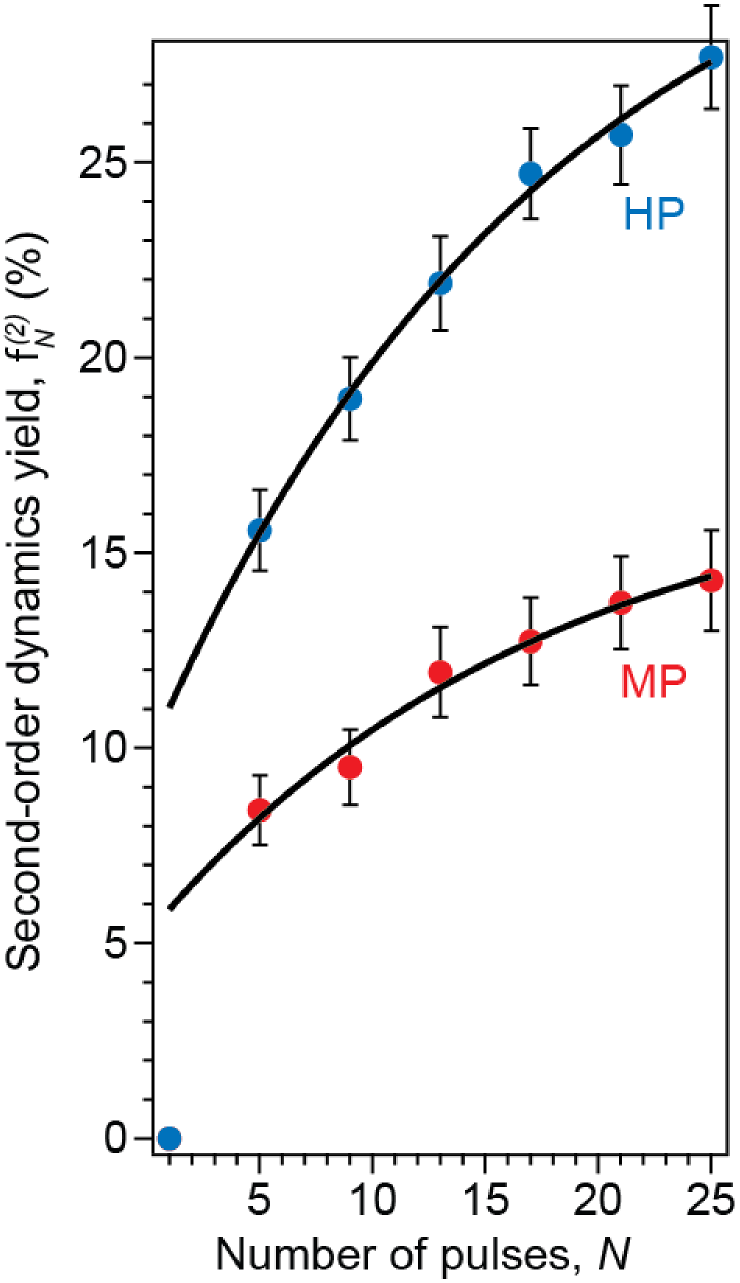

Figure 5.6 : Percentage yield, $\boldsymbol{\phi_N^{(2)}}$, of the second-order decay contributions after the N^{th} laser pulse. In each case, the error bars are ±2 × the standard deviation.

It will be useful to calculate the percentage of second order contribution as a function of excitation intensity as well as number of pulses, N. The percentage yield, $\phi_N^{(2)}$, of the second-order decay contributions after the N^{th} laser pulse is given by:

$$\phi_N^{(2)} = 100 \times \frac{\int_0^\infty \chi_N^{(2)} I_N^{(2)}(t)dt}{\int_0^\infty \left(\chi_N^{(1)} I_N^{(1)}(t) + \chi_N^{(2)} I_N^{(2)}(t)\right) dt} \tag{5.9}$$

As shown in Figure 5.6, when plotted versus N, we find that at both medium and high powers, $\phi_N^{(2)}$, is well modeled by an exponential function,

$$\phi_N^{(2)} = \phi_\infty^{(2)} - \alpha e^{-\beta N} \tag{5.10}$$

where $\phi_\infty^{(2)}$ is the second-order yield in the limit of an infinite number of pulses. Fits to both the medium power and high power yields give almost identical rate constants: $\beta = 0.057$ and 0.056 pulse^{-1}, showing that the decay dynamics of the doubly excited state is the same in both cases and therefore indicating that the same state is being created in both the cases. Furthermore, the value of $\phi_\infty^{(2)}$, which indicates the emission yield of this state under continuous illumination with an 80 MHz source, is 17.3% and 33.5% for the medium and high powers respectively.

This is considerably longer than the time it takes for the first-order dynamics to reach equilibrium (∼8 pulses or ∼100 ns), which suggests that second-order populations exist for considerably longer than excitons; however, this is at odds with the average (<10 ns) second-order PL lifetimes shown earlier.

The CdSe/CdS QDs used in this study had thick (9.25 monolayers) CdS shells, which were expected to reduce electron–hole coupling, slow Auger recombination rates,[44] and thereby increase the likelihood of second-order fluorescence. However, their relatively low emission yields (~20%) indicated that surface trapping and other nonradiative recombination pathways were active. Biexcitons are formed in CdSe/CdS QDs after absorption of two photons, and they can recombine to form (i) excitons (radiatively or nonradiatively) or (ii) charged states via Auger-induced ejection of an electron or hole.[59,86] Process (i) would explain the short second-order decay lifetimes, but simple carrier recombination does not explain the slow rise in second-order emission yield. Alternatively, a charged QD, formed via process (ii), could absorb another photon to give a trion, which also has a relatively short emission rate; however, the state formed after trion decay is the charged state, not the neutral ground state, and therefore, recovery of first-order dynamics requires that the QD discharges. If the ejected carrier is localized in a deep trap, the discharging time can be microseconds or longer, as discussed in chapter 3, and also evidenced by QD "off" time fluorescence blinking statistics.[81,87] Since the emission yield from process (ii) could build up from pulse to pulse as more charged QDs are generated, these data suggest that trion emission rather than biexciton emission is responsible for the second-order dynamics in these QDs.

5.3.3 Emission Intensities

We can further examine this model by considering the relative emission intensities of first- and second-order fluorescence contributions. Shown in Figure 5.7 a are the total count rates, J_N, for each multipulse experiment (5 μs window, Figure 5.4b) normalized by the count rate for the $N = 1$ experiment, J_1. These were calculated by summing every channel in the photon counting data, subtracting the mean background count × the number of channels, correcting for the optical density of filters in the emission path, dividing by the time taken to record the data, and finally, dividing by the total count rate for the 1-pulse decay.

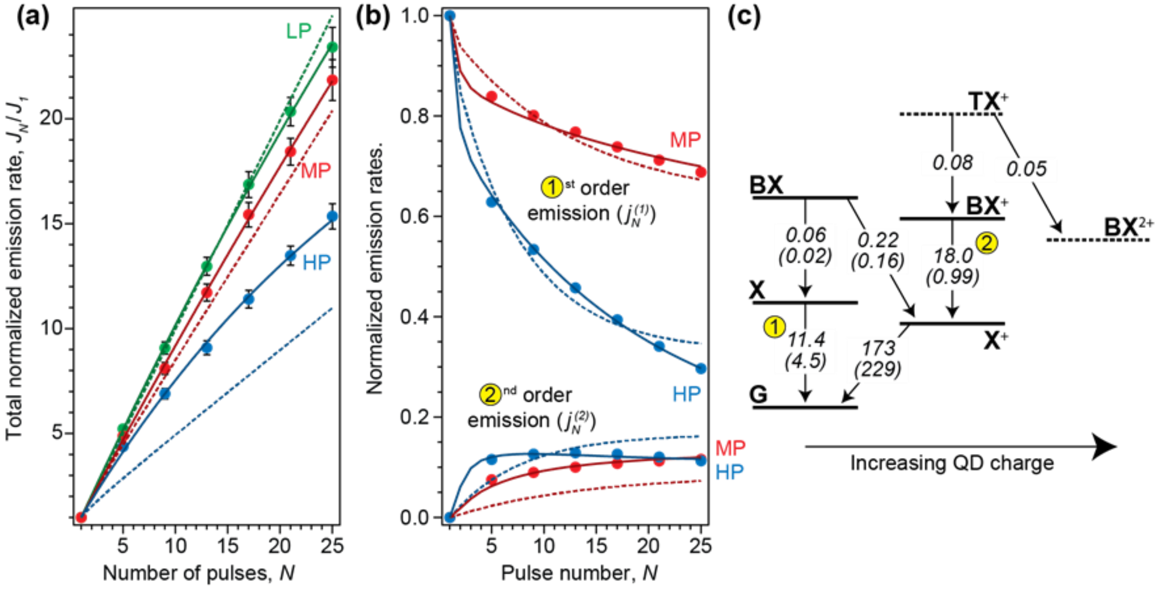

Figure 5.7: (a) Total normalized emission intensities, J_N/J_1, for low (green), medium (red), and high power (blue) experiments. Solid lines are exponential fits, and the dashed line is $J_N/J_1 = \mathrm{N}$. Uncertainties are ±1σ and are estimated from the Poisson statistics associated with single photon counting experiments. (b) Normalized first- and second-order emission intensities after the N^{th} laser pulse, j_1^N and j_2^N, for medium (red) and high power (blue) data sets. Fitted curves correspond to exciton and trion populations from fitting the five- (dashed curves) and seven-state (solid curves) schemes shown in (c). (c) Kinetic schemes used to model the j_1^N and j_2^N data in (b). The five-state scheme is shown (solid lines) with corresponding best-fit transition times (in ns) in parentheses. The seven-state scheme adds two more states (dashed lines), and the corresponding transition times are shown without parentheses. The transitions corresponding to first- and second-order emission are indicated.

At first, the low power relative emission intensities (green dots) are equal to the number of pulses, as expected from a low excitation probability. After about 17 pulses, however, the low power intensities start to rise more slowly. This is likely due to a growing population of long-lived non-emissive trap states. More significantly, the medium and high power intensities (red and blue dots) increase sub linearly. This is likely due to saturation of the exciton transition (ground state depletion), as expected if a significant proportion of QDs are excited per pulse.

To get a more revealing picture of the excited state dynamics we decomposed the total intensities, J_N, into the relative emission intensities after the N^{th} laser pulse, denoted J_N, where $j_N = (J_N - J_{N-1})/J_1$. The $(J_N - J_{N-1})$ values were calculated from the best exponential fits to the total emission intensities in Figure 5.7a (black lines). The proportion of j_N due to first- and second-order emission, $j_N^{(1)}$ and $j_N^{(2)}$, was then calculated by multiplying j_N by $1 - \phi_N^{(2)}$ and $\phi_N^{(2)}$, respectively, where $\phi_N^{(2)}$ was extrapolated from the exponential fits in Figure 5.6.

The $j_N^{(1)}$ and $j_N^{(2)}$ intensity curves for every fourth pulse are plotted for medium and high power regimes (red and blue markers, respectively) in Figure 5.7b. These data reveal that the drop in fluorescence intensity with increasing N at medium and high excitation powers (Figure 5.7a) is almost entirely due to declining first-order emission. In fact, the amount of second-order emission tends to increase with N, and although it starts to fall again in the high power experiment it is clear that the N-dependent intensity dynamics of first- and second-order emission contributions are quite different.

We can go ahead a step further, and analyze the first-order and second-order emission intensities using a kinetic scheme. To build the kinetic scheme, we followed following steps:

(i) Build a kinetic scheme, such as shown in Figure 5.7c, with initial population entirely in the ground state. Identify the transitions that will be assigned to first- and second-order emission.

(ii) Determine state populations after photoexcitation by using Poisson statistics and two adjustable expectation values, λ_{MP} and λ_{HP} (assuming the same absorption cross section for each vertical transition).

(iii) Propagate the dynamics for 12.5 ns or, if this is the *N*th pulse in an *N*-pulse sequence, for ~200 ns to allow all the population to return to the ground state.

(iv) If there are remaining pulses, return to (ii); otherwise, find the total occupation probability of first- and second-order emitting states by integrating their final-pulse population decays.

(v) Repeat for other values of *N* and normalize all the total population probabilities to those determined for $N = 1$.

(vi) Compare the calculated populations with the $j_N^{(1)}$ and $j_N^{(2)}$ data for medium and high power experiments and adjust the kinetic model until a best fit is obtained.

Using this procedure, three kinetic schemes were tested. The first was a simple three-state scheme consisting of a ground state (G), exciton (X), and biexciton (BX), but, as already anticipated from the yield data in Figure 5.6, this scheme was unable to model the $j_N^{(1)}$ and $j_N^{(2)}$data with realistic transition rates because the biexciton rapidly recombines making it impossible to reproduce the relatively slow rise in second-order emission.

We then added an Auger ionization pathway from the biexciton, creating a charged exciton (X^+) that could be subsequently photoexcited to yield a trion (BX^+). This 5-state scheme is shown in Figure 5.7c (solid lines). The first- and second-order emission was designated to arise from X and BX^+ states, respectively. Using this scheme we obtained somewhat reasonable fits to $j_N^{(1)}$ and $j_N^{(2)}$data for medium and high power experiments (dashed curves in Figure 5.7b). Transition times for the best-fit 5-state scheme are indicated in parentheses in Figure 5.7c and are broadly reasonable; however, the excitation parameters obtained for the 5-state scheme were $\lambda_{MP} = 0.95$ and $\lambda_{HP} = 3.42$, which are significantly higher than the experimentally measured values ($\lambda_{MP} = 0.15$ and $\lambda_{HP}= 1.5$).

Note that positive charging has been assumed in our notation since, in CdSe/CdS QDs, the hole wave function is localized in the core, whereas that of the electron is delocalized over the entire structure.[88,89] It is therefore likely that trions form after reversible electron trapping in surface states; however, in these experiments we were not able to distinguish the type of trion being formed.

In an attempt to further improve the fits we added a second Auger ionization step from charged triexciton (TX^+) to doubly charged biexciton (BX^{2+}). This scheme immediately yielded much better fits (solid curves in Figure 5.7b), accounting for all the trends, including the drop in second-order emission at high power after ∼13 pulses. The best-fit transition times for this scheme are shown in Figure 5.7c without parentheses and are broadly in line with what we would expect: sub-100 ps multiexciton lifetimes, exciton recombination around 10 ns, and discharging times in the hundreds of nanoseconds. In addition, the excitation parameters were $\lambda_{MP} = 0.31$ and $\lambda_{HP} = 0.72$, much closer to the measured values than for the 5-state scheme. A complete tabulated list of the 5- and 7-state fit parameters, together with estimated uncertainties, is presented in the Appendix B.

One surprise from the 7-state fit was the long trion lifetime; however, we note that despite their apparent complexity these kinetic schemes still predict single exponential first-order decay dynamics because they ignore carrier trapping and exciton fine structure, which have been shown to yield multiexponential decays.[79] Furthermore, exciton and biexciton absorption cross sections are known to differ markedly, especially at higher excitation energies due to a higher density of biexciton states.[90] This means that the assumption of equal absorption cross sections is likely not very good. Nevertheless, this analysis strongly suggests that second-order emission in these QDs comes from trions and, perhaps, higher-order charged states rather than neutral biexcitons.

So, why did we not observe biexciton emission in these QDs? In spite of a relatively thick CdS shell, emission efficiencies were poor (~20%) indicating a significant population of surface defects or trap states that could increase the rate of biexciton Auger ionization, making radiative recombination less likely. Furthermore, a significant density of CdS valence band states, associated with the shell, could have provided an efficient pathway for biexciton Auger recombination wherein a hole is excited deep into the valence band after recombination of an electron–hole pair. In the trion, we would expect Auger recombination to be statistically slower since there are eight ways for an electron–hole pair to recombine and give the excess energy to another carrier in a biexciton but only two ways in a trion. Furthermore, if negative rather than positive trions are being generated the lower density of states in the conduction band could also limit the rate of Auger recombination and promote radiative recombination of the trion.[91]

Previous work has shown that biexcitons as well as positive and negative trions can be spectrally separated.[91,92] In our studies we were unable to do this using steady state emission spectroscopy, but it should be possible, in follow-up work, to determine the spectral dependence of $\phi_N^{(2)}$, which could allow us to directly identify the nature of the emitting second-order states.

5.4 Conclusions

In this chapter, we have described a new multipulse time-resolved fluorescence experiment that is able to isolate and quantify the recombination times of multiexcited states in an ensemble QD sample. Analysis of second-order yields in a sample of CdSe/CdS core/shell QDs enabled us to exclude biexcitons as the source of second-order emission. Furthermore, calculation of N^{th} pulse emission intensities allowed us to explore several models of QD recombination dynamics, which indicated that radiative recombination from charged QDs is a likely explanation for the second-order emission.

We envisage that this multipulse time-resolved fluorescence method will be a useful tool in the study and analysis of second-order fluorescence in QDs. The ability to distinguish different sources of second-order emission could enhance our understanding of multiexciton dynamics and the effects of particle charging on QD photophysics. In combination with single particle fluorescence these measurements could yield a clearer picture of QD fluorescence blinking.

The strength of this technique lies in its ability to resolve small second-order fluorescence contributions, which, in turn, relies on the ability to control both pulse energy and pulse number. This extra dimension enables us to collect decay series that can be globally analyzed using the formalisms described here, effectively increasing the signal-to-noise ratio far beyond what is possible if the only tunable parameter is pulse energy. We can run experiments with a wide range of pulse numbers and energies, and in the next chapter, we will further expand this technique by enabling a pre-specified pulse series to be collected automatically, and use this technique to explore multiexcited state dynamics in a different system.

CHAPTER 6 : SPECTROSCOPY OF NANOSTRUCTURED METAL-QD FILMS

6.1 Motivation

The coupling of optical excitations in metal-semiconductor nanostructures has tremendous potential to create highly functional hybrid materials at the nanoscale.[42,59] Surface Plasmon (SP) is the resonant oscillation of free conduction electrons within metallic NPs that result in strong absorption of visible light. We can tailor the surface plasmon resonance by varying the size or shape of the metallic nanoparticles as well as the surrounding dielectric environment.[60] The localized electromagnetic field of SP can couple with the exciton dipole in colloidal QDs, and this coupling has been shown to modify the emission and absorption properties of QDs-leading to enhanced absorption cross-sections, increased radiative rates, and exciton-plasmon energy transfer.[61–63] However, plasmonic coupling with QD states strongly depends on the distance between the QD and the metallic NPs (Figure 6.1).[98] At very short distances, plasmon couples strongly with excitonic states in QD leading to non-radiative Rabi oscillations that completely quenches QD fluorescence. For long inter-particle distances, there is minimal interaction, but, in the intermediate coupling regime (mostly between 5-20 nm), excitons in QD can interact weakly with the plasmon oscillations leading to modification of QD's emission and absorption properties as discussed above.

Figure 6.1: Distance dependence of exciton-plasmon coupling.

Previously,[43] in our group, we have shown that CdSe/ZnS core−shell QDs localized near a rough gold thin film demonstrated significant enhancement of multiphoton emission and an increase in their radiative recombination rates. It has been observed that charge emission from trions can also be enhanced in the presence of metallic nanoparticles.[99,100]

This chapter will address this highly interesting problem of exciton-plasmon interaction in terms of following research objectives:

(1) First, extend the multi-pulse fluorescence technique to new systems such as Au NP/QD hybrid nanostructures.

(2) Explore how plasmon coupling modifies the recombination dynamics of multi-excited states in QDs?

(3) Study the strength of plasmonic interaction with QDs as a function of QD-NP distance.

6.2 Experimental methods

The optical set-up for this experiment is exactly similar to previous experiments in chapter 5 apart from few critical changes which are discussed below:

6.2.1 Sample preparation

For this study, we wanted to use well-passivated quantum dots that had negligible second-order fluorescence (due to multi-excited states) to begin with, so that any enhancement due to plasmonic coupling can be unambiguously resolved. We collaborated with Dr. Andrew Greytak[85] to get some high quality CdSe/CdS core-shell QDs[101] (Figure 6.2) that have very high emission yields, and nearly mono-exponential dynamics which remains unchanged even at very high pump-fluences. This means that these QDs have conformal ligand-coverage that prevents any trapping events which can lead to creation of photo-charged dots.

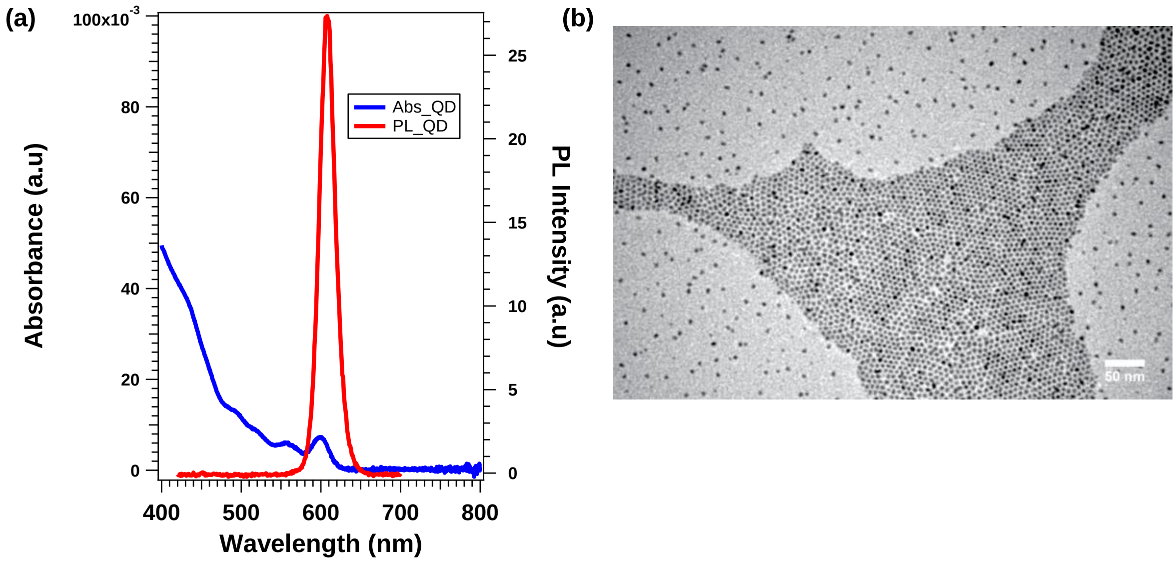

Figure 6.2: (a) UV-vis and steady state fluorescence (b) TEM images for CdSe/CdS QDs.

The hybrid metal-QD films with variable inter-layer spacing (Figure 6.3a) were prepared through following steps:

(1) Gold nanoparticles were synthesized according to the methods by Grabar et al.[102] Glass slides ($1.5\ cm \times 1.5\ cm$) functionalized with (3-aminopropyl) trimethoxysilane were then kept in gold nanoparticle solution for 24 hours. Afterwards, the glass slides were washed and characterized through UV-Vis and AFM. These steps resulted in good coverage single monolayer gold nanoparticle films.

(2) The spacer layer of variable thickness between gold film and QDs was fabricated by spin-assisted layer-by-layer deposition of positively charged (poly (allylamine)), and negatively charged (sodium 4-styrenesulfonate) polymer solutions.[103]

(3) A thin QD film was then spun cast on these gold-spacer glass slides in a N_2 filled glove-box. The thickness of QD layer was between 15-18 nm as measured by AFM (see Appendix D). The hybrid film sample was then sealed by putting a clean glass slide on top, and applying a thin layer of epoxy paste (Locite Epoxy Marine) on the sides. The epoxy sealed film was then left in glove-box to cure for 12 hours, and was ready to use after that.

For this experiment, four samples were made: QD on spacer/glass as control, QD/5 nm spacer/Au, QD/15 nm spacer/Au, and QD/25 nm spacer/Au (see figure 6.3a)

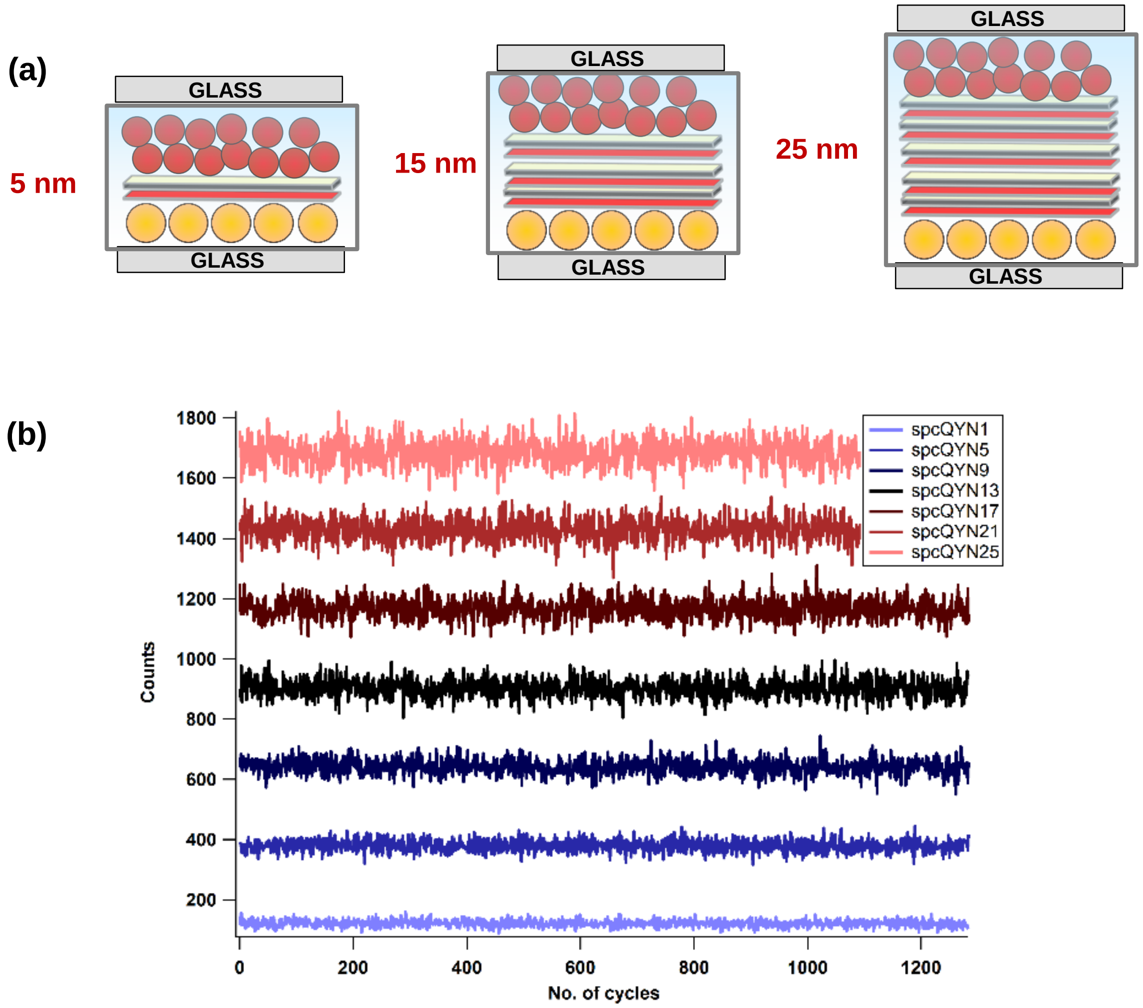

Figure 6.3: (a) A simple schematic depicting sample construction of hybrid films used in this study (b) Average sample intensity for different pulse sequences as a function of time; denoting sample photo-stability.

6.2.2 Data Collection

The data was collected automatically by a homebuilt LabVIEW program (Figure 6.4). The LabVIEW module changed the pulse sequences, initialized two different photon counting cards, synchronized data collection between both the cards, changed the neutral density filters if the emission rate exceeded 1% of excitation rate, and also did onboard data analysis to display lifetime decays in real time. Further the program is designed in a modular way so that if any additional step has to be performed, the program can be modified easily.

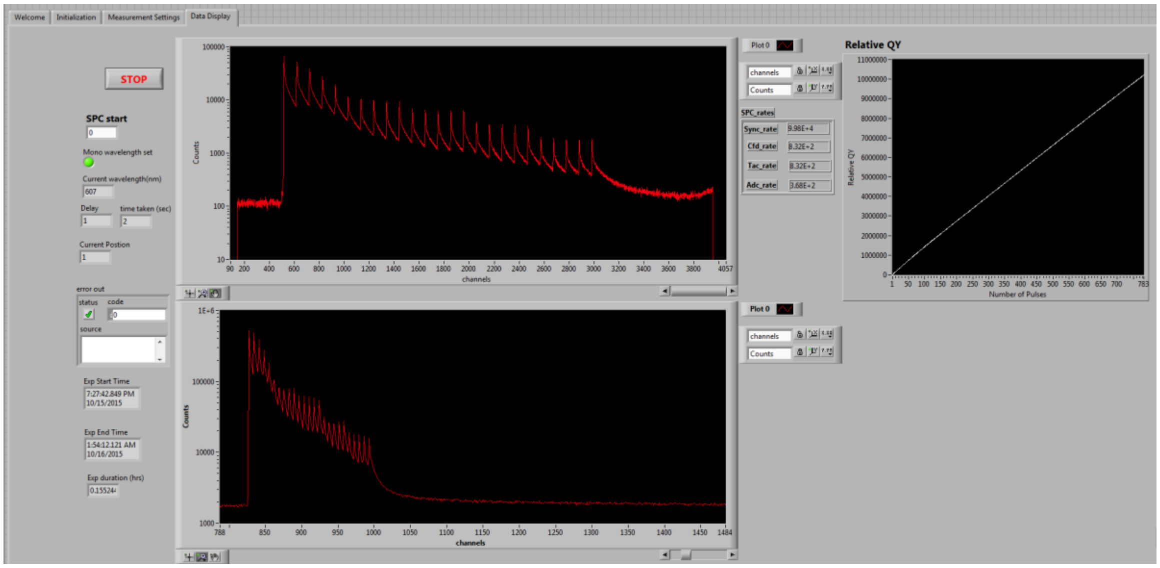

SPC start: 0
Mono wavelength set: ●
Current wavelength(nm): 607
Delay: 1
time taken (sec): 2
Current Postion: 1
error out
status: ✓
code: 0
source:
Exp Start Time: 7:27:42.849 PM 10/15/2015
Exp End Time: 1:54:12.121 AM 10/16/2015
Exp duration (hrs): 0.15524

SPC_rates
Sync_rate: 9.98E+4
Cfd_rate: 8.32E+2
Tac_rate: 8.32E+2
Adc_rate: 3.68E+2

Figure 6.4: A screenshot of the home-built LabVIEW program collecting multi-pulse data for short and long time windows.

Further, we didn't collect data for each pulse- sequence in one go as we wanted to make sure that QDs weren't photo-degrading as we collected data thereby introducing additional decay components that cannot be account for. Therefore, for each pulse-sequence we collected data for just 20 seconds, and proceeded to next pulse sequence. This cycle was repeated until we had decent counts for all the pulse sequences. This procedure ensured that any changes on account of sample degradation were averaged out. This procedure also serves as a good tool for real time monitoring of average sample quantum yields both as a function of number of pulses, *N*, and time (Figure 6.3b).

6.2.3 Data Analysis

The data fitting and analysis methodology is similar to that adopted in chapter 5 apart from few important changes.

For each sample, a short (500 ns) and long (7μs) decay pair was collected for 9 different pulse sequences (containing 1, 2, 3, 4, 5, 10, 15, 20, 25 pulses) at medium power ($\langle n \rangle = 0.15$). The final decay for each *N*-pulse pair (short and long time window) was simultaneously modeled with one multiexponential decay function convoluted with the measured 1-pulse instrument response function.

6.3 Results and discussion

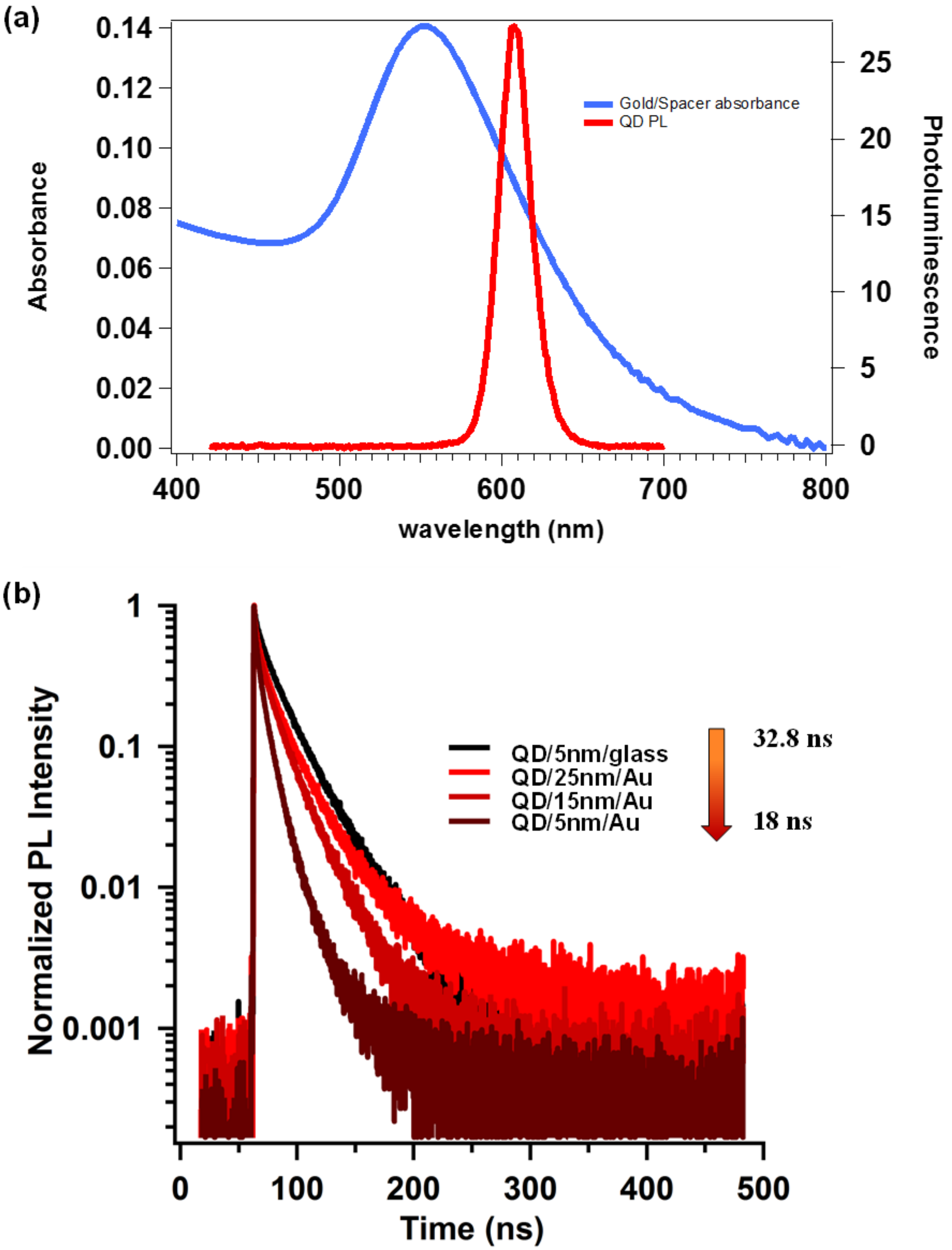

Figure 6.5: (a) Spectral overlap of plasmon resonance with exciton emission (b) Single pulse decays at medium excitation power.

Figure 6.5b shows the single pulse decays for all the four samples. Clearly, the presence of gold nanoparticles causes the sample to decay at a faster rate. This is expected because presence of metal can enhance emission rates or add new pathways for non-radiative transfer, both of which would cause the lifetimes to become shorter.

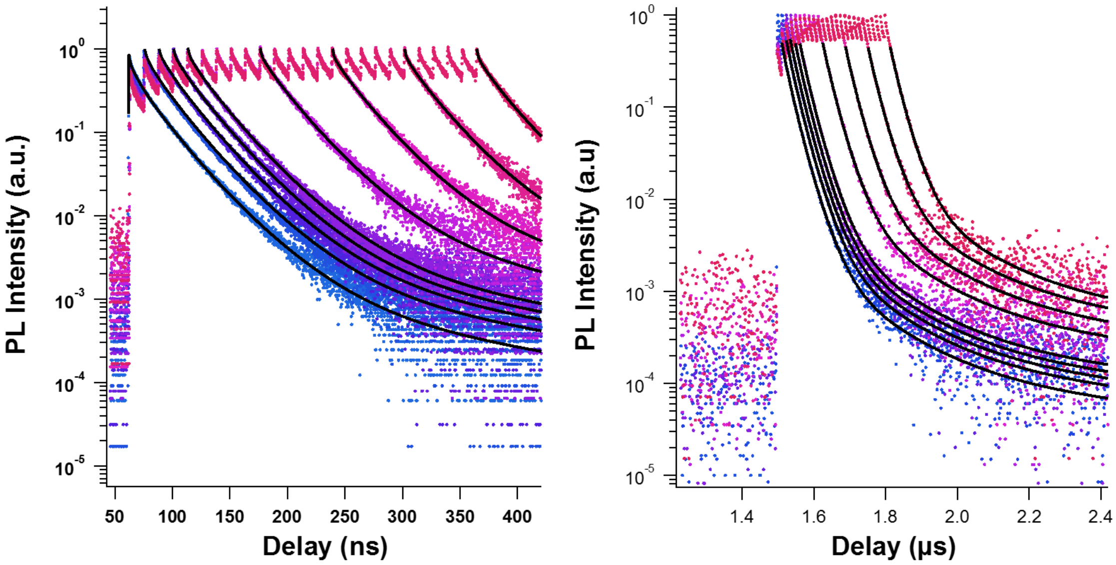

Figure 6.6 : Representative multi-pulse decays (short and long) for QD film on spacer/glass for different pulse sequences (containing 1, 2, 3, 4, 5, 10, 15, 20, 25 pulses).

Figure 6.6 displays the representative multi-pulse decays (short and long time window) for the QD on spacer sample. Fitting of multi-pulse data revealed that all the samples required a second order decay function, $I_N^{(2)}$ to satisfy the fitting criteria defined in the previous chapter. Barring the QD film sample that required a single sub-nanosecond component, for all other QD-Au hybrid samples, $I_N^{(2)}$ was found to be a bi-exponential function comprising of a sub-ns component just like the QD sample but also a 3-5 ns long component. Clearly, presence of gold nanoparticles modified second-order recombination dynamics.

However, even more interesting was the evolution of second-order yields as a function of QD- gold NPs separation (Figure 6.7).

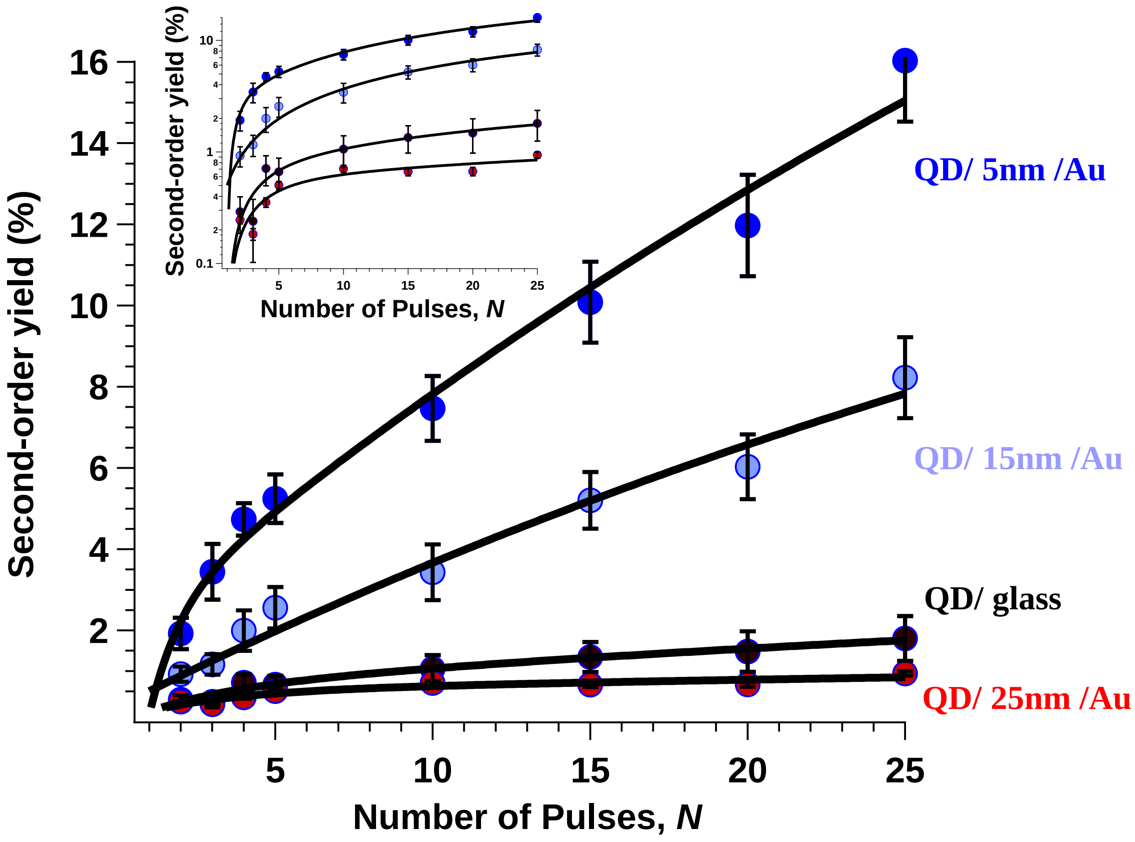

Figure 6.7: Second-order percentage yields, $\phi_N^{(2)}$, after N laser pulse for all the four samples. For each curve, the error bars are ±2 × the standard deviation. The solid black lines are bi-exponential fits to experimental data points. The inset shows the same figure on a semi-log axis.

First, QD film sample by itself had a very low second order yield of around 1-2%. Also, the QD-Au sample separated by 25 nm also has a very small second order contribution. This was expected because if the inter layer distance is large enough there would be no coupling between the gold NP surface plasmon and QD exciton states. Further, as the QD and metal NP layer gets closer, the second order yield increased by almost an order of magnitude, from 1.5% to 16% for the 5 nm separation between QDs and Au NP film. This is a very promising evidence that plasmon coupling can enhance multi-excited state fluorescence because as discussed in the previous chapter, second-order fluorescence in our experiment can only arise from multiply excited states.

More-over, all the four second-order yield vs N functions can be modeled by the following bi-exponential-function:

$$\phi_N^{(2)} = \phi_\infty^{(2)} - \alpha_1 e^{-\beta_1 N} - \alpha_2 e^{-\beta_2 N} \tag{6.1}$$

Further, similar to what we observed in the previous chapter where both medium and high power experiments had same rate constant for second-order yields, all the samples irrespective of inter-particle separation have same value for β_2, 0.18 pulse^{-1} (more visible on a semi-log plot as shown in the inset of Figure 6.7). This is a clear indication that it’s the same state which is responsible for second-order dynamics in all the three samples, and is most likely an emissive Trion state as we have seen in the previous chapter.

6.4 Conclusions

First, we clearly established that there is a distance dependence on exciton-plasmon coupling, and second order fluorescence from QDs is greatly enhanced in the presence of gold nanoparticles. Further, all the three samples irrespective of inter-particle (QD and Au NPs) separation had the same rate constant for one of the exponential functions used to model the second-order yields, thereby strongly indicating that it’s the same state which was probably responsible for multi-excited state fluorescence.

CHAPTER 7 : RELATED EXPERIMENTS: DELAYED FLUORESCENCE[⊥]

7.1 Overview

Formation of spin-forbidden triplet states in organic dyes, such as porphyrins, have recently acquired considerable interest for possible applications in photovoltaics, photo-catalysts, and singlet oxygen generation for killing tumor cells.[104,105] It is therefore essential to quantify triplet quantum yields in these organic systems.

Bachilo and Weisman[106] have shown that delayed fluorescence arising due to triplet–triplet recombination can be used to accurately calculate triplet quantum yields. The delayed fluorescence may last for few hundred microseconds, and is several orders of magnitude weaker than singlet fluorescence. A single short laser pulse (a few hundred fs long) typically employed to measure fast fluorescence dynamics is insufficient to build up a significant triplet population, in order to observe weak emission by triplet–triplet annihilation. One way to overcome this obstacle is to use excitation pulses of longer duration as employed by Bachilo and Weisman in their study. However, that would make the recording of fluorescence unfeasible. Another way is to use a burst of high repetition rate pulses to build up the triplet state population. We therefore use our multi-pulse technique introduced in previous chapters to excite a sample with a controllable number of 80 MHz laser pulses.

[⊥] Some content in this chapter is adapted from my contributed work as a co-author towards

One distinct advantage of our approach is that both the delayed fluorescence and the fast singlet fluorescence can be measured using the same time resolved fluorescence setup by a femtosecond laser.

7.2 Experimental methods

Triplet–triplet annihilation fluorescence was recorded using a femtosecond Ti:saphire laser (Spectra Physics MaiTai), operating at 80 MHz repetition rate and 820 nm. The laser output was fed to an optical parametric oscillator (OPO) (Spectra Physics Inspire). The frequency-doubled output (410 nm) from the OPO was then directed through two electro-optic modulators (Conoptics 350-105 KD*P Series) driven by a high voltage push– pull power amplifier. A delay generator (SRS DG535), externally triggered by a synchronous counter operating at 4 kHz, was used to produce an electronic gate of variable length, which determined the length of the optical gate opened by the pulsepicker system. An electronic gate of suitable length was chosen to excite the sample with 100 pulses. The excitation light was focused on a degassed sample solution inside a 10 mm sealed quartz cuvette. Fluorescence dynamics were measured by time correlated single photon counting, using a multichannel photon counting board (Becker & Hickl DPC 230) with a double monochromator (Spectral Products CM112) and a hybrid PMT detector (Becker & Hickl HPM-100-40).

7.3 Results and discussion

One of the main goals of this study was to measure the changes in triplet quantum yields for singly halogenated carbomethoxyphenyl porphyrins when the halogen group was varied[107] on account of heavy atom effect. Figure 7.1 shows the structure of these three derivatives that we worked with.

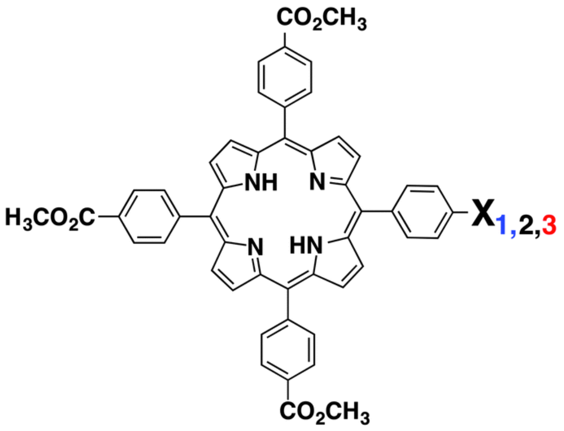

1: X = CO_2CH_3 - 5,10,15,20-tetrakis(4-carbomethoxyphenyl)porphyrin
2: X = Br - 5,10,15,-tris(4-carbomethoxyphenyl)-20-(4-bromophenyl)porphyrin
3: X = I - 5,10,15-tris(4-carbomethoxyphenyl)-20-(4-iodophenyl)porphyrin

Figure 7.1: The structure and names of three carbomethoxyphenylporphyrin derivatives used in this study.

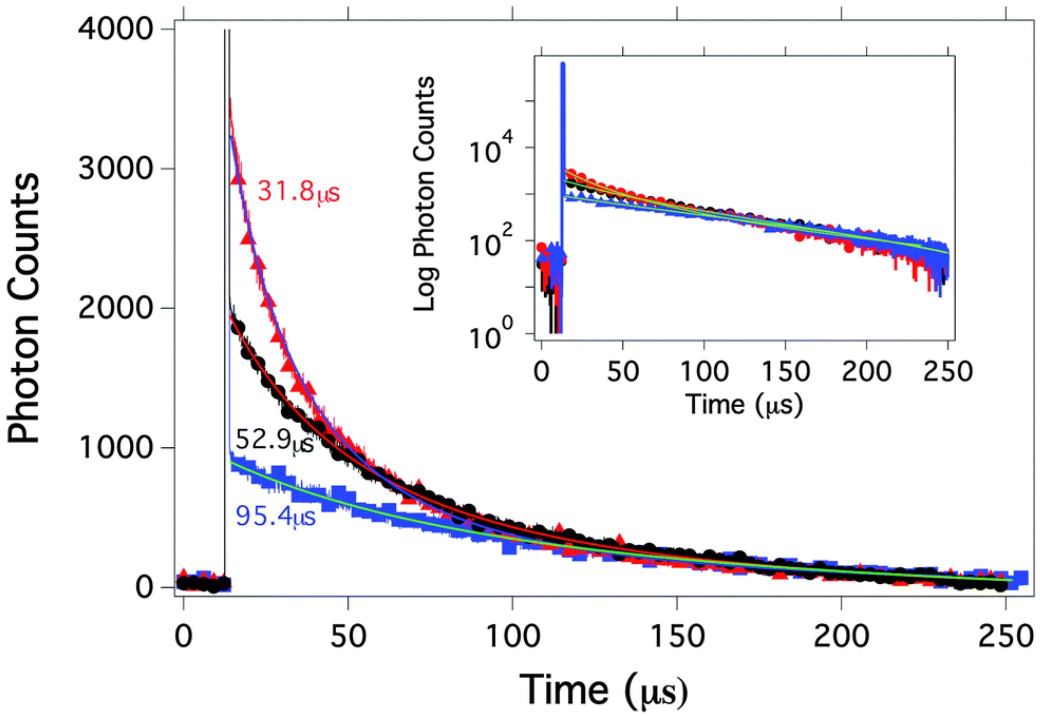

Figure 7.2 : Delayed fluorescence of (1) TCM$_4$PP (■), (2) TBCM$_3$PP (·) and (3) TCM$_3$IPP (Δ) with average lifetimes. The inset shows the normalized overlaid prompt fluorescence on a logarithmic scale for (1) TCM$_4$PP (■), (2) TBCM$_3$PP (·) and (3) TCM$_3$IPP (Δ).

Fig. 7.2 shows the multi-pulse prompt (fast singlet fluorescence) and delayed fluorescence decays for three different porphyrin derivatives: (1) TCM$_4$PP, (2) TBCM$_3$PP and (3) TCM$_3$IPP . Clearly, the emission decay consists of a fast singlet fluorescence peak in the early period, and a weak but very long decay component building up on account of triplet–triplet recombination. The intense narrow peak in the beginning actually consists of 100 singlet decays but looks flat because channel width was on the scale of few tens of nanoseconds thus masking the fast singlet transient. The triplet quantum yields were then extracted from delayed fluorescence data using the procedure laid by Weisman’s group.

Slower delayed fluorescence can be modeled by a simple second order model as shown by Weismann and his group, and the corresponding second order rate constant for triplet–triplet annihilation, k_A, was found by fitting the intensity of the delayed fluorescence. However, the key result in this experiment was that iodine substituted porphyrin had the hightest triplet quantum yield around 0.88. And this was expected as iodine being the heaviest atom, would lead to greater singlet to triplet conversion efficiency because iodine is larger and therefore has the strongest spin-orbit coupling.

7.4 Conclusions

The experiment we performed above is neither novel nor exceptional in the sense that the same experiment can be done by using an optical chopper wheel that can modulate the excitation laser at few kHz or ten of kHz at best. This would give us a longer excitation profile to create a substantial population of emitting states, similar to what we have done above by using a long gated excitation pulse. However, the significant advantage that we have is that we can modulate our excitation profile anywhere from 12.5 ns to few seconds in steps of 12.5 ns. This kind of powerful dynamic range could be very useful in experiments that probe dynamics that can happen on a faster scale such as quenching of triplet states by some external process or molecular species.We hope to do such kind of studies in future to glean more information on longer lived states in porphyrin or porphyrin like systems.

CHAPTER 8 : CONCLUSIONS AND FUTURE WORK

The basic focus of this thesis has been to advance the understanding of photo-physics in semiconductor nanocrystals (NCs) or quantum dots (QDs). Furthermore, the focus has been to understand the exciton dynamics in ensemble systems, and explain it in terms of dynamical processes happening in individual nanocrystals. This is inherently a challenging task because of size inhomogeneity in colloidal nanocrystals and strong interaction of NCs with its microscopic environment. Therefore, we have devoted considerable efforts on designing a state of art but flexible ultrafast time-resolved spectroscopy system as described in this thesis, so that we can measure NC dynamics as a function of several variables in controlled conditions, and with excellent statistics in order to fit those dynamics with simple but powerful global models. The temperature-resolved experiments discussed in chapter 2 is an effective example of such kind of approach.

This thesis has made some original and innovative contributions to the study of multi-excited states in ensemble systems. We began with a very simplistic approach of changing pulse rate to generate multi-excited states, but quickly realized that we need a technique that can excite QDs in a much-more controlled and systematic way, and that led to development of multi-pulse time resolved fluorescence – a novel technique to resolve multi-excited states in ensemble QDs. Furthermore, we showed that the multi-pulse technique can also resolve the nature of underlying multi-excited state, whether it is a biexciton or a charged trion. We further demonstrated the applicability of this technique to other systems such as semiconductor-metal nanostructures, and successfully showed that this technique can capture changes in multi-excited state dynamics on interaction with external fields such as those generated by plasmons in metallic nanoparticles.

We also demonstrated some unintended but fruitful applications of our technique such as studying the dynamics of long-lived but not very bright transitions like those generated by triplet-triplet annihilation in porphyrin dyes.

There are several areas discussed in this thesis that still needs to be addressed such as the rate constant, β, which crops up while modelling second-order yields, and tends to remain constant irrespective of the excitation (medium vs high power) density or changes in QD environment (plasmon-coupling). In our analysis, we haven't connected, β, to a physical process or some other underlying cause. Second, it will be interesting to know how second-order dynamics would change if we increase or decrease the spectral overlap of plasmon-exciton resonances. Also, it would be prudent to verify if the multi-pulse technique is probably more sensitive to charged states thus unable to detect bi-excitons. For these kind of experiments, we would need a material with relatively high bi-exciton quantum yields. Another interesting experiment would be developing approaches to further reduce the inter-pulse period, of 12.5 ns, in our experiment to probe excited states that may not live that long enough to be excited again.

On the whole, to exploit the full potential of such an interesting material like quantum dots, it's essential to develop new spectroscopy techniques and analysis methods particularly for ensemble systems that otherwise present a challenge to microscopic understanding of QD photo-physics.

REFERENCES

1. Alivisatos, A. P. Perspectives on the Physical Chemistry of Semiconductor Nanocrystals. **3654,** 13226–13239 (1996).

2. Kuno, M. *Introductory Nanoscience: Physical and Chemical Concepts*. (Garland Science, 2011).

3. Kang, K. I. *et al.* Confinement-enhanced biexciton binding energy in semiconductor quantum dots. *Phys. Rev. B* **48,** 15449–15452 (1993).

4. Koch, M., Kheng, K., Robin, I. C. & André, R. Biexcitonic complexes and the decay dynamics of trion and exciton in a single CdSe quantum dot. *Phys. Status Solidi C* **3,** 3916–3919 (2006).

5. Caruge, J.-M., Chan, Y., Sundar, V., Eisler, H. & Bawendi, M. Transient photoluminescence and simultaneous amplified spontaneous emission from multiexciton states in CdSe quantum dots. *Phys. Rev. B* **70,** 085316 (2004).

6. Sanguinetti, S., Guzzi, M., Gatti, E. & Gurioli, M. in *Characterization of Semiconductor Heterostructures and Nanostructures (Second Edition)* (eds. Lamberti, C. & Agostini, G.) 509–556 (Elsevier, 2013). at <http://www.sciencedirect.com/science/article/pii/B9780444595515000121>

7. The many aspects of quantum dots. *Nat. Nanotechnol.* **5,** 381–381 (2010).

8. Kim, J. Y., Voznyy, O., Zhitomirsky, D. & Sargent, E. H. 25th Anniversary Article: Colloidal Quantum Dot Materials and Devices: A Quarter-Century of Advances. *Adv. Mater.* **25,** 4986–5010 (2013).

9. By Kevin Bullis on January 11, 2013. Quantum Dots Produce More Colorful Sony TVs. *MIT Technology Review* at <http://www.technologyreview.com/news/509801/quantum-dots-get-commercial-debut-in-more-colorful-sony-tvs/>

10. 3M Announces Rec. 2020 Readiness at Display Week 2015. *Nanosys - Quantum Dot Pioneers* at <http://www.nanosysinc.com/press-releases-archive/2015/6/2/3m-announces-rec-2020-readiness-at-display-week-2015>

11. Poor, A. Will Quantum Dots Dominate Displays? (2014). at <http://spectrum.ieee.org/semiconductors/materials/will-quantum-dots-dominate-displays>

12. QLED market forecast reports mass production of commercialized quantum dots is a game-changer | Solid State Technology. at <http://electroiq.com/blog/2013/03/qled-market-forecast-reports-mass-production-of-commercialized-q/>

13. Beard, M. c. & Ellingson, R. J. Multiple exciton generation in semiconductor nanocrystals: Toward efficient solar energy conversion. *Laser Photonics Rev.* **2,** 377–399 (2008).

14. Nozik, A. J. Quantum dot solar cells. *Phys. E Low-Dimens. Syst. Nanostructures* **14,** 115–120 (2002).

15. Beard, M. C., Luther, J. M., Semonin, O. E. & Nozik, A. J. Third Generation Photovoltaics based on Multiple Exciton Generation in Quantum Confined Semiconductors. *Acc. Chem. Res.* **46,** 1252–1260 (2013).

16. Kamat, P. V. Quantum Dot Solar Cells. The Next Big Thing in Photovoltaics. *J. Phys. Chem. Lett.* **4,** 908–918 (2013).

17. Loss, D. & DiVincenzo, D. P. Quantum Computation with Quantum Dots. *Phys. Rev. A* **57,** 120–126 (1998).

18. Bimberg, D. Quantum dots for lasers, amplifiers and computing. *J. Phys. Appl. Phys.* **38,** 2055 (2005).

19. Stiff-Roberts, A. D. Quantum-dot infrared photodetectors: a review. *J. Nanophotonics* **3,** 031607–031607–17 (2009).

20. Flügge, S. *Practical Quantum Mechanics*. (Springer, 1998).

21. Bányai, L. & Koch, S. W. *Semiconductor Quantum Dots*. (World Scientific, 1993).

22. Efros, A. L. & Rosen, M. The Electronic Structure of Semiconductor Nanocrystals1. *Annu. Rev. Mater. Sci.* **30,** 475–521 (2000).

23. Klimov, V. I. *Semiconductor and Metal Nanocrystals: Synthesis and Electronic and Optical Properties*. (CRC Press, 2003).

24. Zhang, J. Z. *Optical Properties and Spectroscopy of Nanomaterials*. (WORLD SCIENTIFIC, 2009). at <http://www.worldscientific.com/worldscibooks/10.1142/7093>

25. Klimov, V. I. *et al.* Optical Gain and Stimulated Emission in Nanocrystal Quantum Dots. *Science* **290,** 314–317

26. Peterson, M. D. *et al.* The Role of Ligands in Determining the Exciton Relaxation Dynamics in Semiconductor Quantum Dots. *Annu. Rev. Phys. Chem.* **65,** 317–339 (2014).

27. Henini, M. Self-assembled quantum dots. *III-Vs Rev.* **10,** 25–30 (1997).

28. Murray, C. B., Kagan, C. R. & Bawendi, M. G. Synthesis and Characterization of Monodisperse Nanocrystals and Close-Packed Nanocrystal Assemblies. *Annu. Rev. Mater. Sci.* **30,** 545–610 (2000).

29. Murray, C. B., Norris, D. J. & Bawendi, M. G. Synthesis and characterization of nearly monodisperse CdE (E = sulfur, selenium, tellurium) semiconductor nanocrystallites. *J. Am. Chem. Soc.* **115,** 8706–8715 (1993).

30. LaMer, V. K. & Dinegar, R. H. Theory, Production and Mechanism of Formation of Monodispersed Hydrosols. *J. Am. Chem. Soc.* **72,** 4847–4854 (1950).

31. Hines, M. A. & Guyot-Sionnest, P. Synthesis and Characterization of Strongly Luminescing ZnS-Capped CdSe Nanocrystals. *J. Phys. Chem.* **100,** 468–471 (1996).

32. Reiss, P., Protière, M. & Li, L. Core/Shell semiconductor nanocrystals. *Small Weinh. Bergstr. Ger.* **5,** 154–68 (2009).

33. Li, J. J. *et al.* Large-Scale Synthesis of Nearly Monodisperse CdSe/CdS Core/Shell Nanocrystals Using Air-Stable Reagents via Successive Ion Layer Adsorption and Reaction. *J. Am. Chem. Soc.* **125,** 12567–12575 (2003).

34. Lo, S. S., Mirkovic, T., Chuang, C.-H., Burda, C. & Scholes, G. D. Emergent Properties Resulting from Type-II Band Alignment in Semiconductor Nanoheterostructures. *Adv. Mater.* **23,** 180–197 (2011).

35. Nozik, A. J. Multiple exciton generation in semiconductor quantum dots. *Chem. Phys. Lett.* **457,** 3–11 (2008).

36. Beard, M. C. *et al.* Comparing multiple exciton generation in quantum dots to impact ionization in bulk semiconductors: implications for enhancement of solar energy conversion. *Nano Lett.* **10,** 3019–27 (2010).

37. Kambhampati, P. Unraveling the structure and dynamics of excitons in semiconductor quantum dots. *Acc. Chem. Res.* **44,** 1–13 (2011).

38. Efros, A. L. & Rosen, M. Random Telegraph Signal in the Photoluminescence Intensity of a Single Quantum Dot. *Phys. Rev. Lett.* **78,** 1110–1113 (1997).

39. Jones, M., Lo, S. S. & Scholes, G. D. Quantitative modeling of the role of surface traps in CdSe/CdS/ZnS nanocrystal photoluminescence decay dynamics. *Proc. Natl. Acad. Sci. U. S. A.* **106,** 3011–6 (2009).

40. Schaller, R. D., Sykora, M., Jeong, S. & Klimov, V. I. High-Efficiency Carrier Multiplication and Ultrafast Charge Separation in Semiconductor Nanocrystals Studied via Time-Resolved Photoluminescence†. *J. Phys. Chem. B* **110,** 25332–25338 (2006).

41. Klimov, V. I. Mechanisms for Photogeneration and Recombination of Multiexcitons in Semiconductor Nanocrystals: Implications for Lasing and Solar Energy Conversion. *J. Phys. Chem. B* **110,** 16827–16845

42. Nair, G. & Bawendi, M. G. Carrier multiplication yields of CdSe and CdTe nanocrystals by transient photoluminescence spectroscopy. *Phys. Rev. B* **76,** 081304

43. Klimov, V. I. Spectral and dynamical properties of multiexcitons in semiconductor nanocrystals. *Annu. Rev. Phys. Chem.* **58,** 635–73 (2007).

44. Htoon, H. *et al.* Highly emissive multiexcitons in steady-state photoluminescence of individual ‘giant’ CdSe/CdS Core/Shell nanocrystals. *Nano Lett.* **10,** 2401–7 (2010).

45. Tyagi, P. & Kambhampati, P. False multiple exciton recombination and multiple exciton generation signals in semiconductor quantum dots arise from surface charge trapping. *J. Chem. Phys.* **134,** 094706 (2011).

46. McGuire, J. A., Sykora, M., Joo, J., Pietryga, J. M. & Klimov, V. I. Apparent Versus True Carrier Multiplication Yields in Semiconductor Nanocrystals. *Nano Lett.* **10,** 2049–2057 (2010).

47. Nair, G., Geyer, S. M., Chang, L.-Y. & Bawendi, M. G. Carrier multiplication yields in PbS and PbSe nanocrystals measured by transient photoluminescence. *Phys. Rev. B* **78,** 125325

48. Shabaev, A., Hellberg, C. S. & Efros, A. L. Efficiency of Multiexciton Generation in Colloidal Nanostructures. *Acc. Chem. Res.* **46,** (2013).

49. Nair, G., Zhao, J. & Bawendi, M. G. Biexciton Quantum Yield of Single Semiconductor Nanocrystals from Photon Statistics. *Nano Lett.* 1136–1140 (2011).

50. Schaller, R. & Klimov, V. High Efficiency Carrier Multiplication in PbSe Nanocrystals: Implications for Solar Energy Conversion. *Phys. Rev. Lett.* **92,** 186601 (2004).

51. Semonin, O. E. *et al.* Peak external photocurrent quantum efficiency exceeding 100% via MEG in a quantum dot solar cell. *Science* **334,** 1530–3 (2011).

52. Muller, A., Fang, W., Lawall, J. & Solomon, G. S. Creating Polarization-Entangled Photon Pairs from a Semiconductor Quantum Dot Using the Optical Stark Effect. *Phys. Rev. Lett.* **103,** (2009).

53. Stevenson, R. M. *et al.* A semiconductor source of triggered entangled photon pairs. *Nature* **439,** 179–182 (2006).

54. McGuire, J. A., Joo, J., Pietryga, J. M., Schaller, R. D. & Klimov, V. I. New Aspects of Carrier Multiplication in Semiconductor Nanocrystals. *Acc. Chem. Res.* **41,** 1810–1819 (2008).

55. Dahan, M. *et al.* Diffusion Dynamics of Glycine Receptors Revealed by Single-Quantum Dot Tracking. *Science* **302,** 442–445 (2003).

56. Courty, S., Luccardini, C., Bellaiche, Y., Cappello, G. & Dahan, M. Tracking Individual Kinesin Motors in Living Cells Using Single Quantum-Dot Imaging. *Nano Lett.* **6,** 1491–1495 (2006).

57. Zhao, J. *et al.* Efficient CdSe/CdS Quantum Dot Light-Emitting Diodes Using a Thermally Polymerized Hole Transport Layer. *Nano Lett.* **6,** 463–467 (2006).

58. Achermann, M. Exciton−Plasmon Interactions in Metal−Semiconductor Nanostructures. *J. Phys. Chem. Lett.* **1,** 2837–2843 (2010).

59. Leblanc, S. J., McClanahan, M. R., Jones, M. & Moyer, P. J. Enhancement of Multiphoton Emission from Single CdSe Quantum Dots Coupled to Gold Films. *Nano Lett.* **13,** 1662–9 (2013).

60. Becker, W. in *Advanced Time-Correlated Single Photon Counting Techniques* (eds. Jr, P. A. W. C., Toennies, P. J. P. & Zinth, P. W.) 11–25 (Springer Berlin Heidelberg, 2005). at <http://link.springer.com/chapter/10.1007/3-540-28882-1_2>

61. Birch, D. J. S. & Imhof, R. E. in *Topics in Fluorescence Spectroscopy* (ed. Lakowicz, J. R.) 1–95 (Springer US, 2002). at <http://link.springer.com/chapter/10.1007/0-306-47057-8_1>

62. Jones, M., Lo, S. S. & Scholes, G. D. Signatures of Exciton Dynamics and Carrier Trapping in the Time-Resolved Photoluminescence of Colloidal CdSe Nanocrystals. *J Phys Chem C* **113,** 18632–18642 (2009).

63. Elliott, C., Vijayakumar, V., Zink, W. & Hansen, R. National Instruments LabVIEW: A Programming Environment for Laboratory Automation and Measurement. *J. Assoc. Lab. Autom.* **12,** 17–24 (2007).

64. Chen, Y. *et al.* ‘Giant’ multishell CdSe nanocrystal quantum dots with suppressed blinking. *J. Am. Chem. Soc.* **130,** 5026–7 (2008).

65. Malko, A. V. *et al.* Pump-Intensity- and Shell-Thickness-Dependent Evolution of Photoluminescence Blinking in Individual Core/Shell CdSe/CdS Nanocrystals. *Nano Lett.* **11,** 5213–5218 (2011).

66. Jones, M. & Scholes, G. D. On the use of time-resolved photoluminescence as a probe of nanocrystal photoexcitation dynamics. *J. Mater. Chem.* **20,** 3533 (2010).

67. Clapp, A. R., Goldman, E. R. & Mattoussi, H. Capping of CdSe–ZnS quantum dots with DHLA and subsequent conjugation with proteins. *Nat. Protoc.* **1,** 1258–1266 (2006).

68. Li, J. J. *et al.* Large-scale synthesis of nearly monodisperse CdSe/CdS core/shell nanocrystals using air-stable reagents via successive ion layer adsorption and reaction. *J. Am. Chem. Soc.* **125,** 12567–75 (2003).

69. O'Connor, D. *Time-correlated single photon counting*. (Academic Press, 1984).

70. Califano, M., Franceschetti, A. & Zunger, A. Temperature Dependence of Excitonic Radiative Decay in CdSe Quantum Dots: The Role of Surface Hole Traps. *Nano Lett.* **5,** 2360–2364 (2005).

71. Bässler, H. Charge Transport in Disordered Organic Photoconductors a Monte Carlo Simulation Study. *Phys. Status Solidi B* **175,** 15–56 (1993).

72. van Driel, A. F. *et al.* Frequency-Dependent Spontaneous Emission Rate from CdSe and CdTe Nanocrystals: Influence of Dark States. *Phys. Rev. Lett.* **95,** 236804 (2005).

73. Crooker, S. A., Barrick, T., Hollingsworth, J. A. & Klimov, V. I. Multiple temperature regimes of radiative decay in CdSe nanocrystal quantum dots: Intrinsic limits to the dark-exciton lifetime. *Appl. Phys. Lett.* **82,** 2793–2795 (2003).

74. Efros, null *et al.* Band-edge exciton in quantum dots of semiconductors with a degenerate valence band: Dark and bright exciton states. *Phys. Rev. B Condens. Matter* **54,** 4843–4856 (1996).

75. Williams, E. S. *et al.* Characterizing the Influence of TOPO on Exciton Recombination Dynamics in Colloidal CdSe Quantum Dots. *J. Phys. Chem. C* **117,** 4227–4237 (2013).

76. Baker, D. R. & Kamat, P. V. Tuning the Emission of CdSe Quantum Dots by Controlled Trap Enhancement. *Langmuir* **26,** 11272–11276 (2010).

77. De Mello Donegá, C., Bode, M. & Meijerink, A. Size- and temperature-dependence of exciton lifetimes in CdSe quantum dots. *Phys. Rev. B* **74,** 085320 (2006).

78. Harrison, W. A. *Applied Quantum Mechanics*. (World Scientific, 2000).

79. Jones, M., Lo, S. S. & Scholes, G. D. Quantitative modeling of the role of surface traps in CdSe/CdS/ZnS nanocrystal photoluminescence decay dynamics. *Proc. Natl. Acad. Sci.* **106,** 3011–3016 (2009).

80. Kim, J. *et al.* Mechanism and origin of exciton spin relaxation in CdSe nanorods. *J. Phys. Chem. B* **110,** 25371–25382 (2006).

81. Krauss, T. D. & Peterson, J. J. Bright Future for Fluorescence Blinking in Semiconductor Nanocrystals. *J. Phys. Chem. Lett.* **1,** 1377–1382 (2010).

82. Galland, C. *et al.* Two types of luminescence blinking revealed by spectroelectrochemistry of single quantum dots. *Nature* **479,** 203–207 (2011).

83. Neuhauser, R. G., Shimizu, K. T., Woo, W. K., Empedocles, S. A. & Bawendi, M. G. Correlation between Fluorescence Intermittency and Spectral Diffusion in Single Semiconductor Quantum Dots. *Phys. Rev. Lett.* **85,** 3301–3304 (2000).

84. Jha, P. P. & Guyot-Sionnest, P. Trion Decay in Colloidal Quantum Dots. *ACS Nano* **3,** 1011–1015 (2009).

85. Greytak, A. B. *et al.* Alternating layer addition approach to CdSe/CdS core/shell quantum dots with near-unity quantum yield and high on-time fractions. *Chem. Sci.* **3,** 2028–2034 (2012).

86. McGuire, J. A. *et al.* Spectroscopic Signatures of Photocharging due to Hot-Carrier Transfer in Solutions of Semiconductor Nanocrystals under Low-Intensity Ultraviolet Excitation. *ACS Nano* **4,** 6087–6097 (2010).

87. Frantsuzov, P., Kuno, M., Jankó, B. & Marcus, R. A. Universal emission intermittency in quantum dots, nanorods and nanowires. *Nat. Phys.* **4,** 519–522 (2008).

88. Dworak, L. *et al.* Ultrafast Charge Separation at the CdSe/CdS Core/Shell Quantum Dot/Methylviologen Interface: Implications for Nanocrystal Solar Cells. *J. Phys. Chem. C* **115,** 3949–3955 (2011).

89. Rainò, G. *et al.* Probing the Wave Function Delocalization in CdSe/CdS Dot-in-Rod Nanocrystals by Time- and Temperature-Resolved Spectroscopy. *ACS Nano* **5,** 4031–4036 (2011).

90. Luo, J.-W., Franceschetti, A. & Zunger, A. Carrier Multiplication in Semiconductor Nanocrystals: Theoretical Screening of Candidate Materials Based on Band-Structure Effects. *Nano Lett.* **8,** 3174–3181 (2008).

91. Fernée, M. J., Littleton, B. N. & Rubinsztein-Dunlop, H. Detection of Bright Trion States Using the Fine Structure Emission of Single CdSe/ZnS Colloidal Quantum Dots. *ACS Nano* **3,** 3762–3768 (2009).

92. Califano, M., Franceschetti, A. & Zunger, A. Lifetime and polarization of the radiative decay of excitons, biexcitons, and trions in CdSe nanocrystal quantum dots. *Phys. Rev. B* **75,** 115401 (2007).

93. Brongersma, M. L. & Shalaev, V. M. The Case for Plasmonics. *Science* **328,** 440–441 (2010).

94. Eustis, S. & el-Sayed, M. A. Why gold nanoparticles are more precious than pretty gold: noble metal surface plasmon resonance and its enhancement of the radiative

and nonradiative properties of nanocrystals of different shapes. *Chem. Soc. Rev.* **35,** 209–217 (2006).

95. Cohen-Hoshen, E., Bryant, G. W., Pinkas, I., Sperling, J. & Bar-Joseph, I. Exciton–Plasmon Interactions in Quantum Dot–Gold Nanoparticle Structures. *Nano Lett.* **12,** 4260–4264 (2012).

96. Canneson, D. *et al.* Strong Purcell effect observed in single thick-shell CdSe/CdS nanocrystals coupled to localized surface plasmons. *Phys. Rev. B* **84,** 245423 (2011).

97. Jin, Y. & Gao, X. Plasmonic fluorescent quantum dots. **4,** (2009).

98. Ratchford, D., Shafiei, F., Kim, S., Gray, S. K. & Li, X. Manipulating Coupling between a Single Semiconductor Quantum Dot and Single Gold Nanoparticle. *Nano Lett.* **11,** 1049–1054 (2011).

99. Ito, Y., Matsuda, K. & Kanemitsu, Y. Mechanism of photoluminescence enhancement in single semiconductor nanocrystals on metal surfaces. *Phys. Rev. B* **75,** 033309 (2007).

100. Ma, X., Tan, H., Kipp, T. & Mews, A. Fluorescence Enhancement, Blinking Suppression, and Gray States of Individual Semiconductor Nanocrystals Close to Gold Nanoparticles. *Nano Lett.* **10,** 4166–4174 (2010).

101. Tan, R., Blom, D. A., Ma, S. & Greytak, A. B. Probing Surface Saturation Conditions in Alternating Layer Growth of CdSe/CdS Core/Shell Quantum Dots. *Chem. Mater.* **25,** 3724–3736 (2013).

102. Grabar, K. C., Freeman, R. G., Hommer, M. B. & Natan, M. J. Preparation and Characterization of Au Colloid Monolayers. *Anal. Chem.* **67,** 735–743 (1995).

103. Zimnitsky, D., Jiang, C., Xu, J., Lin, Z. & Tsukruk, V. V. Substrate- and time-dependent photoluminescence of quantum dots inside the ultrathin polymer LbL film. *Langmuir ACS J. Surf. Colloids* **23,** 4509–4515 (2007).

104. Yang, C.-M. *et al.* Enhanced photovoltaic response of organic solar cell by singlet-to-triplet exciton conversion. *Appl. Phys. Lett.* **90,** 133509 (2007).

105. Zhao, J., Wu, W., Sun, J. & Guo, S. Triplet photosensitizers: from molecular design to applications. *Chem. Soc. Rev.* **42,** 5323–5351 (2013).

106. Bachilo, S. M. & Weisman, R. B. Determination of Triplet Quantum Yields from Triplet−Triplet Annihilation Fluorescence. *J. Phys. Chem. A* **104,** 7711–7714 (2000).

107. Marin, D. M. *et al.* Efficient intersystem crossing using singly halogenated carbomethoxyphenyl porphyrins measured using delayed fluorescence, chemical

quenching, and singlet oxygen emission. *Phys Chem Chem Phys* **17,** 29090–29096 (2015).

108. *Topics in Fluorescence Spectroscopy*. **2,** (Kluwer Academic Publishers, 2002).

109. *Data Reduction and Error Analysis for the Physical Sciences*. (McGraw-Hill Education, 2002).

110. Straume, M. & Johnson, M. L. Monte Carlo method for determining complete confidence probability distributions of estimated model parameters. *Methods Enzymol.* **210,** 117–129 (1992).

111. Chowdhury, F. N., Kolber, Z. S. & Barkley, M. D. Monte Carlo convolution method for simulation and analysis of fluorescence decay data. *Rev. Sci. Instrum.* **62,** 47–52 (1991).

112. Quimby, R. S. in *Photonics and Lasers* 307–325 (John Wiley & Sons, Inc., 2006). at <http://onlinelibrary.wiley.com/doi/10.1002/0471791598.ch17/summary>

113. Leatherdale, C. A., Woo, W.-K., Mikulec, F. V. & Bawendi, M. G. On the Absorption Cross Section of CdSe Nanocrystal Quantum Dots. *J. Phys. Chem. B* **106,** 7619–7622 (2002).

114. Park, Y.-S. *et al.* Near-Unity Quantum Yields of Biexciton Emission from CdSe/CdS Nanocrystals Measured Using Single-Particle Spectroscopy. *Phys. Rev. Lett.* **106,** 187401 (2011).

115. Palik, E. D. *Handbook of Optical Constants of Solids*. (Academic Press, 1998).

116. Zhao, J., Chen, O., Strasfeld, D. B. & Bawendi, M. G. Biexciton Quantum Yield Heterogeneities in Single CdSe (CdS) Core (Shell) Nanocrystals and Its Correlation to Exciton Blinking. *Nano Lett.* **12,** 4477–4483 (2012).

APPENDIX A: ERROR ANALYSIS

A.1. Determining the uncertainties in fitting parameters.

In this thesis, we use non-linear least squares method for estimation of parameters by fitting the data with a multi-exponential model function. Most times, 5 or 6 exponentials are enough to fit the lifetime decays (2 parameters per exponential) but several times we might need 8-9 exponentials. This would mean determination of ~10-18 parameters by fitting the data. And, it should be noted that although we use complex non-linear functions to fit raw data but we don’t attach any physical significance to number of exponentials or complexity of function used. But we do use the fitting parameters and the high quality fits to calculate physically relevant quantities such as average lifetimes or test the validity of different mechanistic kinetic models. Therefore, it is of considerable importance to obtain realistic determination of statistical uncertainties for such physically relevant quantities. And, there are several approaches to estimate uncertainties or confidence intervals in fitting parameters;[108] however, each approach makes certain assumptions about the nature of underlying uncertainties.

Like most researchers in the field we use computer software to run our fitting procedures and we readily get standard uncertainties in each fitting parameter. Now, say, we need to calculate uncertainties in average lifetimes that depend on the combination of several fitting parameters. A simple and quick way would be just propagate uncertainties[109] using the following equation:

$$s_f = \sqrt{\sum_i \left(\frac{df}{da_i}\right)^2 s_{a_i}^2}$$

where s_f is the standard deviation of function, f, that we are interested in (could be average lifetime or any other function), s_{a_i} is the standard deviation in the i^{th} fit parameter, a_i. This approximation ignores correlations between parameters as well as second-and higher-order terms. Table A.1 shows the average lifetimes calculated using this approach for one of the datasets used in chapter 4, and we can note that standard uncertainties in average lifetimes are fairly small. However, the above procedure, although widely used, sometimes can significantly underestimate errors and is statistically relevant for linear fit functions with no correlations in independent data points, and assumes that uncertainties are normally distributed, which might not be true. Further, in our case, apart from using a highly non-linear fitting function, it is a difficult task to identify parameter spaces that minimize correlation.[110]

Table A.2: Estimating uncertainties in average lifetimes.

Average lifetimes, $\langle\tau\rangle$, at different excitation powers	Uncertainties (2 × the standard deviation) by propagating uncertainties	Uncertainties (2 × the standard deviation) using Monte Carlo simulations
$\langle n\rangle = 0.015$	0.45 ns	0.67 ns
$\langle n\rangle = 0.15$	0.66 ns	0.93 ns
$\langle n\rangle = 1.5$	0.26 ns	0.36 ns
$\langle n\rangle = 15$	0.83 ns	1.01 ns

In this study, therefore we have used a Monte Carlo[108] method to evaluate uncertainties in parameters. This method has the advantage that we can compute the complete probability distribution for parameters without making any assumption on the shape of that probability distribution. The only requirement is prior knowledge of distribution of uncertainties in each data point which is in our case is well known (poissonian distribution). The method basically involves fitting the decay as usual, with as many exponentials as are necessary to satisfy our chi-squared and Durbin-Watson requirements. This yields a fit function, $I(t)$. Then, using a Monte Carlo algorithm developed by Chowdhury, et al[111] together with $I(t)$ and the recorded instrument response, we generate simulated decays with the same total number of counts as the original data. This simulated decay is then modeled with another multi-exponential function, $I'(t)$, (using the $I(t)$ function as a starting guess for the parameters) and the average emission times are calculated from this function. This procedure is then repeated several hundred times to obtain a distribution of average lifetimes with associated standard deviations. We have found that uncertainties in average lifetimes calculated using Monte Carlo method often are slightly bigger than that calculated by propagating the standard uncertainties (see Table A.1).

A.2. Statistics for the kinetic scheme

I have included standard deviations for parameters used in all the kinetic schemes shown in this work; however, I have not shown any statistic such as reduced chi-square (χ^2) denoting the significance (or goodness of fit) of a particular kinetic scheme because we couldn’t calculate such a measure very reliably in our present analysis. We didn’t fit the kinetic scheme to raw data but to fits of raw data therefore, we did not have a distribution of experimental uncertainties associated with each data point, and couldn’t predict what is the probability of obtaining say a given reduced chi square just because of random errors. Therefore, we rely on global analysis of multiple datasets with a single physical model with as few parameters as possible, and adding complexity only when we can visually see any improvement in fits. For example, in chapter 3 we fit 11 different datasets containing 132 parameters with a single kinetic scheme having 12 variable parameters, thus using just ~1 parameter per dataset..

A.3. Rate constants for kinetic schemes used in chapter 3

Scheme Parameters	**Thick shell QDs**	**Thin shell QDs**
Energy (bright exciton, X_B), eV	2	2
Energy (Ground, G), eV	0	0
Energy (Trap 1, $T1$), eV	1.879 ± 0.001	1.932 ± 0.019
Energy Dist. (Trap 1), eV	0.0237 ± 0.0028	0.0572± 0.016
Dist. skewness(Trap 1)	0.001871 ± 9.18E-09	0.00131 ± 1.31
No. of Trap Sites (Trap 1)	0.1859 ± 0.1786	1.358 ± 2.23
Energy (Initial X), eV	3.01	3.01
Energy ($dark\ exciton, X_D$), eV	1.998	1.998
$k_R(X_B \rightarrow G)$, 1/sec	$10^{7.9 \pm 0.059}$	$10^{8.14 \pm 0.26}$
$k(X_B \rightarrow X_D)$, 1/sec	$10^{12.4}$	10^{12}
$k(T1 \rightarrow G)$, 1/sec	$10^{4.61 \pm 0.5}$	$10^{4.88 \pm 0.6}$
$k(X \rightarrow X_D)$, 1/sec	10^{12}	10^{12}
Lambda (Trap 1), eV	0.01653 ± 0.005	0.03934 ± 2.41E-02
coupling constant (Trap 1), 1/sec	0.000196 ± 9.15E-05	1.16E-05 ± 1.04E-05
Energy (Trap 2, $T2$),eV	N.A	2.007 ± 0.2
$k(T2 \rightarrow G)$, 1/sec	N.A	7.69 ± 1.4

lambda (Trap 2), eV	N.A	0.4004 ± 1.8
coupling constant (Trap 2), 1/sec	N.A	0.000336 ± 0.006

It is to be noted that some parameters shown above have no associated uncertainty because they were held constant during the fitting process. Further, all the emission comes from the bright exciton state. An emission band of 30 nm was used to mimic the emission broadening in ensemble samples.

APPENDIX B: EXCITATION PROPERTIES AND MULTIPULSE FIT PARAMETERS

B.1. Calculation of laser spot size and excitation volume

The focused spot diameter (ϕ) and depth of focus (DOF) for a Gaussian laser beam is given by[112]:

$$\phi = \frac{4}{\pi} \times wavelength \times \frac{(lens\ focal\ length)}{beam\ diameter} \times M^2$$

$$DOF = \frac{8}{\pi} \times wavelength \times \left(\frac{lens\ focal\ length}{beam\ diameter}\right)^2 \times M^2$$

where the wavelength of laser beam is 410nm, the beam diameter is 0.3 cm, the lens used has a focal length of 5 cm, and M^2 is the beam quality factor. Here, DOF is defined as the distance at which excitation beam is $\sqrt{2}$ times larger than it is at the focal spot.

For a theoretical Gaussian beam, $M^2 = 1$ however in our case the input beam is non-spherical hence $M^2 = 3$ which gives,

$$\Rightarrow \phi = 2.61 \times 10^{-3}\ \text{cm}$$

$$\Rightarrow DOF = 86.91 \times 10^{-3}\ \text{cm}$$

And, therefore the spot size then is $5.4 \times 10^{-6}\ \text{cm}^2$ at 410 nm. Further the excitation volume can be calculated as:

$$excitaion\ vol = spot\ size \times DOF$$

$$excitaion\ vol = 0.469 \times 10^{-6}\ \text{cm}^3$$

B.2. Calculation of photo-absorption events per illuminated QD per laser pulse, λ

The absorption cross-section (σ) for CdSe-CdS core-shell QDs is determined by the following formula developed by Leatherdale et. al[113]:

$$\sigma(\omega) = \frac{\omega}{n_{med}\, c}\ |f(\omega)|^2\ 2n_1k_1\frac{4}{3}\ \pi R^3 = \varsigma_\omega\ R^3$$

$$f(\omega) = \frac{3\ n_{med}^2}{n_1^2 + 2n_{med}^2}$$

where n_1, k_1 is the real and imaginary part of the bulk absorption coefficient, $f(\omega)$ is the correction factor that accounts for local field effects, R is the radius of the QD and n_{med} is the refractive index of the medium. For core-shell QDs, we calculate the absorption cross-section by averaging it over the entire QD volume[114]:

$$\sigma(\omega) = \varsigma_\omega^{core}\ R^3 + \varsigma_\omega^{shell}\ [(R+H)^3 -\ R^3] = \zeta_\omega^{shell}(R+H)^3 + (\zeta_\omega^{core} - \zeta_\omega^{shell})R^3$$

where R is the core radius and H is the shell thickness. At 410 nm excitation, using n, k values obtained from Palik et. al[115], the optical constants for CdSe and CdS in hexane (n_{med} = 1.375) are,

$\zeta_{410nm}^{core} = 4.16 \times 10^{-16} cm^2/nm^3$ and $\zeta_{410nm}^{shell} = 3.04 \times 10^{-16} cm^2/nm^3$

Therefore, for our QDs with R=2 nm and H=4.1 nm,

⇨ absorption cross-section at 410 nm, $\sigma = 6.98 \times 10^{-14} cm^2$

Further, we can calculate the average number of photons absorbed per QD per laser pulse by the following equation[116]:

$$\lambda = \frac{\sigma \times \text{power}}{\text{photon energy} \times \text{spot size} \times \text{laser repetition rate}}$$

In our experiment, the laser repetition rate used is 100 KHz, the photon energy is 4.84×10^{-19} J and spot size is $5.4 \times 10^{-6}\,\text{cm}^2$ at 410 nm, and the three different laser powers used are: low power (LP) at 7.46 nW, medium power (MP) at 560 nW and high power (HP) at 5.6 µW.

Therefore, at different excitation energies, the average number of photons absorbed per pulse are, $\lambda = 0.002$ (low power, LP), 0.15 (medium power, MP) and 1.5 (high power, HP).

B.3. Predicting QD excitation statistics

We determined expressions for the following probabilities for photoexcitation of QDs after *N* laser pulses, assuming that the absorption cross section for the 1st, 2nd, 3rd, etc, photoexcitations are identical.

1. Probability, $P_N^{(0)}$, that a QD never undergoes photoexcitation.
2. Probability, $P_N^{(1)}$, that a QD is photoexcited one or more times, but never more than once per pulse.
3. Probability, $P_N^{(2)}$, that a QD is photoexcited two or more times, and more than once per pulse on at least one occasion.

Assuming Poisson statistics, the probability that a QD does not absorb a photon in *N* laser pulses, when there are, on average, λ photoexcitations per QD per pulse, is:

$$P_N^{(0)} = (p_0)^N = e^{-N\lambda}$$

Probability that a QD is photoexcited one or more times in *N* pulses, but never more than once per pulse is:

$$P_N^{(1)} = p_{1N}^{(1)} + p_{2N}^{(1)} + \cdots + p_{NN}^{(1)}$$

Where, $p_{xN}^{(1)}$, is the probability that a QD is excited *x* times in *N* pulses, but never more than once per pulse.

$$p_{xN}^{(1)} = \binom{N}{x}(p_1)^x(p_0)^{N-x} = \binom{N}{x}\left(\lambda e^{-\lambda}\right)^x\left(e^{-\lambda}\right)^{N-x} = \binom{N}{x}\lambda^x e^{-N}$$

Therefore,

$$P_N^{(1)} = e^{-N\lambda}\sum_{i=1}^{N}\binom{N}{i}\lambda^i = e^{-N\lambda}\sum_{i=0}^{N}\binom{N}{i}\lambda^i - P_N^{(0)} = [(1+\lambda)^N - 1]e^{-N\lambda}$$

The probability that a QD is photoexcited two or more times, and more than once per pulse on at least one occasion is given by:

$$\begin{aligned} P_N^{(2)} &= p_{1N}^{(2)}\left(P_{N-1}^{(0)} + P_{N-1}^{(1)}\right) + p_{2N}^{(2)}\left(P_{N-2}^{(0)} + P_{N-2}^{(1)}\right) + \cdots + p_{NN}^{(2)} \\ &= \sum_{i=1}^{N} p_{in}^{(2)}(1+\lambda)^{N-i}e^{-(N-i)\lambda} \\ &= \sum_{i=1}^{N}\binom{N}{i}\left(\frac{\lambda^2 e^{-\lambda}}{2}\right)^i(1+\lambda)^{N-i}e^{-(N-i)\lambda} \end{aligned}$$

$$= (1+\lambda)^N e^{-N\lambda} \sum_{i=0}^{N} \left(\frac{\lambda^2}{2(1+\lambda)}\right)^i \binom{N}{i} - \left(P_N^{(0)} + P_N^{(1)}\right)$$

Therefore,

$$P_N^{(2)} = \left[\left(1+\lambda+\frac{1}{2}\lambda^2\right)^N - (1+\lambda)^N\right] e^{-N\lambda}$$

B.4. Fit parameters

Table 3: Fit function parameters for $\boldsymbol{I_1^{(1)}(t)}$ and $\boldsymbol{I_1^{(2)}(t)}$

		Low power		**Medium power**		**High power**	
	i	α_i	$1/k_i$ (ns)	α_i	$1/k_i$ (ns)	α_i	$1/k_i$ (ns)
$I_1^{(1)}(t)$	1	1.00	0.22	1.00	0.95	1.00	0.75
	2	2.46	3.39	1.21	7.36	0.822	7.70
	3	3.21	10.84	1.99	24.69	0.832	24.26
	4	6.85	27.12	0.919	48.14	0.440	52.00
	5	2.55	54.84	0.120	80.80	0.0124	233.06
	6	0.0644	254.78	0.0132	333.98	0.00151	1227.39
	7	0.00620	1592.96	0.00193	1446.68		

	i	α_i	$1/k_i$ (ns)	α_i	$1/k_i$ (ns)	α_i	$1/k_i$ (ns)
$I_2^{(2)}(t)$	1	-	-	1.00	7.90	1.00	0.91
	2	-	-	-	-	0.979	7.02

N	$\chi_N^{(1)}$	$\chi_N^{(2)}$	$\chi_N^{(1)}$	$\chi_N^{(2)}$	$\chi_N^{(1)}$	$\chi_N^{(2)}$
1	0.0006	0	0.0014	0	0.0038	0
5	0.0132	0	0.0213	0.0298	0.0285	0.0371
9	0.0134	0	0.0214	0.0343	0.0270	0.0445
13	0.0147	0	0.0222	0.0458	0.0289	0.0571
17	0.0144	0	0.0226	0.0501	0.0311	0.0720
21	0.0142	0	0.0224	0.0540	0.0305	0.0743
25	0.0136	0	0.0221	0.0562	0.0316	0.0853

APPENDIX C: MULTI-PULSE DATASET FOR USC QDs

Multi-pulse dataset collected at short (500 ns) and long (5 us) time windows for core-shell CdSe/CdS acquired from University of South Carolina. The QDs were washed and dispersed in a degassed solvent and excited at 3.02 eV with medium excitation power ($\lambda = 0.2$)

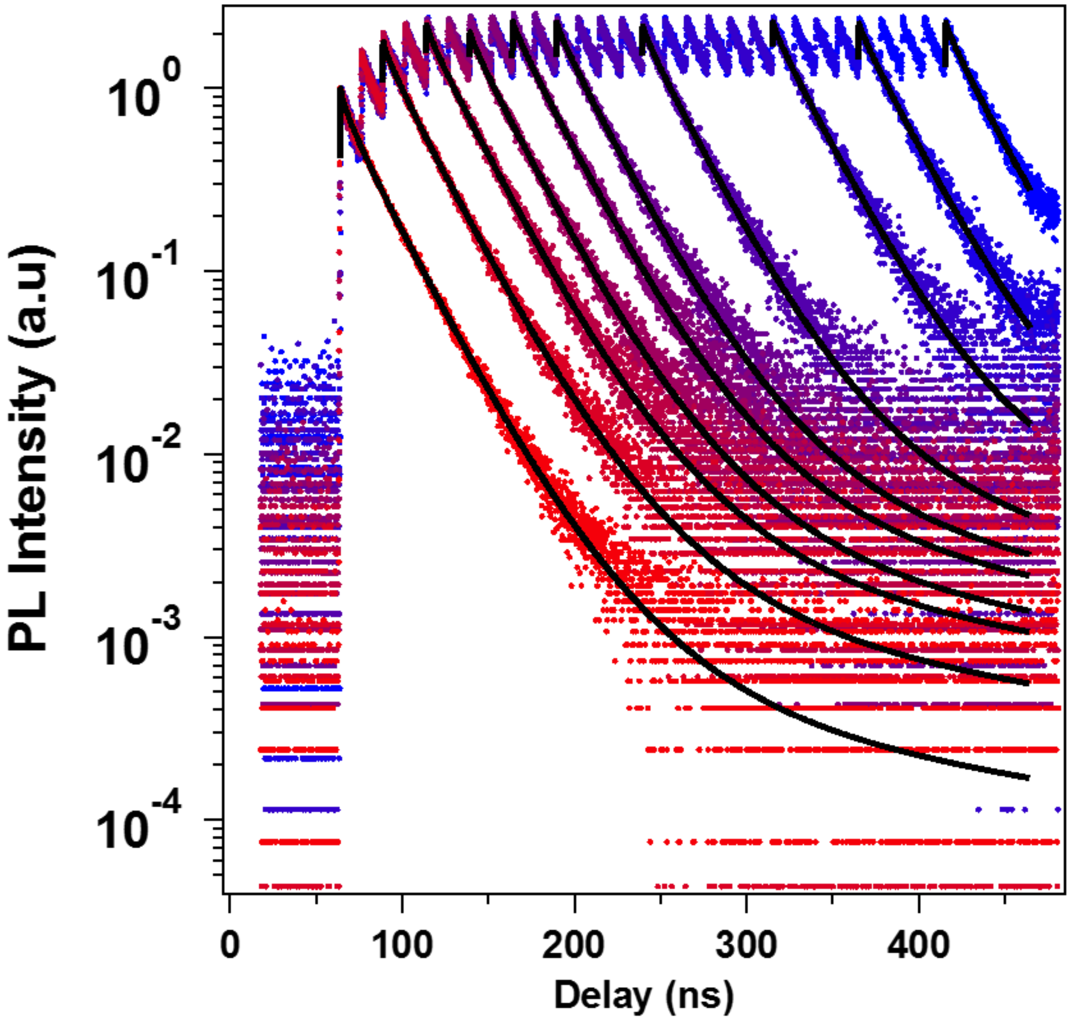

Figure C.1: Composite plots of multi-pulse time-resolved fluorescence data recorded for 10 different pulse sequences, containing 1, 3 5, 7, 9, 11, 15, 21, 25 and 29 pulses, over 500 ns.

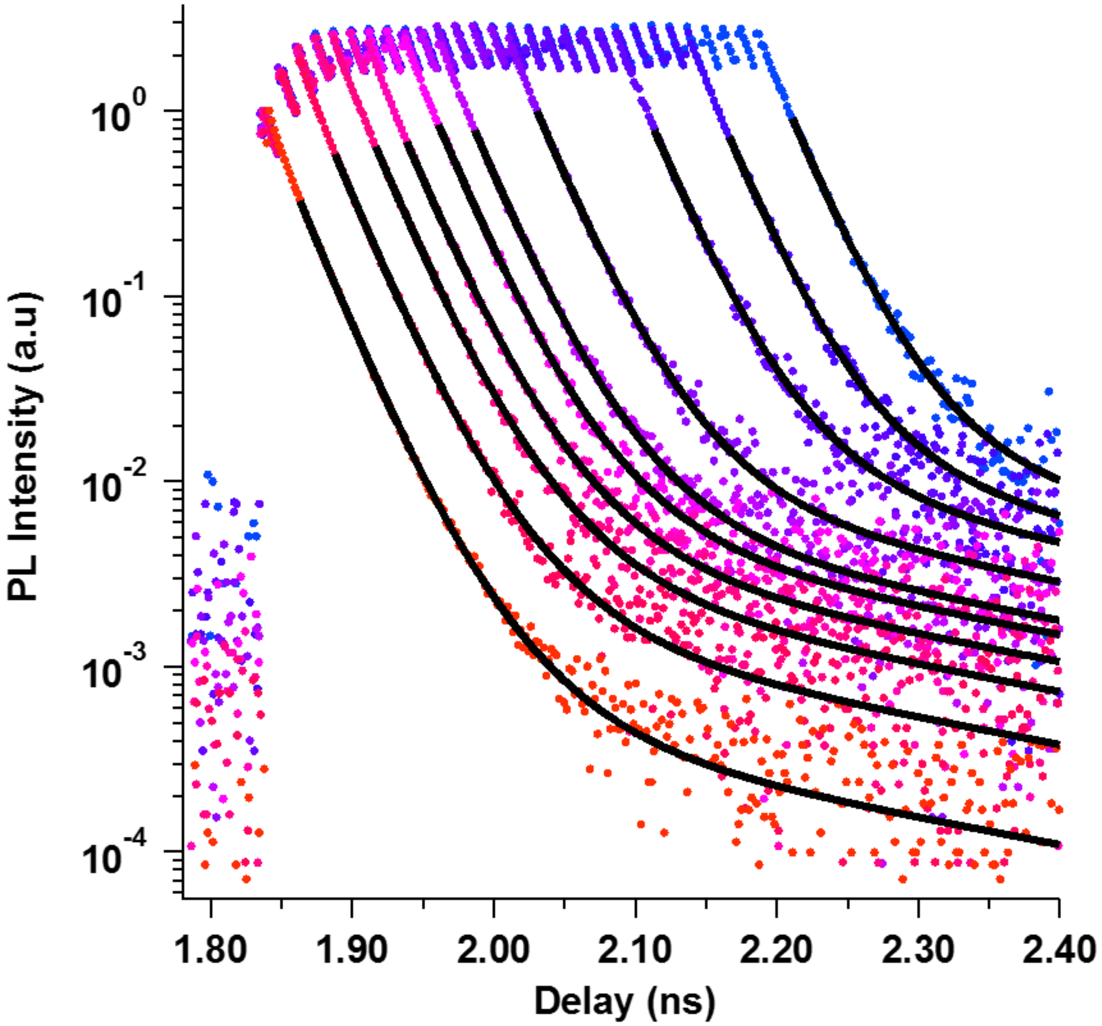

Figure C.2: Composite plots of multi-pulse time-resolved fluorescence data recorded for 10 different pulse sequences, containing 1, 3 5, 7, 9, 11, 15, 21, 25 and 29 pulses, over 5 μs.

APPENDIX D: AFM IMAGES

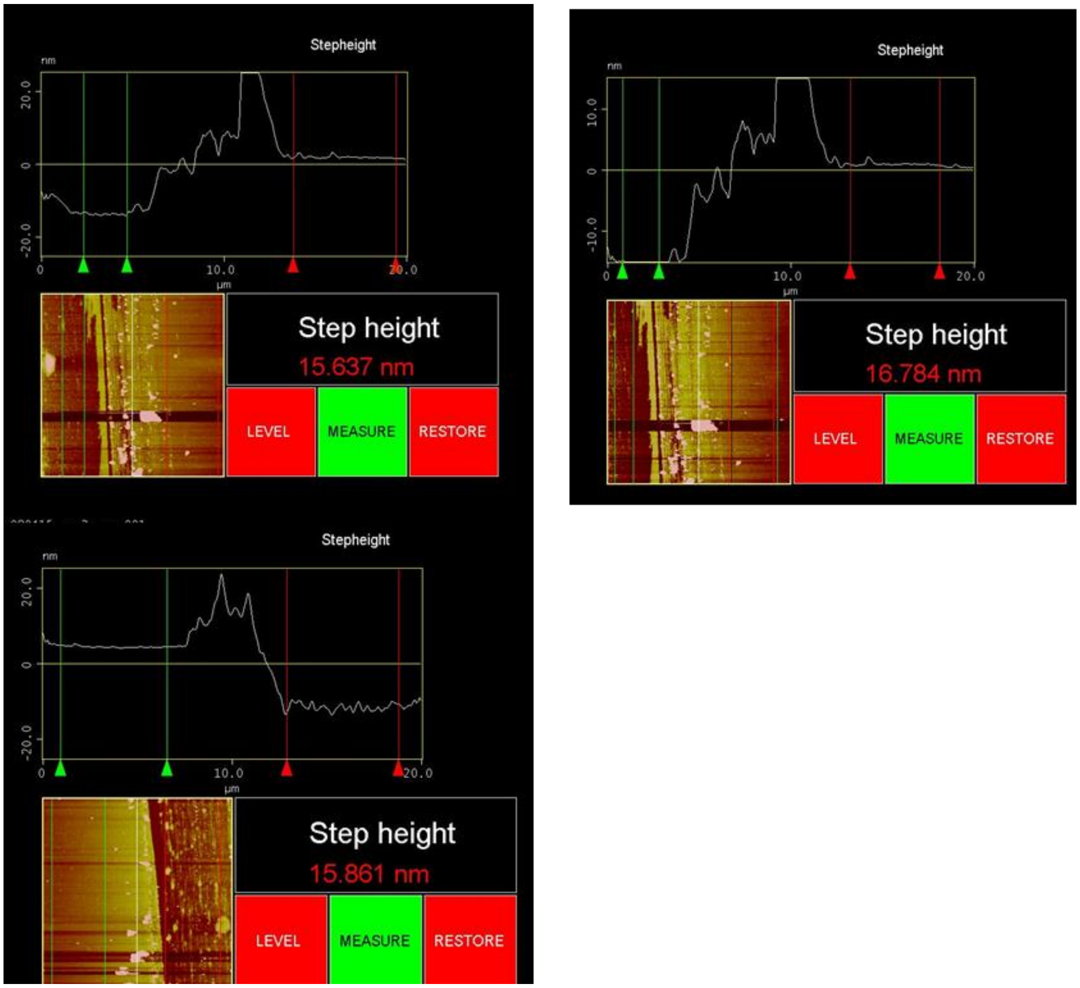

Figure D.1: Atomic force microscopy images of CdSe/CdS thin films (three different samples) spun cast on clean glass slides.

The AFM images were taken using Digital Instruments Veeco Metrology Group Dimension 3100 Atomic Force Microscope at a scan rate of 0.8 Hz with 256 samples/line.